

---


Electronic Theses and Dissertations, 2004-2019

---

2007

## High-speed Modelocked Semiconductor Lasers And Applications In Coherent Photonic Systems

Wangkuen Lee  
*University of Central Florida*

 Part of the [Electromagnetics and Photonics Commons](#), and the [Optics Commons](#)  
Find similar works at: <https://stars.library.ucf.edu/etd>  
University of Central Florida Libraries <http://library.ucf.edu>

This Doctoral Dissertation (Open Access) is brought to you for free and open access by STARS. It has been accepted for inclusion in Electronic Theses and Dissertations, 2004-2019 by an authorized administrator of STARS. For more information, please contact [STARS@ucf.edu](mailto:STARS@ucf.edu).

---

### STARS Citation

Lee, Wangkuen, "High-speed Modelocked Semiconductor Lasers And Applications In Coherent Photonic Systems" (2007). *Electronic Theses and Dissertations, 2004-2019*. 3238.  
<https://stars.library.ucf.edu/etd/3238>

HIGH-SPEED MODELOCKED SEMICONDUCTOR LASERS  
AND APPLICATIONS IN COHERENT PHOTONIC SYSTEMS

by

WANGKUEN LEE

B.S. in Physics, Pusan National University, Republic of Korea, 1997

M.S. in Physics, Pusan National University, Republic of Korea, 1999

M.S. in Optics, University of Central Florida, Orlando, Florida, 2002

A dissertation submitted in partial fulfillment of the requirements  
for the degree of Doctor of Philosophy  
in the College of Optics and Photonics: CREOL & FPCE  
at the University of Central Florida  
Orlando, Florida

Summer Term  
2007

Major Professor: Peter J. Delfyett, Jr.

© 2007 Wangkuen Lee

## ABSTRACT

1.55- $\mu\text{m}$  high-speed modelocked semiconductor lasers are theoretically and experimentally studied for various coherent photonic system applications. The modelocked semiconductor lasers (MSLs) are designed with high-speed ( $>5$  GHz) external cavity configurations utilizing monolithic two-section curved semiconductor optical amplifiers. By exploiting the saturable absorber section of the monolithic device, passive or hybrid modelocking techniques are used to generate short optical pulses with broadband optical frequency combs. Laser frequency stability is improved by applying the Pound-Drever-Hall (PDH) frequency stabilization technique to the MSLs. The improved laser performance after the frequency stabilization (a frequency drifting of less than 350 MHz), is extensively studied with respect to the laser linewidth ( $\sim 3$  MHz), the relative intensity noise (RIN) ( $< -150$  dB/Hz), as well as the modal RIN ( $\sim 3$  dB reduction). MSL to MSL, and tunable laser to MSL synchronization is demonstrated by using a dual-mode injection technique and a modulation sideband injection technique, respectively. Dynamic locking behavior and locking bandwidth are experimentally and theoretically studied. Stable laser synchronization between two MSLs is demonstrated with an injection seed power on the order of a few microwatt. Several coherent heterodyne detections based on the synchronized MSL systems are demonstrated for applications in microwave photonic links and ultra-dense wavelength division multiplexing (UD-WDM) system. In addition, efficient coherent homodyne balanced receivers based on synchronized MSLs are developed and demonstrated for a spectrally phase-encoded optical CDMA (SPE-OCDMA) system.

## ACKNOWLEDGMENTS

I have enjoyed my life in College of Optics and Photonics / Center for Research and Education in Optics and Lasers (CREOL) learning optics and lasers everyday. I am always so proud to be a member of CREOL and especially, Ultrafast Photonics group. All of my passions and efforts towards modelocked lasers and ultrafast photonics were grown to make the modest success during my Ph D study, thanks to the endless support and encouragement from my adviser, Peter J. Delfyett, Jr.

I am thankful to the past and present Ultrafast Photonics group members, Dr. Hossein Izadpanah, Dr. Sangyoun Gee, Dr. Luis Archundia-Berra, Dr. Tolga Yilmaz, Dr. Bojan Resan, Dr. Michael Mielke, Dr. Myoung-Taek Choi, Dr. Kyungbum Kim, Shinwook Lee, Franklyn Quinlan, Sarper Ozharar, Ji-Myoung Kim, Leonard Kisimbi, Scott Rozzo, Dimitrios Mandridis, Ibrahim Ozdur, Mohammad Umar Piracha, Charles Williams, Samantha Wallace, Iffat Nayyar, Sharad Bhooplapur, and Abhijeet Ardey for their help and assistances. Also I would like to thank Dr. Hwan Kim and Dr. Inwoong Kim for many useful discussions.

I am sincerely grateful to committee members, Professor Guifang Li, Professor Patrick LiKamWa, and Professor Donald Malocha for their interest and suggestions for this dissertation.

I would like to give biggest thanks to my wife, Junghee and my wonderful daughters, Esther and Janice. I dedicate this dissertation to my father in heaven.

# TABLE OF CONTENTS

CHAPTER 1: INTRODUCTION .....	1
1.1 Introduction.....	1
1.2 Motivation and Dissertation Statement.....	2
1.3 Overviews .....	3
CHAPTER 2: HIGH-SPEED MODELOCKED SEMICONDUCTOR LASERS .....	5
2.1 Introduction.....	5
2.1 External Cavity Modelocked Semiconductor Lasers.....	6
2.1.1 General Features of the High-Speed MSLs .....	6
2.1.2 Theory of High-Speed MSLs.....	11
2.1.3 Numerical Modeling and Simulation of High-Speed MSLs.....	15
2.2 Laser Frequency Stabilization .....	20
2.2.1 The Pound-Drever-Hall (PDH) Technique .....	20
2.2.2 Frequency Stabilized MSLs .....	24
2.3 Linewidth .....	27
2.3.1 Linewidth of MSLs .....	27
2.3.2 Linewidth Measurement by Delayed Self-Heterodyne Technique.....	27
2.4 Relative Intensity Noise (RIN) .....	33
2.4.1 Introduction of Relative Intensity Noise (RIN) .....	33
2.4.2 Measurement and Calibration of RIN .....	34
2.4.3 RIN Measurement of MSLs .....	35
2.4.4 General RIN Characteristics of a Frequency Stabilized Grating-Coupled MSL .....	37
2.4.5 Modal RIN Reduction of a Frequency Stabilized Grating-Coupled MSL.....	39
2.4.6 Comparison of RIN of a Mirror Coupled and a Grating Coupled MSLs .....	43
CHAPTER 3: SYNCHRONIZED MSL SYSTEMS .....	45
3.1 Introduction.....	45
3.1.1 Theory of Injection Locking .....	45
3.1.2 Locking Range .....	49
3.2 Experimental Demonstration of Injection Locking Techniques.....	53
3.2.1 Modulation Sideband Injection Locking of a MSL with a Tunable CW Laser.....	53
3.2.2 Dual-Mode Injection Locking of Two Independent MSLs .....	55
CHAPTER 4: APPLICATIONS WITH SYNCHRONIZED MSLS.....	59
4.1 Coherent Analog Photonic Links.....	59
4.1.1 Heterodyne Detection .....	59
4.1.2 Broadband Coherent Probe System .....	64
4.2 Coherent Ultra-Dense WDM System .....	70
4.2.1 Single Channel Modulation (CW Injection Locking).....	71
4.2.2 Multi-Channel Modulation (Pulsed Injection Locking).....	74
4.2.3 Comparison of BER.....	77

4.3 Secure Coherent Communications.....	79
4.3.1 Spectrally Phase-Encoded Optical CDMA (SPE-OCDMA) .....	79
4.3.2 Coherent Pulse Detection and Multi-Channel Coherent Detection .....	81
4.3.3 High-Speed MSM Balanced Receiver .....	93
CHAPTER 5: CONCLUSION .....	97
5.1 Summary .....	97
5.2 Future Studies .....	99
APPENDIX A: HIGH-SPEED MODELOCKED SEMICONDUCTOR LASER SIMULATION CODE IN MATLAB.....	101
APPENDIX B: LASER FREQUENCY STABILIZATION BY POLARIZATION SPECTROSCOPY .....	106
APPENDIX C: LONG-WAVELENGTH TWO-SECTION MONOLITHIC MSL FABRICATION.....	110
C.1 Laser Diode Fabrication Steps .....	111
C.2 Device Characteristics.....	112
C.3 Improved Design.....	118
C.4 Metallic Pad Design for the High-speed MSL.....	119
APPENDIX D: SEMICONDUCTOR OPTICAL AMPLIFIER DEVICE CHARACTERISTICS AND MISCELLANEOUS SYSTEM ELEMENTS .....	121
D.1 Two-Section SOA Characteristics .....	122
D.2 Covega SOA Characteristics.....	125
D.3 Essex Hyperfine WDM.....	126
D.4 Grating Filter.....	128
D.5 Fiber Coupling System .....	129
LIST OF REFERENCES .....	130

## LIST OF FIGURES

Figure 1: Schematic of the external cavity high-speed MSL cavity configurations. (a) a grating-coupled MSL (b) a mirror-coupled MSL. L: lens; G: grating; M: mirror; S: optical sampler.....	7
Figure 2: Pictures of the external cavity high-speed MSL cavity configurations. (a) the grating-coupled MSL system (b) the mirror-coupled MSL system (c) the grating-coupled MSL cavity configuration (d) the mirror-coupled MSL cavity configuration.....	8
Figure 3: Optical spectra of the 6.33 GHz external cavity MSLs (a) grating-coupled MSL (hybridly modelocked) (b) mirror-coupled MSL(passively modelocked).....	9
Figure 4: RF spectra of the 6.33 GHz external cavity MSLs (a) grating-coupled MSL (hybridly modelocked) (b) mirror-coupled MSL (passively modelocked) .....	10
Figure 5: Intensity autocorrelation of the 6.33 GHz external cavity MSLs (a) grating-coupled MSL (hybridly modelocked) (b) mirror-coupled MSL(passively modelocked) .....	11
Figure 6: Schematic diagram of equivalent systems and numerical simulation modeling of the external cavity MSL systems (SCPM: self-colliding pulse modelocking, CPM: colliding pulse modelocking).....	15
Figure 7: Input noise spectrum and spectral band-pass filter (solid curve) (a) Linear scale (b) Log scale.....	17
Figure 8: Output laser spectra (a) time evolution of the laser spectrum (3D mesh plot) (b) time evolution of the laser spectrum (contour plot) (c) output laser spectrum after 50 times iteration (Linear scale)(d) output laser spectrum after 50 times iteration (Log scale).....	18
Figure 9: Output optical pulses (a) time evolution of optical pulses (3D contour plot) (b) pulse trains (c) optical pulse output (d) temporal phase of the optical pulse .....	19
Figure 10: Schematic of the Pound-Drever-Hall laser frequency stabilization Setup. (a) schematic (b) picture of real system, O: optical amplifier; PC: polarization controller; HW: half-wave plate; PBS: polarizing beam splitter; QW: quarter-wave plate; PD: photodetector; E: electrical amplifier; BPF: band-pass filter; LPF: low-pass filter. ....	21
Figure 11: Plot of the magnitude and phase of the reflection coefficient of the reference etalon (a) magnitude (b) phase.....	22
Figure 12: The PDH error signal (a) theoretically calculated (b) experimentally measured (modulation frequency: 640MHz) .....	23



Figure 13: Transmission measurement of the laser output with respect to the reference etalon before and after the PDH frequency stabilization.....	25
Figure 14: Comparison of optical spectra before and after the PDH laser frequency stabilization (a) before stabilization (b) after stabilization.....	26
Figure 15: Optical comb frequency drift measurement with the heterodyne mixing technique (a) before PDH frequency stabilization (b) after stabilization .....	26
Figure 16: Experimental setup of the delayed self-heterodyne linewidth measurement .....	28
Figure 17: Single axial mode filtering for the linewidth measurement (a) setup for the single axial mode filtering (b) optical spectrum of the filtered single axial mode from the frequency stabilized 6.33 GHz grating-coupled MSL. ....	29
Figure 18: Heterodyning process in the delayed self-heterodyne technique. ....	31
Figure 19: The linewidth measurement using delayed self-heterodyne technique (a) Linewidth measurement of a commercial DFB laser (b) Linewidth measurement of the frequency stabilized MSL .....	32
Figure 20: Schematic diagram of RIN measurement setup and calibration. ....	35
Figure 21: Schematic diagram of the general RIN and modal RIN measurement .....	36
Figure 22: General RIN measurement: (a) RIN of the entire axial mode set of the MSL (b) corresponding optical spectra of the MSL .....	38
Figure 23: Modal RIN measurement (a) RIN measurements of a filtered single axial mode of the MSL with and without PDH frequency stabilization (b) theoretically calculated modal RIN (N=30).....	41
Figure 24: The RIN measurements of the mirror-coupled MSL systems.....	44
Figure 25: Injection locking range depending on $\alpha$ .....	52
Figure 26: Schematic of experimental setup for the modulation sideband injection locking of a MSL with a tunable CW laser.....	53
Figure 27: RF spectrum of the 6.33 GHz passively modelocked semiconductor laser LO (a) before injection locking and (b) after injection locking.....	54
Figure 28: Conceptual diagram of the dual-mode injection locking of MSLs .....	55
Figure 29: Experimentally measured optical spectra of the dual-mode injection seed from a master MSL (a) as well as an injection locked slave MSL(b). ....	56

Figure 30: Dynamic locking and pulling behavior of the injection seeded SL carrier. (a) dynamic evolution of the injection seeded SL carrier of injection locking (b) dynamic evolution of the cavity frequency detuned SL carrier of frequency pulling. ....	57
Figure 31: Schematic of the experimental setup for optical heterodyne detection based on modulation sideband injection locking. PML LD – passively modelocked laser diode; HF-WDM– hyperfine WDM filter; MZ – Mach-Zehnder intensity modulator; PD – photodiode; RFSA – radio frequency spectrum analyzer; OSA – optical spectrum analyzer; others defined in text. $f_1 = 500$ MHz; $f_2 = 700$ MHz .....	60
Figure 32: Modulated optical two-tone analog signals ( $f_1 = 500$ MHz; $f_2 = 700$ MHz) (a) at optimum RF input power (b) at high RF input power (c) IMD measurement of the analog two-tone signals. ....	61
Figure 33: A filtered single axial mode of the 6.33 GHz passively modelocked semiconductor laser LO (a) and the optical spectrum of the analog signals ( $f_1 = 500$ MHz, $f_2 = 700$ MHz) heterodyned with the selected single axial mode of the LO (b). ....	62
Figure 34: Heterodyne beat signal (a) before injection locking, (b) after injection locking (I: IF 12.66 GHz tone, II: 13.16 GHz tone [ IF+500 MHz ], III: 13.36 GHz tone [ IF+700 MHz ] ), (c) the microwave bandpass filtered 13.16 GHz tone at the resolution bandwidth of 30 kHz, and (d) a higher resolution scan of the 13.16 GHz tone (RBW = 1kHz). ....	63
Figure 35: The experimental setup for the dual-mode injection locking of independent MSLs and heterodyne detection of a two-tone analog signal; GF: grating filter(See Appendix D); GB: optical gain block; PC: polarization controller; HF-WDM: hyperfine WDM filter; MZ: Mach-Zehnder intensity modulator; PD: photodiode; BPF: electrical bandpass filter; ESA – electrical spectrum analyzer; OSA – optical spectrum analyzer; others defined in text. ....	65
Figure 36: Two-tone analog signal. (a) sinusoidally modulated optical analog signals at 500 MHz and 700 MHz. (b) spurious free dynamic range (SFDR) measurement of the two-tone analog signal. ....	66
Figure 37: Optical heterodyning (a) optical spectrum of the data channel from the ML (b) optical spectrum of the selected probe channel from the injection locked SL. (c) optical heterodyning of the data channel and the LO probe channel. ....	67
Figure 38: Experimental results of the coherent heterodyne detection of the two-tone analog signal. (d) heterodyne beat signal around the IF of 12.66 GHz before injection locking (e) heterodyne beat signal around the IF of 12.66 GHz after injection locking (f) the filtered heterodyne beat signal at 13.160 GHz (IF carrier 12.66 GHz +500 MHz) under a strongly injection locked state. ....	68

Figure 39: Schematic of coherent heterodyne digital data detection based on dual-mode hybrid injection locking. (a) single channel data modulation (injection locking without data). (b) multi-channel data modulation (injection locking with data).....	70
Figure 40: Schematic of the experimental setup for coherent heterodyne digital data detection in the case of single channel data modulation.....	71
Figure 41: Clock Recovery. (a) Pulse train of the 6.33GHz hybridly modelocked master laser (Pulse Width: 17 ps, RMS Jitter: 600-900 fs )(b) Recovered pulse train from the dual-mode hybrid injection locked passively modelocked slave laser (Pulse Width: 16.2 ps, RMS Jitter: 1.2-2.1 ps).....	72
Figure 42: Coherent Heterodyne Digital Data Detection. (a) Eye diagram of the heterodyne detection of 500Mb/s PRBS data signals before injection locking (b) under injection locked state. (c) Bit error rate (calculated from measured SNR): square symbol (back to back direct detection of the PRBS data channel), triangle symbol (heterodyne detection of PRBS data under injection locked state).....	73
Figure 43: Schematic of the experimental setup for coherent heterodyne digital data detection in the case of multi-channel data modulation .....	75
Figure 44: Data Clock Recovery. (a) Pulse train of the 6.33GHz hybridly modelocked master laser (Pulse Width: 17 ps, RMS Jitter: 700-900 fs) (b) Recovered pulse train from the dual-mode hybrid injection locked passively modelocked slave laser (Pulse Width: 16.1 ps, RMS Jitter: 3.0-4.0 ps). .....	75
Figure 45: Coherent Heterodyne Digital Data Detection. (a) Eye diagram of the heterodyne detection of 316.5 Mb/s PRBS data signals before injection locking (b) under injection locked state.....	76
Figure 46: Comparison of BER: (a) open circle symbol (back to back direct detection of entire data channels), closed circle (heterodyne detection of a single data channel under injection locked state). Triangle (single channel modulation case) (b) BER of a Heterodyne-Detected Single Data Channel: Triangle → Single Channel Modulation Case (CW injection locking without data), Circle → Multi-Channel Modulation Case (Pulsed injection locking with data). .....	78
Figure 47: Architecture of the overall spectrally phase-encoded optical CDMA (SPE-OCDMA) system based on synchronized MSLs. D: data modulation; OCDM: optical code-division multiplexing. ....	80
Figure 48: Schematic of the architecture of efficient coherent homodyne receivers for the SPE-OCDMA based on synchronized MSLs. (a) CPD (b) MCCD.....	82
Figure 49: 10-GHz external cavity grating-coupled MSL combined with a 20-GHz microring resonator interleaver. (a) conceptual diagram of 20-GHz frequency channel generation	

(b) optical spectrum of the 10-GHz hybridly MSL (c) optical spectrum of the filtered 20-GHz channels out of the 10-GHz MSL spectrum through the 20-GHz interleaver.....	84
Figure 50: Pulse measurements of the 10-GHz external cavity grating-coupled MSL system combined with the 20-GHz de-interleaver (a) sampling oscilloscope trace of the 10-GHz MSL pulse train before the 20-GHz de-interleaver (b) 20-GHz pulse train after the 20-GHz de-interleaver (c) intensity autocorrelation measurement of the 10-GHz MSL pulse before the 20-GHz de-interleaver (d) intensity autocorrelation measurement of the 10-GHz MSL pulse before the 20-GHz de-interleaver. ....	85
Figure 51: Experimental setup for the CPD and MCCD demonstration using a 10-GHz MSL (M1~M6: mirror; G: grating; SOA: semiconductor optical amplifier; TBPF: tunable bandpass filter; MZ: Mach-Zehnder intensity modulator; F1 and F2: fiber to free space launcher; BS: beam splitter; PC: polarization controller; HP: half wave plate; LP: linear polarizer; PD: photodetector; LPF: low pass filter; OSC: oscilloscope) .....	86
Figure 52: Schematic of the homodyne processes in CPD and MCCD (BS: beam splitter, M1 and M2: mirror, D1 and D2: photodetector).....	88
Figure 53: Experimental results of CPD and MCCD (a) SNR measurements of CPD and MCCD (Solid symbol: MCCD, open symbol: CPD) (b) eye diagrams of the direct detection of the initial signal and coherent homodyne detections (scale: 10mV/Div.) .....	90
Figure 54: Coherent gain versus LO power .....	91
Figure 55: Schematic of a balanced receiver system based on high-speed MSM photodetectors	94
Figure 56: Experimental results of CPD at the data rate of 2.5 Gbps (NRZ coded $2^{10}$ -1 long PRBS) (a) SNR measurements in the CPD (Different symbols stand for different measurements) and the corresponding eye diagrams (b) Coherent gain vs. LO power. ..	95
Figure 57: Schematic of laser frequency stabilization by polarization spectroscopy .....	107
Figure 58: Theoretical response of a reference cavity (a) the angle $\theta$ (b) the error signal .....	108
Figure 59: Schematic diagram of the Ridge Waveguide Laser Diode (RWLD) fabrication steps (VM: vertical mesa, RM: reverse mesa) .....	111
Figure 60: Reverse Mesa Ridge Waveguide Laser Diode (RM-RWLD) .....	113
Figure 61: Gain growth and Absorption band edge shift.....	114
Figure 62: RF performance of the RM-RWLD (a) External Cavity Hybridly Modelocked at 6.33GHz (b) 10 GHz modulated carrier by the electroabsorption modulator .....	115

Figure 63: Optical spectra of 6.33GHz hybridly modelocked external cavity RM-RWLD (a) undesirable modulation due to discontinuity effect (b) Undesirable modulation due to poor AR coating.....	115
Figure 64: Angled waveguide.....	116
Figure 65: Effective facet reflectivity of angled waveguide.....	117
Figure 66: Mask design for the improved RM-RWLD .....	118
Figure 67: Metallic pad design 1 (S: signal, G: ground).....	119
Figure 68: Metallic pad design 2 .....	120
Figure 69: Picture of the 1550 nm two-section SOA.....	122
Figure 70: LI (light output vs. current)-VI (bias voltage vs. current) characteristics of the two-section SOA .....	123
Figure 71: Wavelength tuning range of the grating-coupled laser in CW lasing (a) and hybrid modelocking (b).....	123
Figure 72: Optical spectrum, output power, and SNR of the amplified 6.33 GHz hybridly modelocked grating-coupled laser. ....	124
Figure 73: Picture of the 1550 nm commercial Covega SOA and home-made device mount...	125
Figure 74: Covega SOA characteristics.....	126
Figure 75: Essex hyperfine filter transfer function (a) unit1 (b) unit2. ....	127
Figure 76: Essex hyperfine filter shape function measurement (a) ASE throughput of a single channel window (b) Zoom-in filter shape.....	127
Figure 77: Schematic of the grating filter (G: grating, L: lens, S: slit, M: mirror, F: fiber launcher) .....	128

## LIST OF TABLES

Table 1 Typical energy and phase relaxation times of semiconductor and solid amplifiers .....	13
Table 2 List of Parameters used in the Simulations.....	16
Table 3 Typical Devices RIN .....	34

# CHAPTER 1: INTRODUCTION

## 1.1 Introduction

Recent advancements in the photonic systems toward high-capacity optical communications as well as ultrafast photonic signal processing are continuously demanding efficient optical sources which can provide reliable short optical pulses and a multiplicity of optical frequency combs with low intensity noise [1]-[3]. Beyond many scientific interests, mode-locked semiconductor lasers (MSLs) have been recognized as one of the most useful optical sources for many future photonic applications due to the ability to generate phase-coherent broadband optical frequency combs from a single device, producing optical pulses of extremely short duration on the order of picoseconds, as well as, compact integration flexibility [4]. Nonetheless, in the past years, it was very difficult to realize the practical use of the individual optical frequency combs from the MSL as potential optical carriers for various enabling photonic systems based on dense wavelength-division multiplexing (DWDM), due to the lack of optical channelization capabilities with a channel separation below 25 GHz.

The demand for many-user access systems, with enormous information traffic capacity and a relatively low bit rate per subscriber, has spurred remarkable advances in hyperfine optical filter design [5], [6]. Accordingly, as potential coherent optical carriers of information and synchronized local oscillators, broadband optical frequency combs from the synchronized MSL systems have recently been gaining strong interests in many coherent lightwave systems based on the advanced filter technologies.

Owing to the superb signal-to-noise ratio and narrow channel selectivity as compared to direct detection methods, the coherent detection is one of the most essential procedures in many

coherent lightwave systems. Nonetheless, most coherent mixing processes employed in the coherent detections require strict optical frequency and phase synchronization between the optical carriers from master lasers and slave lasers. In MSL systems, synchronization of multiple optical frequency combs at separate locations are very easily attainable by using optical injection locking techniques due to the strong initial phase coherency of the mode-locked spectral combs [7]. As compared with other techniques, optical injection locking is a very simple technique which does not require any active feedback control for phase tracking of a stable reference oscillator [8]-[11]. Recent, extensive works on optical injection locking have shown on admirably stable quality of oscillator synchronization in a wide range of applications such as coherent detection, dense optical frequency multiplexing, and low noise millimeter-wave carrier generation for radio-on-fiber systems [12]-[14].

Keeping toward the ideas on the practical utilization of phase coherent optical combs of a MSL system, this research mainly focuses on studies of the characteristics and intensity noise properties of high-speed MSL systems and demonstration of coherent detections for the ultra-dense-wavelength-division-multiple-access (UD-WDMA) systems, as well as, microwave photonic analog link systems in addition, essential subsystems for a secure coherent communication system based on optical code division multiplexing (O-CDM) technology.

## **1.2 Motivation and Dissertation Statement**

This dissertation is a study of high speed modelocked semiconductor lasers (MSLs), synchronized MSL systems and their feasibility for various coherent communication system applications, as well as high-speed photonic signal processing.



The challenges described in this dissertation are generation and synchronization of a multiplicity of optical frequency combs from two independent MSLs at separate locations, as well as, demonstration of many coherent optical detection subsystems utilizing the synchronized optical frequency combs from the MSLs for arrays of coherent carriers of information and arrays of local oscillators.

### **1.3 Overviews**

In this dissertation, I will present, in chapter 2, general features and characteristics of two different external cavity high-speed MSL systems, with respect to the generation of phase-coherent optical frequency combs and short pulses, Pound-Drever-Hall laser frequency stabilization, linewidth measurement. Theoretical modeling and simulation of the high-speed MSL systems are introduced with description on several key elements of modelocking. And details of relative intensity noise (RIN) characteristics of the MSL systems as well as measurement technique for the RIN are described.

In chapter 3, oscillator synchronization of independent MSLs and a tunable CW laser to a MSL is described. Experimental results of a novel injection locking method, called dual-mode injection locking technique for the synchronization of two independent MSLs and modulation sideband injection locking technique for a tunable CW laser to a MSL are described. Dynamic locking behavior and locking range are described based on theoretical study and experimental demonstrations.

In chapter 4, demonstration of coherent heterodyne detections using synchronized MSL systems are demonstrated for many coherent high-speed photonic system such as coherent

analog photonic links, broad- band coherent probe system, ultra-dense WDM systems, and finally, efficient homodyne balanced detection techniques for a spectrally phase-encoded optical CDMA (SPE-OCDMA) system based on synchronized MSLs, as one of the promising future secure coherent communication applications.

In chapter 5, a summary of this dissertation and suggestions of the future work are described.

Finally, several appendices describe a program for the simulation of MSL systems, laser frequency stabilization by polarization spectroscopy, and fabrication of an electro-absorption modulator incorporated two-section semiconductor optical amplifier and a reverse mesa ridge waveguide laser diode (RM-RWLD), characterization of semiconductor optical amplifiers and miscellaneous system elements.

## **CHAPTER 2: HIGH-SPEED MODELOCKED SEMICONDUCTOR LASERS**

### **2.1 Introduction**

A modelocked semiconductor laser (MSL) is a very attractive optical source which can generate broadband phase coherent optical combs producing stable pulses of light of extremely short duration, on the order of picoseconds before external compression [15]. Since early 1990s, numerous MSL systems have been introduced to demonstrate several key applications for the future optical high-data-rate communication systems based on time division multiplexing (TDM) technology, such as optical clock regeneration, gate switching, all-optical demultiplexing, and etc [16,17]. Furthermore, based on mature semiconductor IC technologies various advanced multi-section and multi-functional chip-scale monolithic MSL devices have been developed attracting remarkable attention as a next generation compact optical pulsed source for all-optical ultrafast signal processing applications. Because those chip-scale monolithic MSLs with as-cleaved mirror facets can easily generate short pulses with an extremely high repetition rate of over 100 GHz due to the shorter cavity length [18,19]. On the other hand, considering a large gain bandwidth of semiconductor laser materials many researchers have continuously attempted to utilize MSLs as a practical multiwavelength light source for broadband transmission systems based on wavelength division multiplexing (WDM) technology [3,20,21]. Multiwavelength semiconductor lasers always suffer severe mode partition noise (MPN) due to the gain competition between the laser longitudinal modes, which results in pulse-to-pulse amplitude fluctuations recognized as the relative intensity noise (RIN) of the laser source. However, recent investigation of multiwavelength generation with improved MSL systems has shown promising

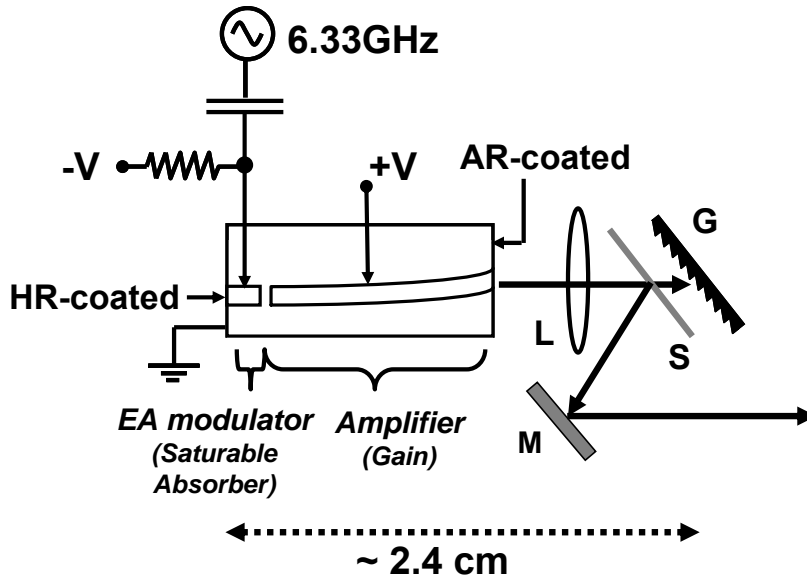
qualified features for photonic access network applications with significantly reduced MPN [22,23].

In the following sections, some of the important general features of the external cavity MSLs as well as the laser performance improvement in terms of intensity noise and frequency stabilization will be described in theoretical study and experimental demonstration.

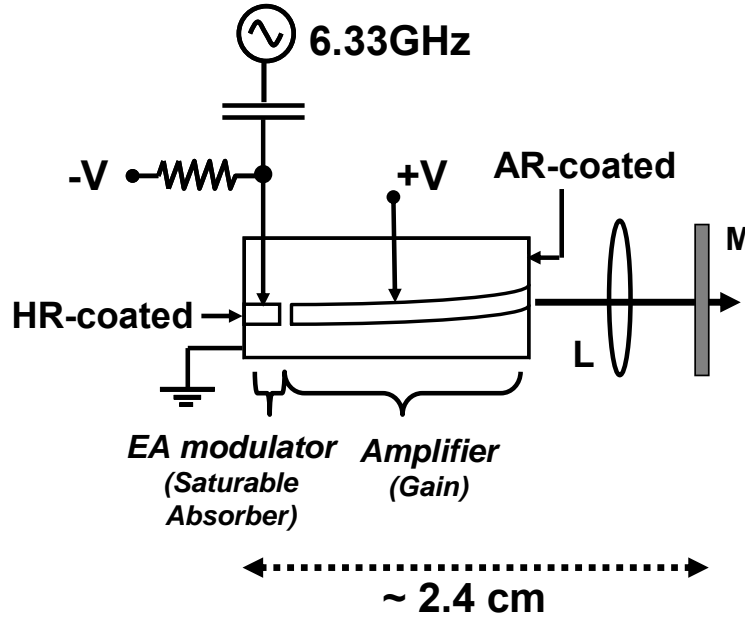
## **2.1 External Cavity Modelocked Semiconductor Lasers**

### **2.1.1 General Features of the High-Speed MSLs**

*1) Cavity configurations:* In this work, two different external cavity MSLs were configured to use as a master laser and a slave laser for our coherent detection systems. Figure 1 shows the schematic of the cavity configurations of a grating-coupled MSL and a mirror-coupled MSL. Pictures of the external cavity high-speed MSL systems and cavity configurations are shown in Figure 2. In both lasers, saturable absorber (SA) incorporated two-section devices are used as semiconductor optical amplifiers for the external cavity MSL systems. The gain section of the device is designed as a curved waveguide terminating at an angle of  $7^\circ$  relative to the normal direction of the facet [24]. Antireflection coating is applied on the facet to eliminate possible residual reflection originated from the device itself. The other facet on the SA section is coated to have high reflection ( $>90\%$ ) at the wavelength of 1550 nm. Details of the basic characteristics of the device is described in the appendix D. Cavity length of the both MSLs was set up for a fundamental cavity frequency of 6.33 GHz which corresponds to  $\sim 2.4$  cm, in order to match with a available hyperfine WDM filter with a periodic frequency grid of 6.33 GHz in



(a)

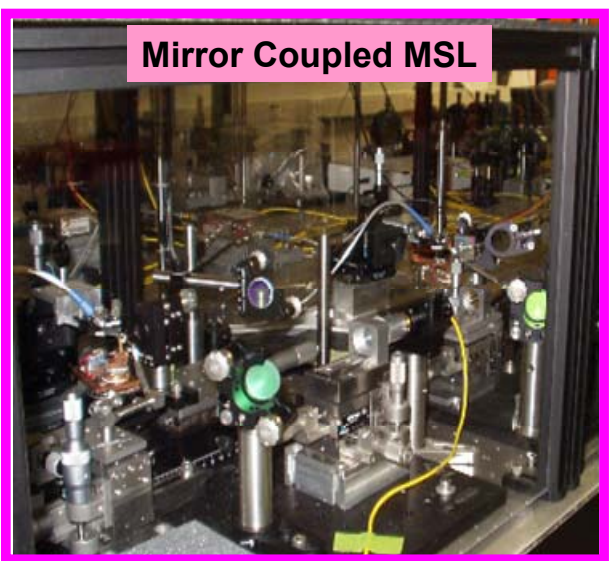


(b)

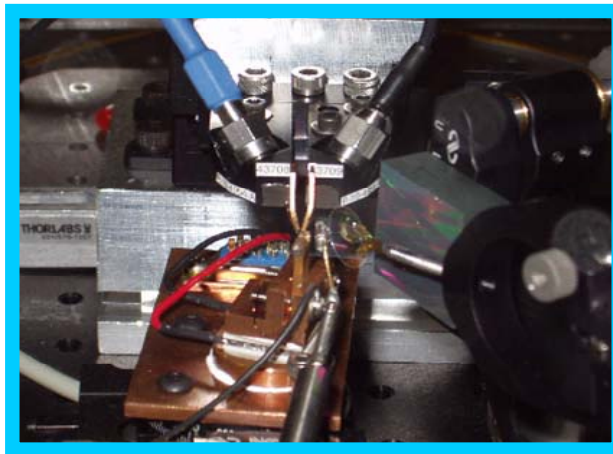
Figure 1: Schematic of the external cavity high-speed MSL cavity configurations. (a) a grating-coupled MSL (b) a mirror-coupled MSL. L: lens; G: grating; M: mirror; S: optical sampler.



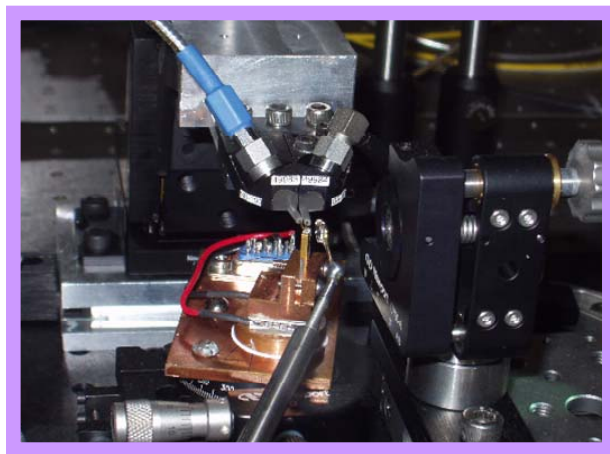
(a)



(b)



(c)



(d)

Figure 2: Pictures of the external cavity high-speed MSL cavity configurations. (a) the grating-coupled MSL system (b) the mirror-coupled MSL system (c) the grating-coupled MSL cavity configuration (d) the mirror-coupled MSL cavity configuration.

further coherent detection experiments. The grating-coupled MSL was hybridly mode-locked by applying a DC current of 78 mA on the gain section of the monolithic two-section device and a reverse bias of 2.4 V with a 6.33 GHz RF signal of 23 dBm on the saturable absorber (SA) section of the device. Phase coherent optical frequency combs at 6.33 GHz was obtained from the optical feedback between the device facet with high reflection (HR) coating and a grating with a groove density of 600 lines/mm.

**2) General features:** Figure 3 (a) shows the optical spectra of the laser carrier of the 6.33 GHz hybridly grating-coupled MSL, respectively. Due to the grating coupler, a narrow 3-dB spectral bandwidth of  $\sim 0.6$  nm was obtained from the grating-coupled MSL. However, higher spectral power of the optical frequency combs, as well as, wavelength tenability for flexible experimental facilitation was obtained from the grating-coupled MSL. On the other hand, the mirror coupled MSL was operated in a passively mode-locked state with a DC current of 80 mA on the gain section and a reverse bias of 2.5 V on the EA modulator section of the device.

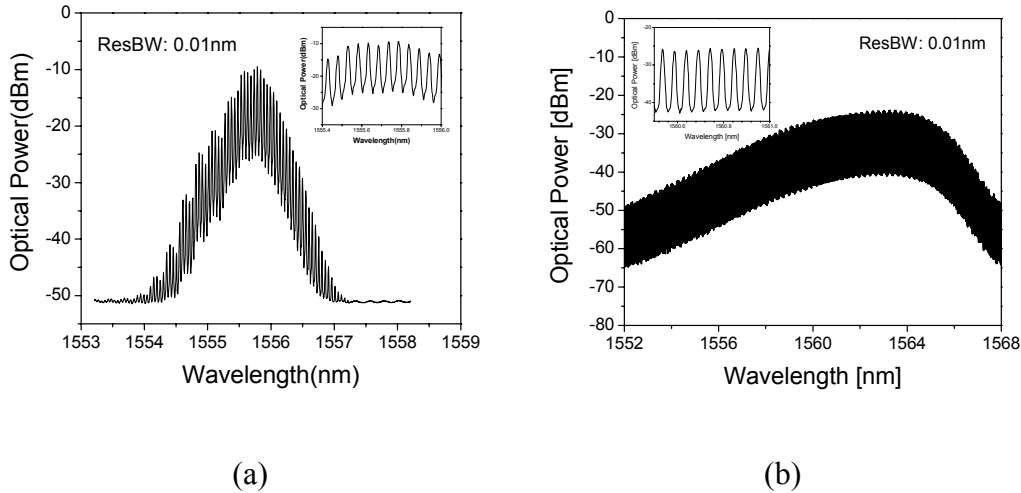


Figure 3: Optical spectra of the 6.33 GHz external cavity MSLs (a) grating-coupled MSL (hybridly modelocked) (b) mirror-coupled MSL (passively modelocked)

In the mirror-coupled MSL, a 70 % partial reflection mirror was used to make laser feedback with the HR-coated facet of the device. Broadband optical coating on the output coupler mirror surface fully covers the entire gain bandwidth of the laser chip and allows the laser to produce  $\sim 3$  nm bandwidth of mode-locked laser spectrum, as shown in Figure 3 (b). The corresponding RF spectra of both external cavity MSLs are shown in Figure 4. Due to the nature of phase

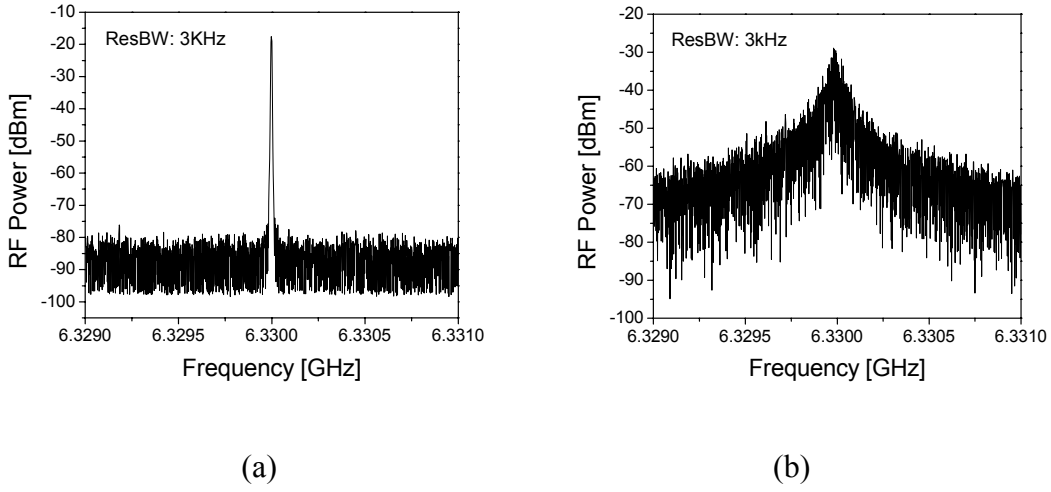


Figure 4: RF spectra of the 6.33 GHz external cavity MSLs (a) grating-coupled MSL (hybridly modelocked) (b) mirror-coupled MSL (passively modelocked)

uncertainty the 6.33 GHz laser carrier from the passively modelocked mirror-coupled MSL shows large phase noise of the carrier. Whereas the laser carrier from the hybridly modelocked grating-coupled MSL, subject to the stability of an external RF source, reveals significantly reduced phase noise sidebands. Figure 5 shows the intensity autocorrelation measurements of both 6.33 GHz external cavity MSLs. After fitting with a  $\text{sech}^2$  pulse shape function, the pulse durations were estimated to be 9.1 ps from the hybridly mode-locked grating-coupled laser, and 4.6 ps from the passively mode-locked mirror-coupled laser. Usually, the shortest pulse possible can be obtained by the passive modelocking but the pulses suffer large timing jittering due to the



random nature of time gating process [25]. This is the origin of a significant phase noise in the resonance carrier of the passively mode-locked lasers, as shown in Figure 4 (b). In the hybridly modelocking, since the active incursion of RF signal on the SA section improves stability on the time gating process, the produced pulses are much more stable than those pulses in the passive

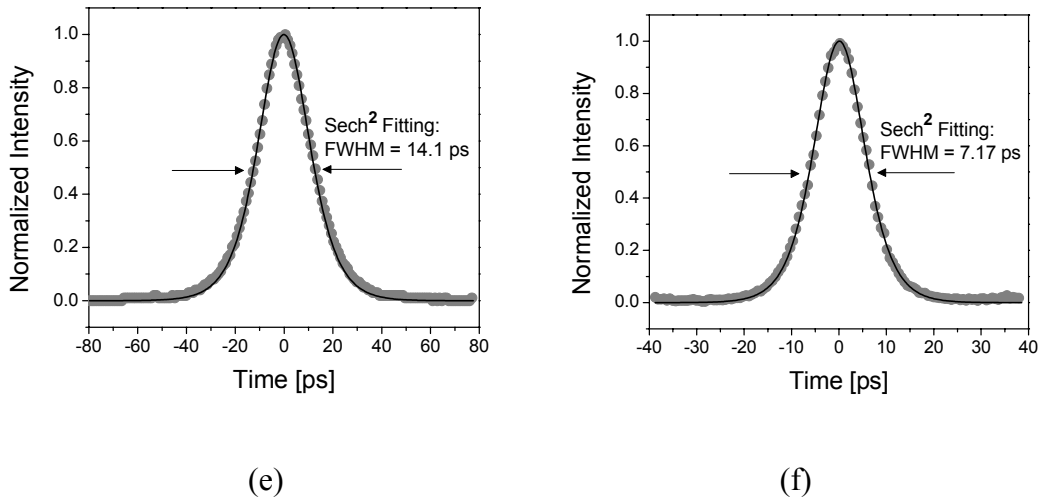


Figure 5: Intensity autocorrelation of the 6.33 GHz external cavity MSLs (a) grating-coupled MSL (hybridly modelocked) (b) mirror-coupled MSL (passively modelocked)

modelocking. The stable RF carrier indicates the improved stability in the hybrid modelocking, as shown in Figure 4(a).

### 2.1.2 Theory of High-Speed MSLs

In the previous chapter, the generation of optical pulses with duration of  $\sim 10$  ps from the external cavity MSL systems based on the monolithic two-section devices was experimentally demonstrated. In this chapter, some of the key physical backgrounds in optical pulse generation

from the MSL systems are studied by numerical simulation. Most of the theoretical foundation of the equations and the relations described in this chapter is referred from the reference book [26 and 27].

### **Saturable Gain and Absorption**

In order to simplify the modeling our MSL systems, a limited case where the pulse duration is much shorter than energy relaxation time ( $T_1$ ) of a semiconductor medium and much longer than the phase relaxation time ( $T_2$ ) of the medium is considered, as described in the reference [26].

Under these conditions, we can use the rate equation approximation describing the saturable gain and absorption processes for an incoming optical pulse to the semiconductor medium, as following expression

$$E(t) = E_{in}(t) \cdot \sqrt{\frac{e^{s \cdot W(t)}}{e^{-a} - 1 + e^{s \cdot W(t)}}} \quad (2.1)$$

where  $E_{in}(t)$  is the input optical pulse,  $E(t)$  is the output optical pulse through the semiconductor medium,  $W(t)$  is the integrated pulse energy ( $= \frac{1}{\hbar \omega} \int_{-\infty}^t I_{in}(t') dt'$ ),  $a$  is the amplification ( $a > 0$ ) or absorption coefficient ( $a < 0$ ),  $s$  is the saturation parameter which is given by

$$s = 2\sigma \cdot W(t) = \frac{\mathcal{E}_p}{\mathcal{E}_{sat}} \quad (2.2)$$

where  $\sigma$  the interaction cross section. The parameter  $s$  describes the ratio of incoming pulse energy  $\epsilon_p$  to saturation energy  $\epsilon_{sat}$  of the medium. With increasing the saturation parameter  $s$  the change in pulse shape can be significant. For a short optical pulse generation using the two-section devices, the saturation energy of the gain section and the SA section must satisfy the following relations.

$$\epsilon_{sat}^{gain} > \epsilon_{sat}^{SA} \quad (2.3)$$

For the simulation, the coefficient  $a$  was specifically described by coefficient  $g$  for the small signal gain of amplification process and coefficient  $L$  for the absorption coefficient of saturable absorption process. Similarly, the coefficient  $s$  was specifically described by  $s1$  for gain saturation and  $s2$  for SA saturation.

Table 1

Typical energy and phase relaxation times of semiconductor and solid amplifiers

Medium	T1 [sec]	T2 [sec]
SOA	$10^{-4} \sim 10^{-12}$	$10^{-12} \sim 10^{-14}$
Soild Amplifiers	$10^{-3} \sim 10^{-6}$	$10^{-11} \sim 10^{-14}$

### **Self-Phase Modulation (SPM)**

A temporal change of gain causes the temporal change of index of refraction through Kramers-Kronig relationship and the variation of index of refraction results in change of instantaneous frequency  $\Delta\omega_{inst}$ , as given by

$$\Delta\omega_{inst} = -\frac{\omega \cdot L}{c} \cdot \frac{\partial n(t)}{\partial t} \quad (2.4)$$

This effect is typically referred to self-phase modulation (SPM). The dynamic change in optical pulses propagating through a semiconductor gain medium caused by the SPM can be described by

$$E(t) = E_{in}(t) \cdot e^{i \cdot n_{SPM} \cdot W(t)} \quad (2.5)$$

where  $n_{SPM}$  is the SPM coefficient.

### **Group Velocity Dispersion (GVD)**

When optical pulses propagate through dispersive media such as semiconductor media, each of spectral components in the pulse will experience different traveling speed which results in temporal broadening of the pulse width. This effect can be governed by

$$E(\omega, z) = E_{in}(\omega, 0) \cdot e^{ik'' \cdot z \cdot (\omega - \omega_0)^2} \quad (2.6)$$

where  $E_{in}(\omega, 0)$  and  $E(\omega, z)$  is the amplitude of pulse spectrum before and after propagation through the medium at a propagation length of  $z$ ,  $k''$  is the GVD parameter ( $= \frac{d^2 k}{d\omega^2}$ ). In the

simulation the GVD parameter was described by  $k_1$  and  $k_2$ .

### 2.1.3 Numerical Modeling and Simulation of High-Speed MSLs

#### Numerical Modeling

Figure 6 shows the schematic diagrams of equivalent systems and numerical simulation modeling of the external cavity MSL systems. Our MSL systems can be simply considered as a two-section monolithic laser diode structure which has gain and SA sections considering

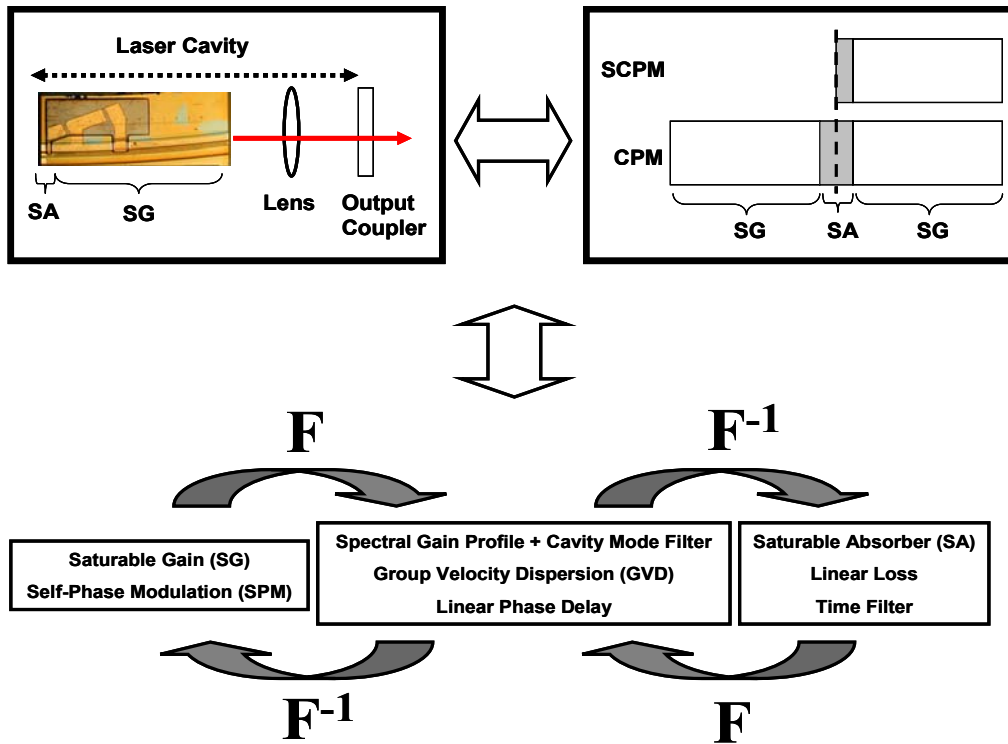


Figure 6: Schematic diagram of equivalent systems and numerical simulation modeling of the external cavity MSL systems (SCPM: self-colliding pulse modelocking, CPM: colliding pulse modelocking)

effective dispersion in the laser system. The unfolded structure from the simplified MSL system is also equivalent to a monolithic colliding pulse mode-locked laser [19,28], as illustrated in the figure 6. In this simulation, a slit-step Fourier method was used to simulate optical pulse formation based on this simplified MSL model. Key elements for the simulation are saturable gain (SG), self-phase modulation (SPM), spectral gain profile function, cavity mode filter, group velocity dispersion (GVD), linear phase delay, saturable absorber (SA), linear loss, and time filter. The spectral gain function is considered for describing a limited spectral gain. The time filter is considered for the time gating mechanism of the saturable absorber in passive modelocking. List of parameters used in this simulation is shown in Table 2. The MATLAB program for this simulation is attached in the appendix A.

Table 2

List of Parameters used in the Simulations

Parameters	Symbol	Value
Small Signal Gain Coefficient	$g$	2.9
Absorption Coefficient	$L$	-1.9
Gain Saturation Parameter	$s_1$	$2.6e-4$
SA Saturation Parameter	$s_2$	$1.2e-3$
SPM coefficient	$n_{\text{spm}}$	$3.2e-3$
GVD parameter	$k_1, k_2$	$1.2e-3$
Linear Loss	$L_1$	0.2
Linear Phase Delay	$L_{\text{pd}}$	$-0.09e-3$

## Simulation Results

It should be mentioned that considering pulses with duration of  $\sim 10$  ps in the MSL systems fast dynamic processes such as carrier heating and others on the order of femtosecond scale were neglected in this simulation. In order to reduce calculation time total span of frequency window was limited to 1024 GHz. The repetition rate of the MSL system for this numerical study was set at 5 GHz. The width of the spectral band-pass filter is  $\sim 200$  GHz. The linewidth of the cavity mode filter is defined as 50 MHz, based on the Lorentzian lineshape function. In the cavity mode filter 41 wavelength channels with a frequency spacing of 5 GHz are defined to fit in the window of the spectral band-pass filter. Figure 7 shows the input noise spectrum and the spectral band-pass filter window. Total number of iteration was 50. Starting from the noise input, stable output laser spectrum and pulses were developed after 10 times of iteration.

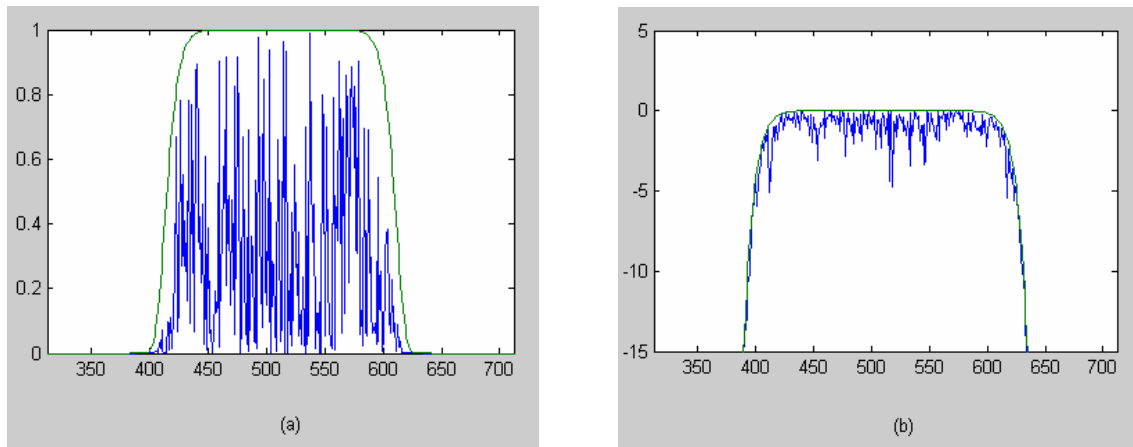


Figure 7: Input noise spectrum and spectral band-pass filter (solid curve) (a) Linear scale (b) Log scale

Figure 8 and 9 shows the simulation results of this MSL model. Time evolution of the optical spectra of the laser system is shown in Figure 8 (a) and (b). The output laser spectrum is shown in Figure 8 (c) and (d). From the simulation result, the bandwidth of the output spectrum was estimated to be  $\sim 35$  GHz ( $= 0.28$ nm).

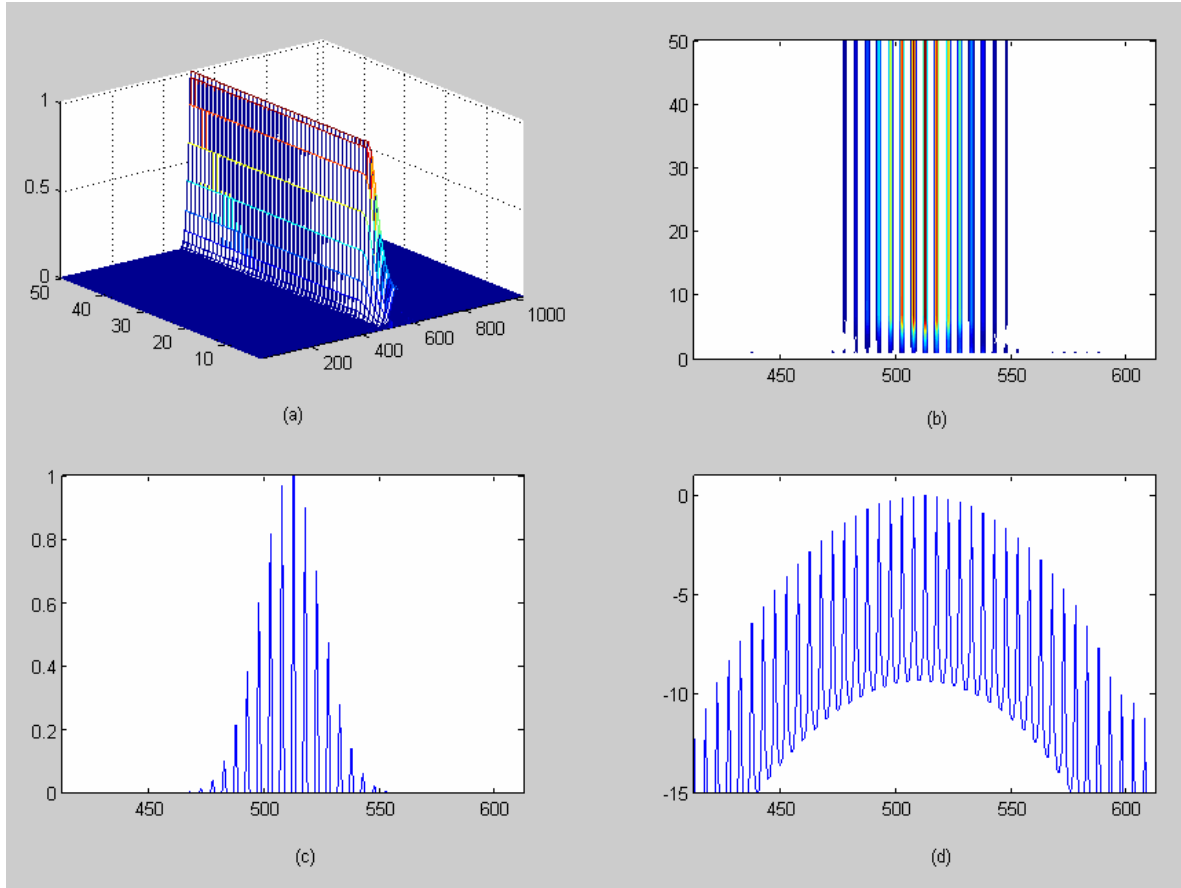


Figure 8: Output laser spectra (a) time evolution of the laser spectrum (3D mesh plot) (b) time evolution of the laser spectrum (contour plot) (c) output laser spectrum after 50 times iteration (Linear scale)(d) output laser spectrum after 50 times iteration (Log scale)



Time evolution of the optical pulses from the laser system is shown in Figure 9 (a). The optical pulses train is shown in Figure 9 (b). The output optical pulse after 50 times iteration is shown in Figure 9 (c). and (d). From the simulation results, the FWHM of the output pulse was estimated to be  $\sim 24$  ps. The time-bandwidth product of the simulated output pulse was  $\sim 0.84$ , which corresponds to approximately 2 times transform limited.

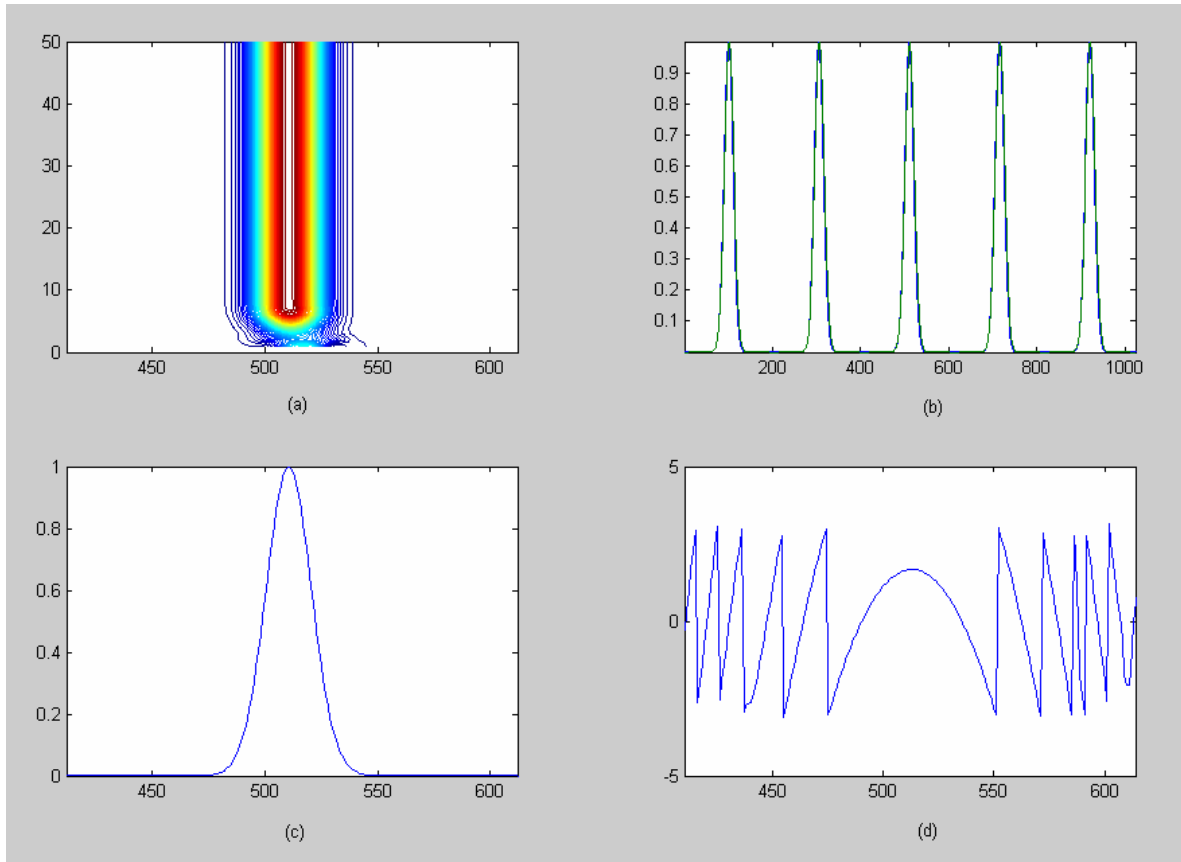


Figure 9: Output optical pulses (a) time evolution of optical pulses (3D contour plot) (b) pulse trains (c) optical pulse output (d) temporal phase of the optical pulse

## **2.2 Laser Frequency Stabilization**

### **2.2.1 The Pound-Drever-Hall (PDH) Technique**

In most photonic applications, frequency stability of optical sources is one of the most essential issues. Due to the well-defined phase coherent periodic axial modes subject to an external RF source stability, as well as, relatively lower RIN level, we have decided to use the hybridly mode-locked grating-coupled laser as a master laser, a transmitter for the rest of the coherent detection experiments. However, the axial modes wander in frequency suffering from effective cavity length variation due to mechanical vibration, temperature drift, injection current fluctuation, etc.

In order to stabilize the optical frequency combs of the MSL, the Pound-Drever-Hall (PDH) frequency stabilization technique is employed as shown in Figure 10 [29]. This PDH technique uses a reference cavity with high finesse for the laser frequency locking to it. When a laser beam is reflected from the reference cavity (etalon), phase of the reflected beam experiences relative change from  $-\pi$  to  $\pi$  across the etalon resonance frequency. The reflection coefficient with respect to the reference etalon is given by

$$F(\nu) = \frac{r \cdot \left[ \exp\left(i \cdot \frac{\nu}{\Delta\nu_{FSR}}\right) - 1 \right]}{1 - r^2 \cdot \left[ \exp\left(i \cdot \frac{\nu}{\Delta\nu_{FSR}}\right) \right]} \quad (2.7)$$

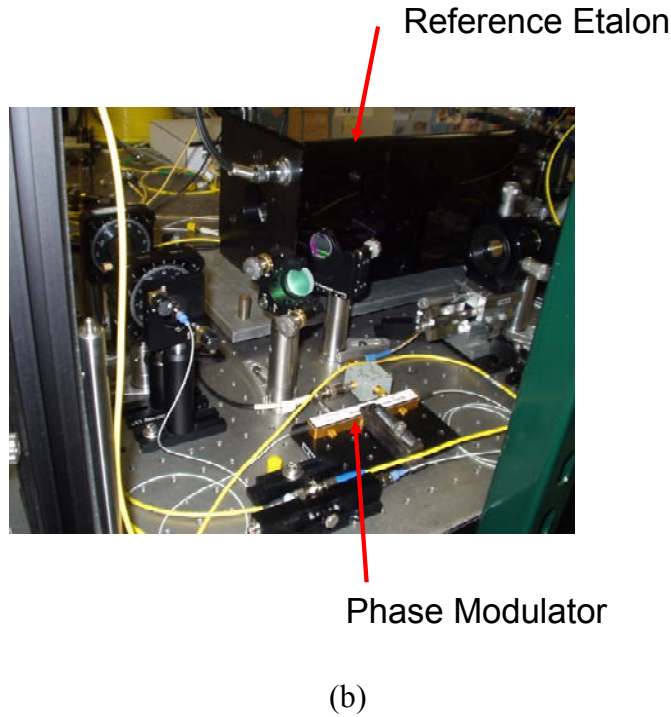
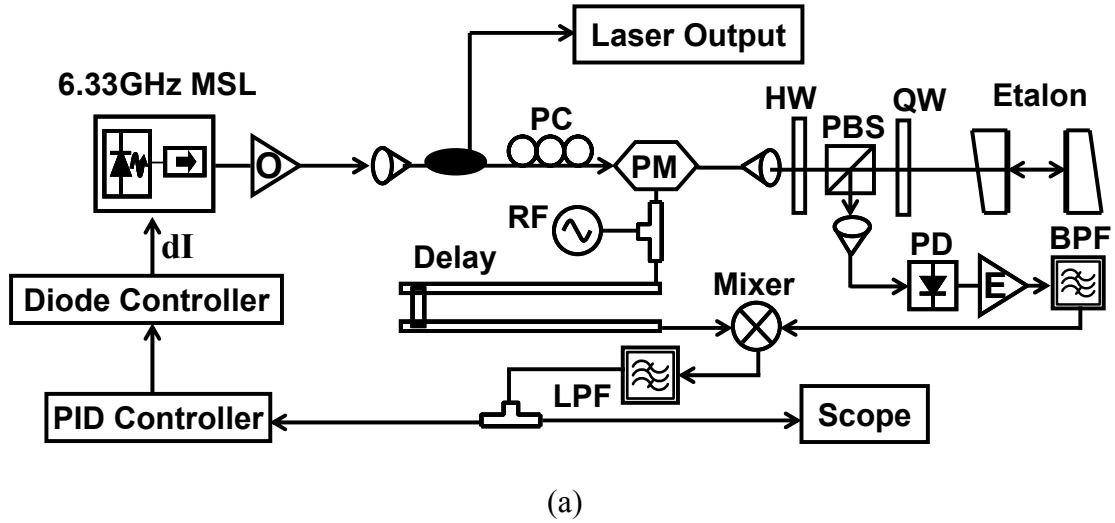


Figure 10: Schematic of the Pound-Drever-Hall laser frequency stabilization Setup. (a) schematic (b) picture of real system, O: optical amplifier; PC: polarization controller; HW: half-wave plate; PBS: polarizing beam splitter; QW: quarter-wave plate; PD: photodetector; E: electrical amplifier; BPF: band-pass filter; LPF: low-pass filter.

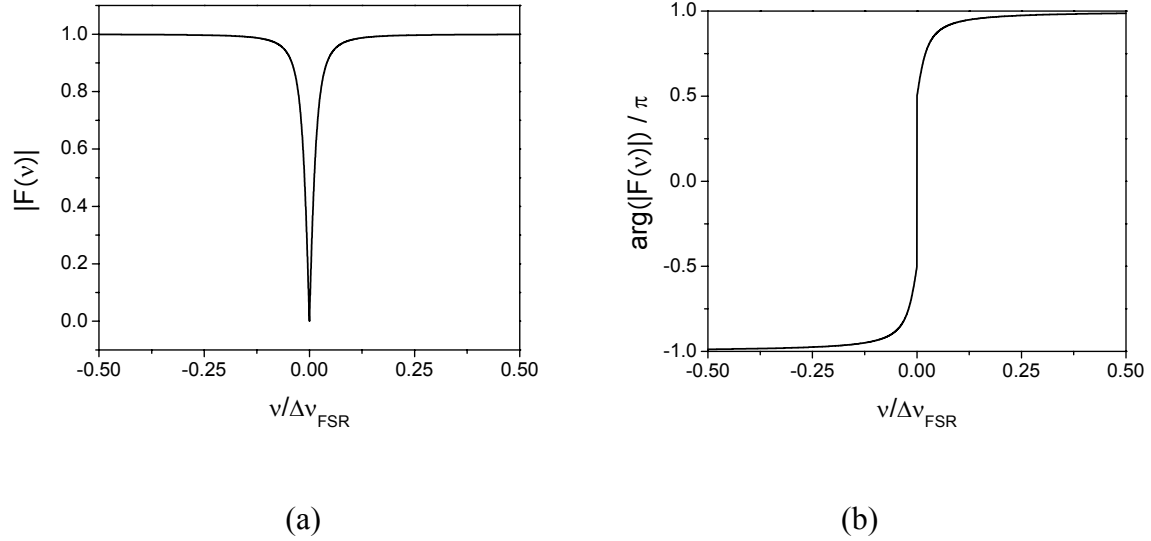


Figure 11: Plot of the magnitude and phase of the reflection coefficient of the reference etalon (a) magnitude (b) phase.

where  $r$  is the reference etalon mirror reflectivity,  $\nu$  is the optical frequency,  $\Delta\nu_{FSR}$  is the free spectral range of the reference etalon. Plot of the magnitude and phase of the reflection coefficient of the reference etalon is shown in Figure 11. Through phase modulation of the laser beam at a certain frequency, the generated modulation sidebands can be served as probes to show the amount as well as the sign of frequency detuning of the laser beam with respect to the resonance frequencies of the reference etalon. The photodetected power of the reflected beam is given by

$$\begin{aligned}
 P_{ref} = & P_c (|F(\nu)|)^2 + P_s \cdot [(|F(\nu + f)|)^2 + (|F(\nu - f)|)^2] \\
 & + 2\sqrt{P_c P_s} \cdot \left( \begin{aligned} & \text{Re}[F(\nu) \cdot F(\nu + f)^* - F(\nu)^* \cdot F(\nu - f)] \cdot \cos(f \cdot t) \\ & + \text{Im}[F(\nu) \cdot F(\nu + f)^* - F(\nu)^* \cdot F(\nu - f)] \cdot \sin(f \cdot t) \end{aligned} \right) \quad (2.8)
 \end{aligned}$$

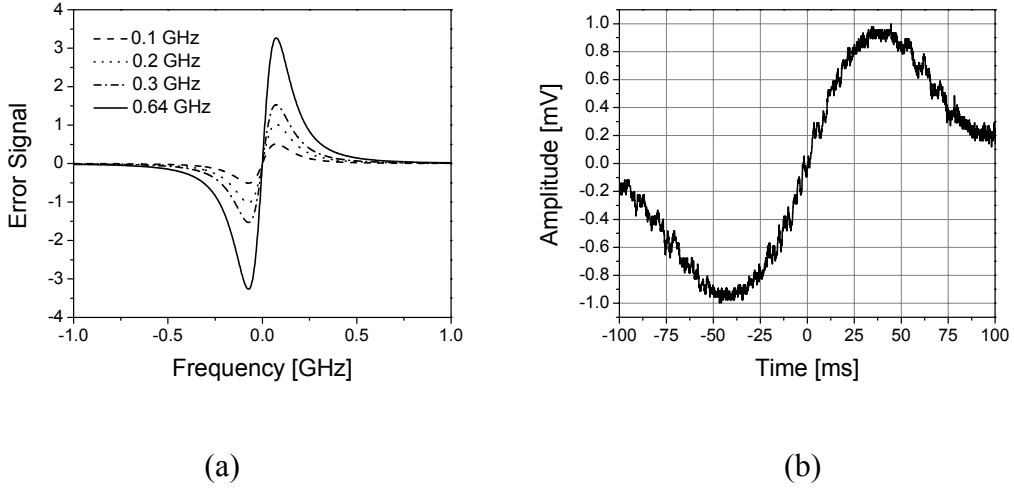


Figure 12: The PDH error signal (a) theoretically calculated (b) experimentally measured (modulation frequency: 640MHz)

where  $P_c$  is the carrier power,  $P_s$  is the power of the first-order sideband,  $f$  is the modulation frequency. The cross term that are oscillating at the modulation frequency  $f$  contains the phase information of the reflected carrier. With a slow modulation frequency the PDH error signal can be simply described by the following expression.

$$\varepsilon(\nu) \approx \left[ \frac{d}{d\nu} (|F(\nu)|)^2 f \right] \quad (2.9)$$

The calculated error signal and the measured error signal are shown in Figure 12. As shown in Figure 10 (a), the mixer compares the modulation signal with the output of the photodetector, extracting the part that is at the same frequency as the modulation signal. (The mixer's output is just the product of its inputs.) The sign of the mixer's output is different on either side of

resonance, and it is zero when the system is exactly on resonance. This is just what we want for a feedback control signal.

### **2.2.2 Frequency Stabilized MSLs**

In this PDH system, a phase-modulation frequency of 640 MHz is used to sample the phase of the reflected beam from the reference etalon. An error signal, reflecting the amount of frequency detuning with respect to the reference frequency of a flat surface FP etalon with a finesse of 312, is obtained from the low frequency component of the mixer output, as shown in Figure 10 (a). The error signal is fed back to control injection current on the gain section of the device through a phase-lock loop circuit to adjust the laser cavity frequency. Figure 13 shows transmission measurement of the laser output with respect to the reference etalon before and after the PDH frequency stabilization. Within the time period that the PDH control was on, stable control was clearly demonstrated. Figure 14 and 15 shows the comparison results of the PDH frequency stabilization. After the laser frequency stabilization, multiple sweeps over 30 minutes under a max-hold operation the optical spectrum showed almost identical spectrum that has been obtained from a single sweep, whereas before the laser frequency stabilization, a severe frequency drifting was observed in the optical spectrum, as shown in Figure 14 (a) and (b). In order to measure the optical comb frequency drift, the heterodyne mixing technique was used. A tunable laser output with 100 kHz narrow linewidth was heterodyned with one of the MSL axial modes to produce beat signals.

Similarly, under a max-hold operation, the heterodyne beat signals were recorded by an electrical spectrum analyzer (HP5566B). When the MSL is free-running, wandering beat signals

swept over more than 1.5 GHz after an elapse of 30 seconds, as shown in Figure 15 (a). However, by providing the PDH frequency control the comb frequency drift was completely locked within 350 MHz over 30 minutes, as shown in Figure 15 (b).

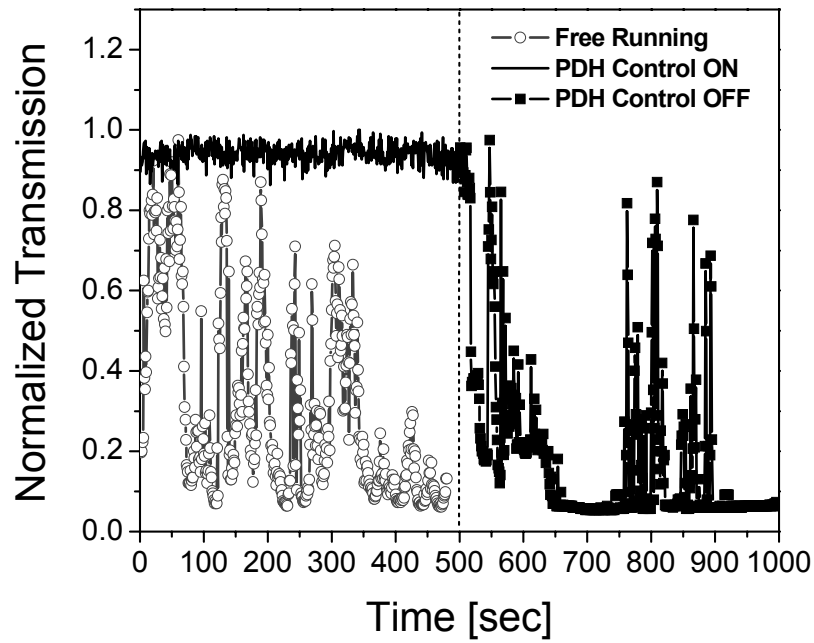
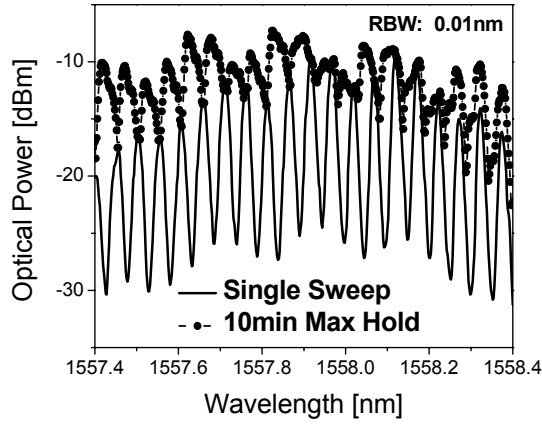
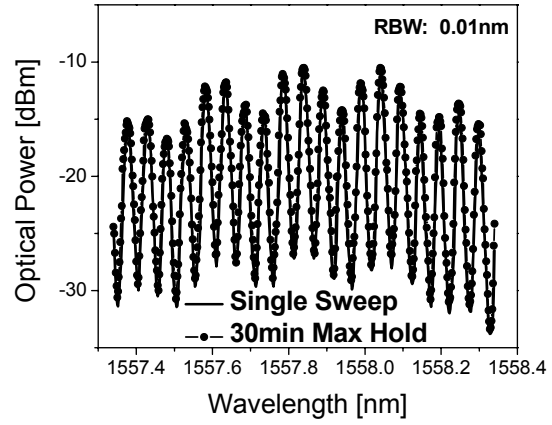


Figure 13: Transmission measurement of the laser output with respect to the reference etalon before and after the PDH frequency stabilization

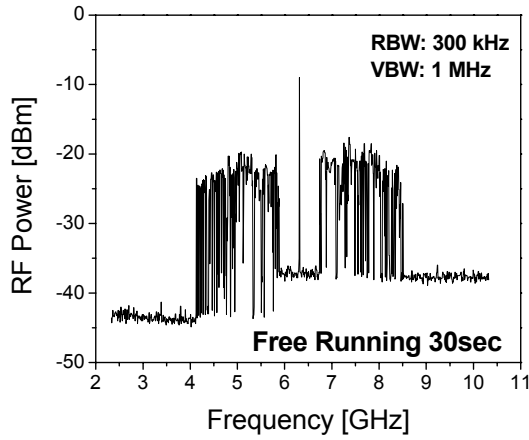


(a)

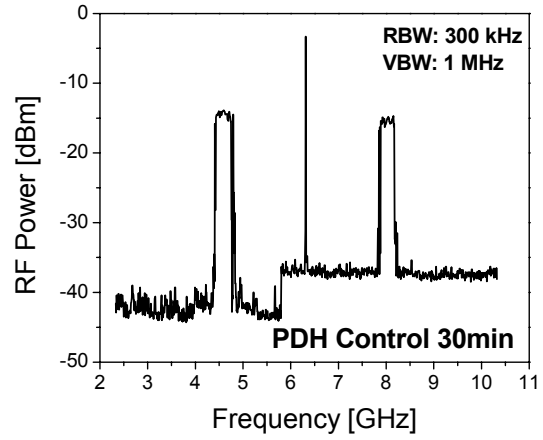


(b)

Figure 14: Comparison of optical spectra before and after the PDH laser frequency stabilization (a) before stabilization (b) after stabilization



(a)



(b)

Figure 15: Optical comb frequency drift measurement with the heterodyne mixing technique (a) before PDH frequency stabilization (b) after stabilization



## **2.3 Linewidth**

### **2.3.1 Linewidth of MSLs**

Even though there has been many theoretical and experimental studies on the linewidth of semiconductor lasers under passive and active (or hybrid) mode-locking operation, the physical origin of the linewidth has not been clarified yet. The linewidth of the axial (longitudinal) modes of a MSL is much broader than the Schawlow-Townes linewidth [70]. This is mainly due to the linewidth enhancement factor  $\alpha$  of the gain medium. In typical multiple quantum well semiconductor gain medium, the value of  $\alpha$  parameter is 2.0-6.0. Furthermore, there are other factors to make an impact on the increase of linewidth of MSLs, such as 1) phase noise induced directly by spontaneous emission noise, 2) phase noise induced by the amplitude fluctuation due to timing jitter and frequency detuning [71, 72]. The latter phase noise described is closely related to the effective cavity length variations due to environmental factors such as mechanical vibration, temperature drift, injection current fluctuation, etc. As shown in the previous section, the frequency stabilized laser has shown a significant improvement of axial mode frequency stability. In the following section, since physics behind the linewidth enhancement issues are beyond the scope of this dissertation, a linewidth measurement technique and the experimentally measured linewidth of a frequency stabilized MSL will be mainly discussed.

### **2.3.2 Linewidth Measurement by Delayed Self-Heterodyne Technique**

Linewidth of the modelocked laser was measured by using well-known delayed self-heterodyne technique [30]. All the linewidth measurements in this work are obtained under PDH

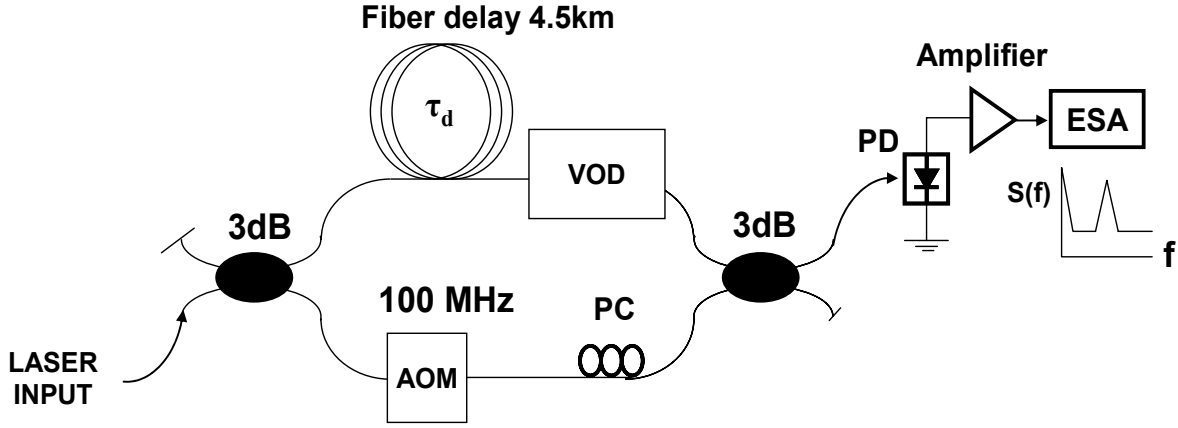


Figure 16: Experimental setup of the delayed self-heterodyne linewidth measurement

laser frequency stabilization in order to reduce the effect of linewidth broadening caused by any frequency jitter of the laser. The schematic of the linewidth measurement setup is shown in Figure 16. A 16-channel hyperfine WDM filter (ESSEX Hyperfine WDM) with a grid space of 6.33 GHz and a channel crosstalk of around 15 dB was used to separate a single axial mode from the MSL, as shown in Figure 17 (a). The filter shape function measurement is attached in the appendix D. The filtered single axial mode from the frequency stabilized MSL is shown in Figure 17 (b). Optical frequency shift of the delayed self-heterodyne technique was obtained by using an acousto-optic modulator with a resonance frequency of 100 MHz.

Validity of the delayed self-heterodyne technique is based on incoherent mixing of the signal and the delayed self-hetero signal. A minimum delay requirement for the interferometer in the technique must satisfy the following relation:

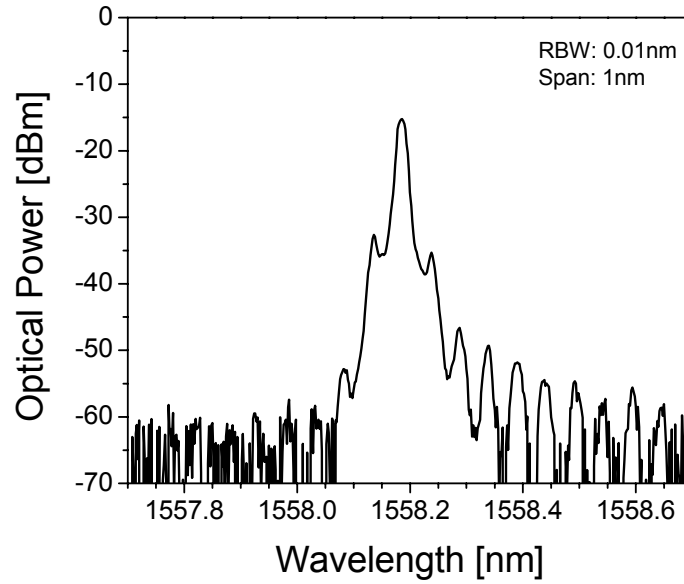
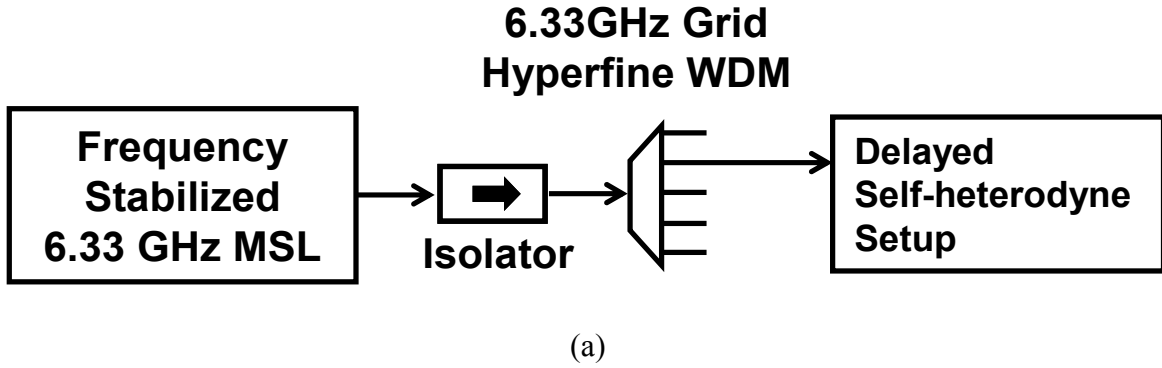


Figure 17: Single axial mode filtering for the linewidth measurement (a) setup for the single axial mode filtering (b) optical spectrum of the filtered single axial mode from the frequency stabilized 6.33 GHz grating-coupled MSL.

$$\tau_d \geq \frac{1}{\Delta\nu} \quad (2.10)$$

where  $\Delta\nu$  is the linewidth of the laser and the  $\tau_d$  is the delay time due to the single mode fiber. In order to obtain fully incoherent heterodyne beating a fiber delay length was provided as long as 4.5km which corresponds to 21.7 usec delay. The resolution of the measurement is given by [31]

$$\Delta \approx \frac{0.5}{\tau_d} \quad (2.11)$$

The measurement system resolution was estimated to be 23 kHz. Figure 18 shows the heterodyning processes in the delayed self-heterodyne technique. The incoherent mixing of the laser signal and delayed self-hetero signal is measured by photocurrent power spectral density, given by [32]

$$S(f) \sim R^2 [S_{dir}(f) + 2\{S(\nu - \delta\nu) \otimes S(-\nu)\}] \quad (2.12)$$

The first term is the direct detection of the laser spectrum and the second term is the desired mixing product. The incoherent beating signal was recoded by using a photodetector with a high responsivity of 0.7 A/W combined with a low noise electrical amplifier with a gain of 17 dB through 100 kHz to 1 GHz through HP8566B electrical spectrum analyzer (ESA). The linewidth measurement of a commercial DFB laser and the frequency stabilized MSL is shown in Figure 19. The measured experimental results revealed that the measured lineshape has good agreement with respect to a Lorentzian line shape function. From the fitting results, the linewidth of a

commercial DFB laser was measured to be 26.5 MHz and that of the external cavity MSL was ~ 3 MHz.

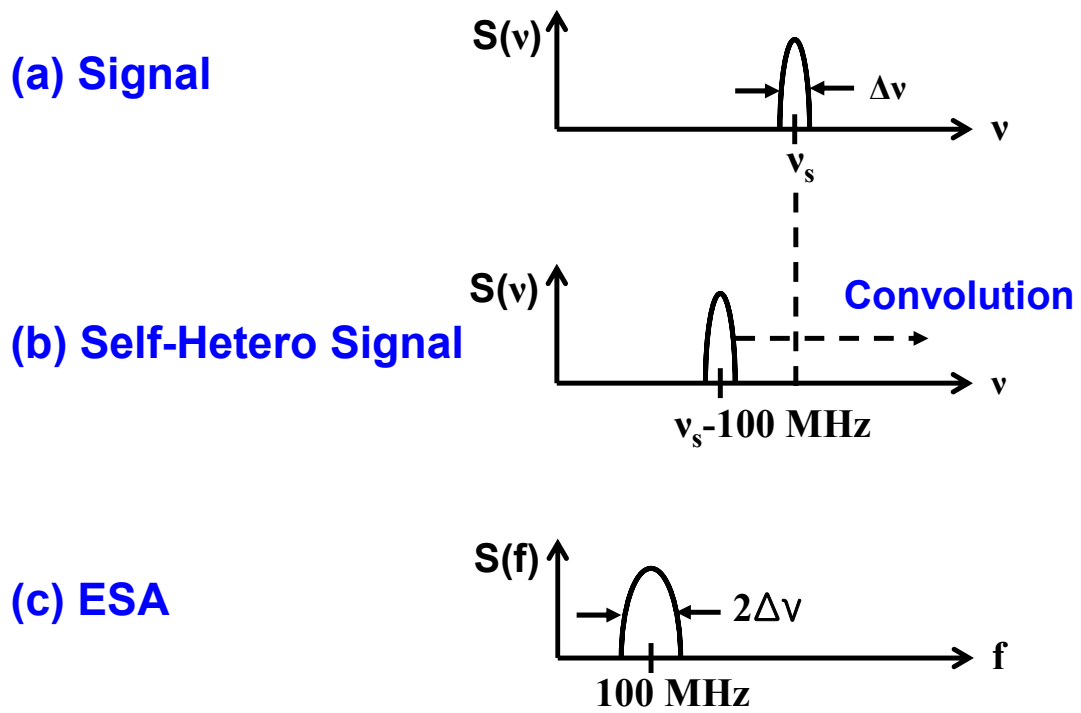
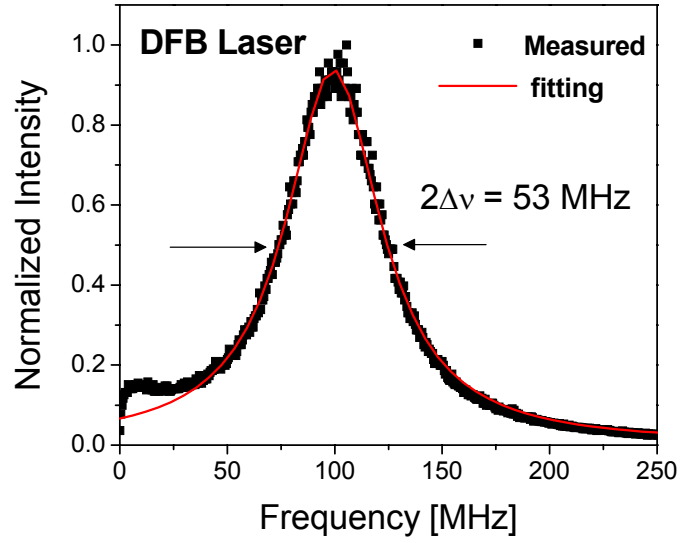
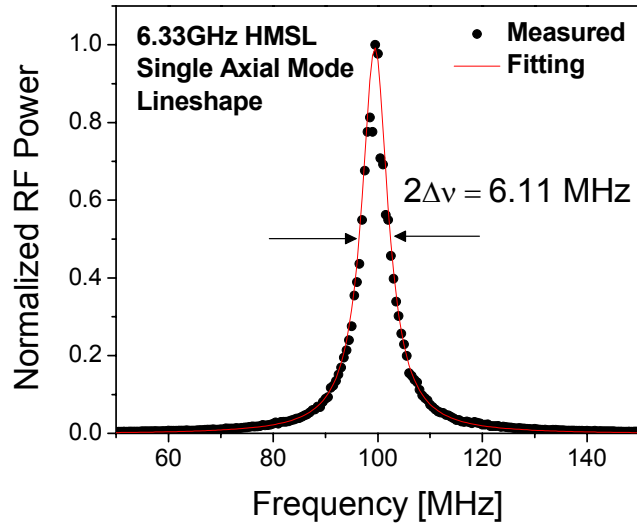


Figure 18: Heterodyning process in the delayed self-heterodyne technique.



(a)



(b)

Figure 19: The linewidth measurement using delayed self-heterodyne technique (a) Linewidth measurement of a commercial DFB laser (b) Linewidth measurement of the frequency stabilized MSL

## **2.4 Relative Intensity Noise (RIN)**

### **2.4.1 Introduction of Relative Intensity Noise (RIN)**

Considering an optical source, temporal power fluctuations of the source can be conveniently expressed in terms of the power spectral density function in frequency domain by means of Wiener-Khintchine theorem. The definition of RIN is the autocorrelation integral of optical power fluctuations divided by total power squared and can be expressed as total RIN [33].

$$RIN_T = \frac{\langle \delta P(t) \rangle^2}{\langle P_{AVG}(t) \rangle^2} = \int_0^\infty R(\nu) d\nu \quad \text{unitless} \quad (2.13)$$

where  $P(t)$  is the optical power of the source,  $P_{AVG}(t)$  is the average power of the source,  $\langle \rangle^2$  stands for the mean squared,  $R(\nu)$  is the spectral density of the RIN, conventionally called RIN (unit: dB/Hz). In many lightwave transmission systems RIN is very important quantity that can be used to determine the maximum realizable signal-to-noise ratio (SNR) by the following relation.

$$SNR = \frac{m^2}{2B \cdot RIN} \quad (2.14)$$

where  $m$  is the optical modulation index,  $B$  is the noise bandwidth. As we can see from the relation lower RIN is always desirable to get better performance in applications. RIN of

semiconductor lasers decreases with increasing laser power due to the decrease of ASE coupled into the laser mode. RIN of typical devices are listed in the Table 3.

Table 3

Typical Devices RIN

Device	RIN
DFB Laser	-149.2 dB/Hz $\pm$ 0.02 dB/Hz
ASE in EDFA	-110 dB/Hz $\pm$ 0.15 dB/Hz

#### 2.4.2 Measurement and Calibration of RIN

In order to have adequate sensitivity of RIN measurement the amplifier gain must be large enough, and its noise figure low enough in relation to electrical spectrum analyzer (ESA) noise figure. To increase dynamic range it would be better to use high-gain-low-noise amplifier with a proper DC block. Figure 20 shows schematic diagram of RIN measurement setup and calibration. According to the measurement setup shown in Figure 20, the measured power spectral density of an optical source under test contains not only the laser power but also shot noise power as well as system thermal noise power. We must subtract the shot noise and the system noise from the measured power spectral density in order to get the RIN of the source. The details of calibration factors and procedures are described below [34]

- $P^* \text{ [dBm/Hz]} = P(\text{measured spectral density}) - 10 \cdot \log(1.2 \cdot \text{RBW}) + 2.5 - \text{System Gain}$
- $\text{RIN [dB/Hz]} = P^* - P(\text{shot}) - P(\text{system}) - \text{Carrier Power}$



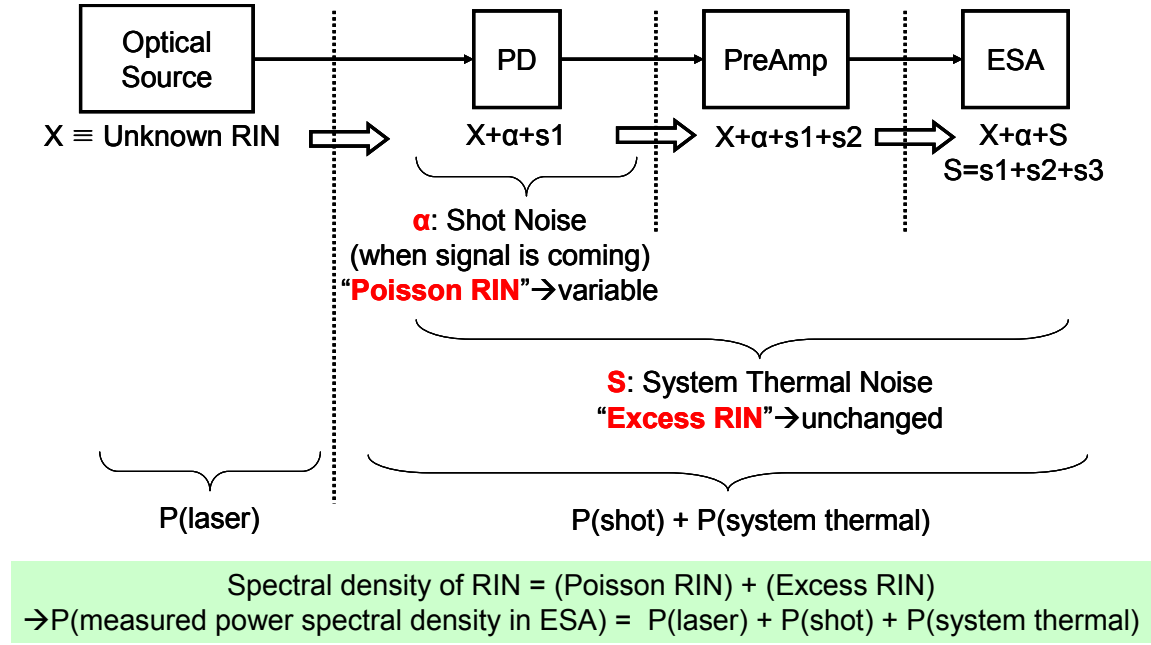


Figure 20: Schematic diagram of RIN measurement setup and calibration.

RBW is the resolution bandwidth of the ESA, and the factor 1.2 is for normalization to a 1HZ noise equivalent bandwidth [34]. The result is in dB. The factor 2.5 is the correction for log amplifiers and peak detectors used in an analog spectrum analyzer [34]. For the RIN measurement hp8566B analog ESA was used.

### 2.4.3 RIN Measurement of MSLs

Phase coherent optical frequency combs from mode-locked semiconductor lasers (MSLs) have been recently recognized as a very attractive optical source for secure coherent communication applications as well as various future photonic system applications [35,36]. In fact, one of the most important prerequisite issues for the practical use of optical combs from MSLs is how to obtain frequency-stable optical combs with low relative intensity noise (RIN).

Many authors have reported RIN measurements and some feasible approaches to reduce RIN of MSL [22,23]. However, to our knowledge, there has been no study reported on RIN reduction of frequency stabilized optical combs of MSLs. In this section, we report the first measurement, to our knowledge, of the general RIN characteristics as well as RIN reduction in a frequency stabilized grating-coupled MSL showing the relationship between RIN and mode coherency of the MSL. Figure 21 shows the schematic diagram of the general RIN and modal RIN measurement.

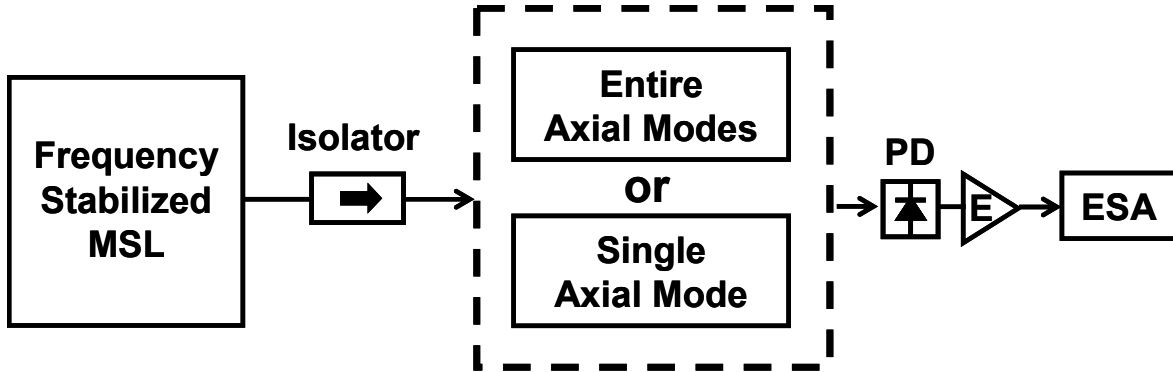


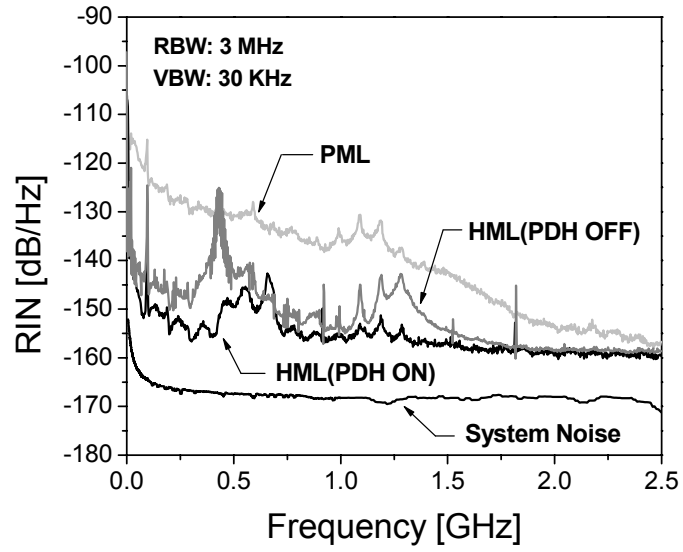
Figure 21: Schematic diagram of the general RIN and modal RIN measurement

In this experiment, an external cavity grating-coupled MSL system is configured to generate optical frequency combs of a fundamental cavity frequency of 6.33 GHz as shown in Figure 21. The laser cavity consists of an electroabsorption (EA) modulator incorporated two-section semiconductor optical amplifier (SOA), an aspheric collimating lens, an optical sampler, and a grating with a groove density of 600 lines/mm. The laser is initially passively mode-locked by applying 78 mA DC current and -2.8 V DC voltage on the gain and EA modulator section in

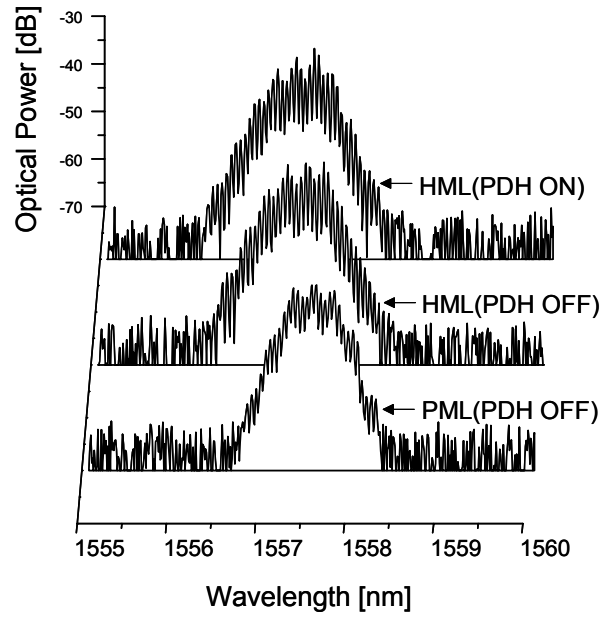
the monolithic two-section device, respectively. By applying an additional 6.33 GHz RF signal on the modulator section phase coherent periodic axial modes, defined by the optical cavity and RF modulation, are produced. However, the axial modes wander in frequency due to effective cavity length variations from environmental perturbations, which result in power fluctuation due to gain-index coupling mechanism. In the frequency domain, laser RIN can be conveniently described by the power spectral density function of the laser output power fluctuation. In this experiment, RIN of either the entire axial mode set (general RIN) or a filtered single axial mode (modal RIN) is recorded using an electrical spectrum analyzer (HP8566B) through a 15 GHz bandwidth photodetector and a low-noise-high-gain electrical amplifier as shown in Figure 21.

#### **2.4.4 General RIN Characteristics of a Frequency Stabilized Grating-Coupled MSL**

The RIN of the collective intensity fluctuation of the entire axial mode set from the laser system is measured in both passive and hybrid mode-locked operations depending on the situation with (PDH ON) and without (PDH OFF) frequency stabilization, as shown in Figure 22 (a). The RIN of hybrid mode-locked (HML) operation is measured to be more than 15 dB lower than the RIN from passive mode-locked (PML) operation in the frequency range below 1 GHz. This result agrees well with the previous studies on the suppression of mode partition noise in a hybrid MSL [22]. The corresponding optical spectra are shown in Figure 22 (b) Higher mode contrast is obtained from the HML operation with lower RIN level in comparison with the PML operation. Results of the different mode-locked condition show an interesting feature that the total RIN, the area under the curve shown in Figure 22 (a) is always lower when the contrast of the laser axial modes is larger. Lowest RIN was obtained from the HML operation with



(a)



(b)

Figure 22: General RIN measurement: (a) RIN of the entire axial mode set of the MSL (b) corresponding optical spectra of the MSL

frequency stabilization. The average RIN level of the frequency stabilized HML operation was measured to be less than -150 dB/Hz throughout the frequency up to 2.5 GHz. In the HML operations, the RIN of the laser with frequency stabilization is measured to be as much as 10 dB lower than the RIN from the laser without frequency stabilization in the frequency range from 1 MHz to 500 MHz. It should be mentioned that the reason for the unnoticeable difference of optical mode contrasts between with and without frequency stabilization in the HML operation is due to the resolution limit (0.01nm) of the optical spectrum analyzer.

#### **2.4.5 Modal RIN Reduction of a Frequency Stabilized Grating-Coupled MSL**

In order to measure modal RIN of the MSL, a 16-channel hyperfine WDM filter with a grid space of 6.33 GHz and a channel crosstalk of around 15dB was used to separate a single axial mode from the MSL in the HML operation. The experimental and theoretical results of the modal RIN are shown in Figure 23. A modal RIN reduction of approximately 3 dB was obtained by frequency stabilization throughout the frequency range from 1 MHz to 500 MHz shown in Figure 23 (a).

#### **Mode Coherence Effect**

One of the feasible explanations for the RIN reduction from the frequency stabilized MSL can be made by the theory of a mode-locked laser describing the mode coherence of the laser [37,38]. The laser output field  $E$  with the amplitude fluctuation  $\Delta E$  and the phase fluctuation  $\Delta\phi$  can be given by

$$\varepsilon(t) \equiv \sum_n (E_n + \Delta E_n) \cdot \exp(-i\nu_n t - i\Delta\phi_n) \quad (2.15)$$

where  $n$  is the mode index of the laser output,  $\nu_n$  is the carrier frequency of laser mode  $n$ . Then the field coherence function  $\gamma(\tau)$  can be defined as [37]

$$\gamma(\tau) \equiv \frac{\langle \varepsilon^*(t) \varepsilon(t + \tau) \rangle}{\langle |\varepsilon|^2 \rangle} = \exp\left(-\frac{|\tau|}{\tau_c}\right) \cdot \exp(-i\nu_0 \tau) \cdot \sum_m \exp\left(-\frac{\nu_M^2 N^2}{8} \cdot (\tau - mT_R)^2\right) \quad (2.16)$$

where the  $\langle \varepsilon^*(t) \varepsilon(t + \tau) \rangle$  is field correlation function, the  $\tau_c$  is coherence time of the laser mode, the  $N$  is number of locked modes, the  $\nu_0$  is central mode frequency, the  $\nu_M$  modulation frequency, the cavity roundtrip time  $T_R \equiv 2\pi/(\nu_n - \nu_{n-1})$ . The laser power spectrum can be calculated by the Fourier transform of the field coherence function  $\gamma(\tau)$ . As a result, each mode of the laser has the same linewidth  $1/\tau_c$  and the field coherence function implicitly represents a degree of mode coherence of the mode-locked laser. The amplitude fluctuation in one mode of the MSL is given by [37]

$$\langle \Delta E_n(t) \Delta E_n(t + \tau) \rangle = K \cdot \left\{ \frac{\exp(-\Gamma_0 |\tau|)}{2\Gamma_0} + \sum_{p=1}^{\infty} \left[ \text{Her}^2\left(p, \frac{\sqrt{2}n}{N}\right) \cdot \frac{1}{2^p p!} \cdot \frac{N}{\pi} \cdot \frac{\exp(-p\gamma|\tau|)}{2p\gamma} \right] \right\} \quad (2.17)$$

where the  $K$  is proportional constant, the  $\Gamma_0$  is spectral width of the laser,  $\text{Her}\left(p, \frac{\sqrt{2}n}{N}\right)$  is the

$p$  th Hermite polynomial for the mode  $n$ . The RIN of the central mode of the MSL can be given as the following expression, taking the Fourier transform of equation (2.17),

$$RIN_{\text{mod}}(f) = C \cdot \left\{ \frac{1}{1+f^2} + \sum_{p=0}^N \left[ Her^2(p,0) \cdot \frac{1}{2^p \cdot p!} \cdot \frac{N}{\pi} \cdot \frac{1}{(p \cdot r)^2 + f^2} \right] \right\} \quad (2.18)$$

where the  $r$  is mode coupling coefficient, defined as  $r \equiv \frac{|\gamma(\tau)|}{\Gamma_0}$ , the  $C$  is amplitude normalization constant,  $Her(p,0)$  is the  $p$ th Hermite polynomial for the central mode and the  $f$  is normalized frequency with respect to the spectral width of the laser.

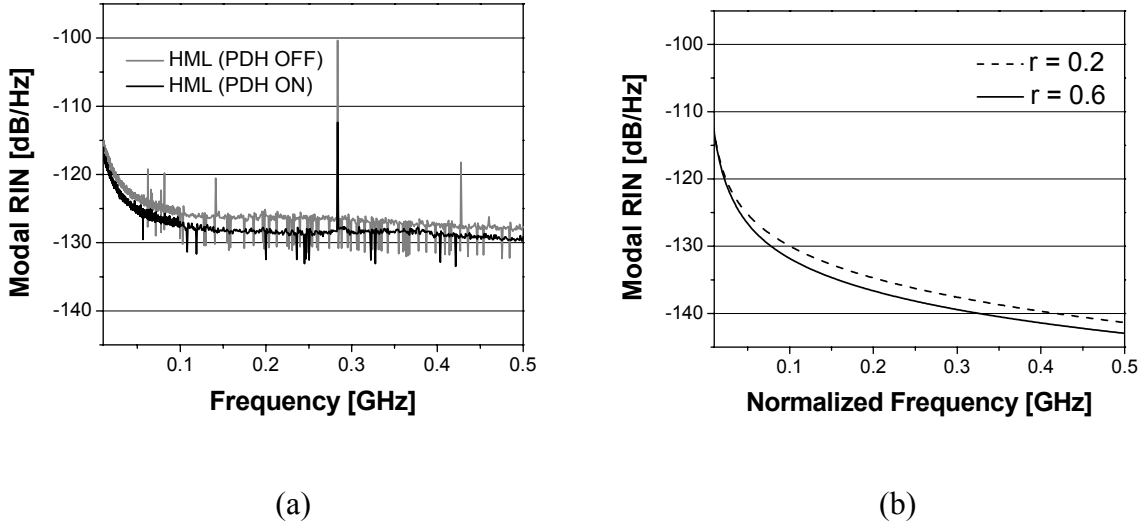


Figure 23: Modal RIN measurement (a) RIN measurements of a filtered single axial mode of the MSL with and without PDH frequency stabilization (b) theoretically calculated modal RIN (N=30)

According to this theory, the larger optical mode contrast corresponds to strong phase coherence of the mode-locked laser. The theoretically calculated modal RIN is shown in Figure 23 (b). The mode coupling coefficient  $r$  represents degree of mode coherence of the mode-locked laser [37, 38]. As the mode coupling increases, modal RIN decreases in the low frequency range. The calculated modal RIN shows a good agreement with the experimental results.

### **FM-AM Noise Conversion Effect**

Filtering out a single axial mode may introduce the FM-AM noise conversion due to the filter shape. The main noise source is believed to be environmental effects which cause a frequency drift with respect to the center frequency of the filter window. Since the intensity fluctuation caused by a slow frequency drifting below 1 MHz was not recorded in our RIN measurements due to a limited frequency response of the measurement system, which is 1 MHz to 15 GHz. In addition, the excess intensity fluctuation due to a fast frequency drifting (up to 2.5 GHz) can be estimated by considering the intensity noise due to the FM-AM noise conversion within the locking bandwidth (320 MHz) of the laser frequency stabilization. The FM-AM coupled intensity fluctuation was estimated to be less than 0.7 % based on the measured filter shape function shown in appendix D. The noise power level corresponding to the 0.7 % intensity fluctuation can be calculated by the following relation,

$$P_A = 10 \cdot \log \left[ \left( \frac{\Delta A}{A} \right)^2 \cdot \frac{1}{B} \right] \quad (2.20)$$



where,  $B$  is the noise bandwidth,  $A$  is the amplitude(optical power) of the filtered axial mode. The power level due to a fast frequency drifting up to 2.5 GHz is well below -137 dB/Hz. Therefore, the contribution of FM-AM noise conversion is negligible in our modal RIN reduction.

*Conclusion:* In this study, experimental results of general RIN characteristics, as well as, RIN reduction in a frequency stabilized grating-coupled MSL using the PDH frequency stabilization technique based on injection current control were described. Average RIN level of less than -150 dB/Hz, as well as, in the frequency range 1 MHz to 500 MHz, general RIN reduction of 10 dB and modal RIN reduction of 3 dB were obtained from the frequency stabilized hybrid MSL. In this frequency stabilized MSL system, the active control of the injection current to the gain medium in the laser cavity produces a mechanism, the gain-index coupling, to improve the inter-modal coherence between the axial modes.

#### **2.4.6 Comparison of RIN of a Mirror Coupled and a Grating Coupled MSLs**

The relative intensity noise (RIN), collective intensity fluctuation of the entire axial mode set from the previously shown the mirror-coupled MSL systems with a fundamental frequency of 33 GHz was measured in both passively and hybridly mode-locked operations. The RIN measurements of the mirror-coupled MSL systems are shown in Figure 24.

In both MSL systems, the hybridly mode-locked states reveals lower RIN than the passively mode-locked states due to the suppression of mode partition noise [22]. In the hybridly mode-locked operation, the grating coupled MSL showed a lower RIN level up to  $\sim 10$  dB than the mirror coupled MSL through a low frequency range below 500 MHz, whereas, in the

passively mode-locked operation the RIN level of the grating coupled laser is significantly larger than that of the mirror coupled laser through the entire frequency range up to 2 GHz.

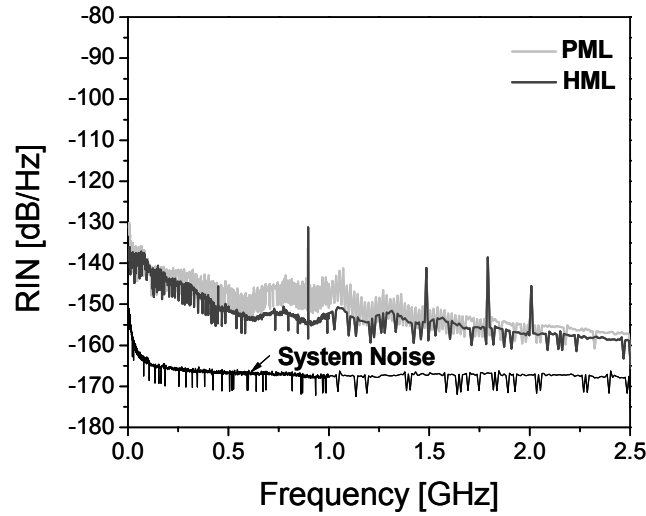


Figure 24: The RIN measurements of the mirror-coupled MSL systems

The grating-coupled MSL showed a large difference of the RIN level up to  $\sim 20$  dB depending on the operation conditions of modelocking. Nonetheless, lowest average RIN level was obtained from the grating-coupled MSL, and was measured to be  $\sim -150$  dB/Hz throughout the frequency range from 1 MHz to 2.5 GHz.

## CHAPTER 3: SYNCHRONIZED MSL SYSTEMS

### 3.1 Introduction

The phase coherent broad-band spectral combs from a modelocked semiconductor laser (MSL) are very attractive and flexibly applicable optical carriers to many coherent communication systems and optical analog and digital signal processing owing to the capability of accommodating large amounts of information, [3, 53] as well as, the ability of facilitating robust synchronization between independent MSL oscillators at distinct locations [8]. As compared with other techniques, optical injection locking is a very simple technique due to the lack of active feedback control for phase tracking of a stable reference oscillator, while providing fairly strong relative oscillator harmonization [9, 12]. This advantage can be ideally implemented in MSL systems owing to the initial phase coherence in spectral combs. Recent, extensive works on optical injection locking have shown on admirably stable quality of oscillator synchronization in a wide range of applications such as coherent detection [13, 54], dense optical frequency multiplexing [10], and low noise millimeter-wave carrier generation for radio-on-fiber systems in wireless access networks [11, 14].

#### 3.1.1 Theory of Injection Locking

Based on the semiclassical laser theory, the complex electric field of the cavity longitudinal mode in the slave laser cavity can be expressed as  $\bar{E} = E(t)e^{j(\omega t + \phi(t))}$ , where  $E(t)$  is the slowly varying amplitude,  $\omega$  is the optical frequency of the target cavity mode into which the external injection seed beam is injected, and  $\phi(t)$  is the phase of the cavity mode. In the presence

of an external coherent light injection, the complex electric field of the slave laser can be described by [9]

$$\frac{d\bar{E}}{dt} = \left[ j\omega + \frac{1}{2} \left( G(N) - \frac{1}{\tau_p} \right) \right] \bar{E} + \kappa \bar{E}_{inj} \quad (3.1)$$

where  $\tau_p$  is the photon lifetime,  $\kappa$  is the coupling coefficient of injection efficiency,  $G(N)$  is the modal gain depending on carrier density  $N$ , and the external injection field is given by  $\bar{E}_{inj} = E_{inj}(t)e^{j(\omega_{inj}t + \phi_{inj}(t))}$ . In the Eq. (3.1), all the considerable noise terms are neglected for the following derivation. For convenience, we will convert Eq. (3.1) into the expressions described by real quantities. The electric field description can be expressed by photon number description through the following relation.

$$\frac{dS}{dt} = \frac{d}{dt}(\bar{E} \cdot \bar{E}^*) = 2 \operatorname{Re}(\bar{E}^* \cdot \frac{d\bar{E}}{dt}) \quad (3.2)$$

where the photon number is defined by  $S = |\bar{E}|^2$ . Under stable injection locking, the optical frequency of the slave laser  $\omega$  is equal to the optical frequency of the external injection field  $\omega_{inj}$ . From the Eqns. (3.1) and (3.2), we obtain the photon number rate equation

$$\frac{dS}{dt} = \left[ G(N) - \frac{1}{\tau_p} \right] S + 2\kappa \sqrt{S \cdot S_{inj}} \cdot \cos(\Delta\phi) \quad (3.3)$$

where  $\Delta\phi = \phi_{inj}(t) - \phi(t)$ . Now, we will continue derivation for the phase equation by extracting out the slowly varying terms from the complex electric field of the cavity longitudinal mode in the slave laser cavity, which can be defined by

$$\tilde{E} = \sqrt{S} \cdot e^{i\phi(t)} \quad (3.4)$$

Taking a time derivative of this Eq.(3.4) and multiplying both sides by a conjugate electric field  $\tilde{E}^*(t)$ , then we have

$$\frac{d\phi}{dt} = \frac{1}{S} \text{Im} \left\{ \tilde{E}^* \cdot \frac{d\tilde{E}}{dt} \right\} \quad (3.5)$$

Considering stably injection locked state, the optical frequency of the slave laser can be specified by the optical frequency of the external injection field and the slowly varying term can be expressed by

$$\tilde{E} = \bar{E} \cdot e^{-j\omega_{inj}t} \quad (3.6)$$

Inserting Eq.(3.6) into (3.5) we obtain the phase equation

$$\frac{d\phi}{dt} = \omega - \omega_{inj} + \kappa \sqrt{\frac{S_{inj}}{S}} \sin(\Delta\phi) \quad (3.7)$$

An external light injection into a slave laser introduces the relative carrier density change, which results in an optical frequency shift. The optical frequency of the target mode in the slave laser can be expanded as

$$\omega(N) = \omega(N_{th}) + \frac{1}{2} \alpha \cdot G_N \cdot (N - N_{th}) \quad (3.8)$$

where  $N_{th}$  is the clamped carrier density without any light injection into the slave laser,  $\alpha$  is the linewidth enhancement factor which is defined as the ratio of the partial derivatives of the real and complex parts of the complex susceptibility with respect to carrier density  $N$ , and  $G_N$  is the differential gain. Inserting Eq. (3.8) into (3.7), we obtain

$$\frac{d\phi}{dt} = (\omega(N_{th}) - \omega_{inj}) + \frac{\alpha}{2} \cdot G_N \cdot (N - N_{th}) + \kappa \sqrt{\frac{S_{inj}}{S}} \sin(\Delta\phi) \quad (3.9)$$

Considering gain saturation and gain compression factor, total gain  $g(N)$  of the slave laser can be given by [39]

$$g(N) = \frac{G_N \cdot (N - N_{th})}{1 + \epsilon S} \quad (3.10)$$

where  $\epsilon$  is the gain compression factor. From the Eqns. (3.3) and (3.9) combining with carrier density rate equation, a set of rate equations which describes injection locked slave laser are expressed as following

$$\frac{dS}{dt} = \left[ g(N) - \frac{1}{\tau_p} \right] S + 2\kappa \sqrt{S \cdot S_{inj}} \cdot \cos(\Delta\phi) \quad (3.11)$$

$$\frac{d\phi}{dt} = (\omega(N_{th}) - \omega_{inj}) + \frac{\alpha}{2} \cdot G_N \cdot (N - N_{th}) + \kappa \sqrt{\frac{S_{inj}}{S}} \sin(\Delta\phi) \quad (3.12)$$

$$\frac{dN}{dt} = J - \frac{N}{\tau_{spont}} - g(N) \cdot S \quad (3.13)$$

In the presence of external injection, the optical power of the target cavity mode in the slave laser is coupled with the phase of the cavity mode depending on the carrier density of the laser system. The photon-phase coupling strength is proportional to the square root of the power ratio between the slave laser and injection beam. Depending on the relative injection power and phase difference, the characteristics of the injection locking can be simply explained. We will discuss conditions for stable injection locking as well as the locking range in the following section.

### 3.1.2 Locking Range

Considering steady state of injection locking, we can set the time derivatives in left hand side of the previous Equations (3.11) and (3.12) to be zero, as following

$$0 = \left[ g(N) - \frac{1}{\tau_p} \right] S + 2\kappa \sqrt{S \cdot S_{inj}} \cdot \cos(\Delta\phi) \quad (3.14)$$

$$0 = (\omega(N_{th}) - \omega_{inj}) + \frac{\alpha}{2} \cdot G_N \cdot (N - N_{th}) + \kappa \sqrt{\frac{S_{inj}}{S}} \sin(\Delta\phi) \quad (3.15)$$

We can simplify the gain tem in Eq. (3.14) as following approximation

$$\left[ g(N) - \frac{1}{\tau_p} \right] \approx G_N \cdot (N - N_{th})$$

Then from Equation (3.14)

$$G_N \cdot (N - N_{th}) \approx -2\kappa \sqrt{\frac{S_{inj}}{S}} \cdot \cos(\Delta\phi) \quad (3.16)$$

Substituting Eq.(3.16) into (3.15), we obtain frequency detuning relation for the injection locked slave laser, as following

$$\begin{aligned} \Delta\omega &= \kappa \sqrt{\frac{S_{inj}}{S}} \cdot [\sin(\Delta\phi) - \alpha \cdot \cos(\Delta\phi)] \\ &= \kappa \sqrt{\frac{S_{inj}}{S}} \cdot \sqrt{1 + \alpha^2} \cdot \sin(\Delta\phi - \psi) \end{aligned} \quad (3.17)$$

where  $\Delta\omega = \omega_{inj} - \omega$  and  $\psi = \tan^{-1} \alpha$ . Equation (3.17) can be rewritten for  $\Delta\phi$ , as a function of frequency detuning and injection power ratio, and  $\alpha$ , we have

$$\Delta\phi = \sin^{-1} \left( \frac{\Delta\omega}{\kappa \sqrt{\frac{S_{inj}}{S}} \cdot \sqrt{1 + \alpha^2}} \right) + \tan^{-1} \alpha \quad (3.18)$$



Some important physical restriction can be found from Eq.(3.16) for stable locking condition. When the external injection field intrudes on the slave laser, the injection reduces the gain in the slave laser consuming some of the carriers. Therefore, the sign of the  $\cos(\Delta\phi)$  term in the Eq.(3.16) must be positive for the stable locking condition. In consequence the relative phase difference must be  $-\frac{\pi}{2} \leq \Delta\phi \leq \frac{\pi}{2}$ , which leads to a locking range, given by:

$$-\kappa \sqrt{\frac{S_{inj}}{S}} \cdot \sqrt{1 + \alpha^2} \leq \Delta\omega \leq \kappa \sqrt{\frac{S_{inj}}{S}} \quad (3.19)$$

The plot of injection locking range depending on  $\alpha$  is shown in Figure 25. Considering effective transmission and mode matching [9], the coupling coefficient  $\kappa$  can be defined by

$$\kappa = \Delta\nu \cdot \frac{1 - R}{\sqrt{R}} \quad (3.20)$$

where the  $\Delta\nu$  is the cavity frequency and  $R$  is the effective reflectivity of the output coupler window of the slave laser. Physics of the asymmetric locking range is based on the Kramers-Kronig relationship between the carrier density and the refractive index of gain medium in the slave laser system. With an external injection, the decrease in the carrier density in the slave laser cavity causes cavity length to be effectively longer so that the cavity wavelength shifts in the direction of longer wavelength side. This hints that relatively easier injection locking can be obtained by injecting an injection field into red side of the target cavity mode. Furthermore, it is

very useful to measure the locking range within a stable locking condition because the  $\alpha$  factor can be properly estimated through the Eq.(3.19). Figure 25 shows the calculated locking range depending on injection power ratio considering our injection locking systems which has a cavity

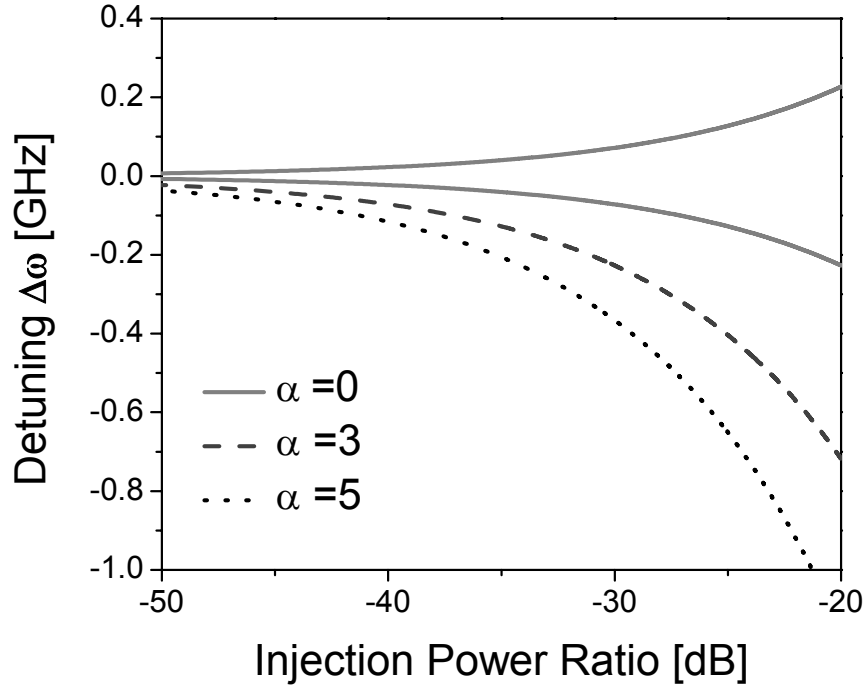


Figure 25: Injection locking range depending on  $\alpha$

frequency of 6.33 GHz and a coupler reflectivity of 70 %. At an injection power ratio of -30 dB, a maximum half locking bandwidth goes 70 MHz ( $\alpha = 0$ ), 200 MHz ( $\alpha = 3$ ), and 350 MHz ( $\alpha = 5$ ). It is rather ambiguous to define stable locking regime strictly. In our experiment, we defined stable locking conditions in terms of the sideband noise suppression of an injection-locked slave laser carrier at a certain offset frequency.

## 3.2 Experimental Demonstration of Injection Locking Techniques

### 3.2.1 Modulation Sideband Injection Locking of a MSL with a Tunable CW Laser

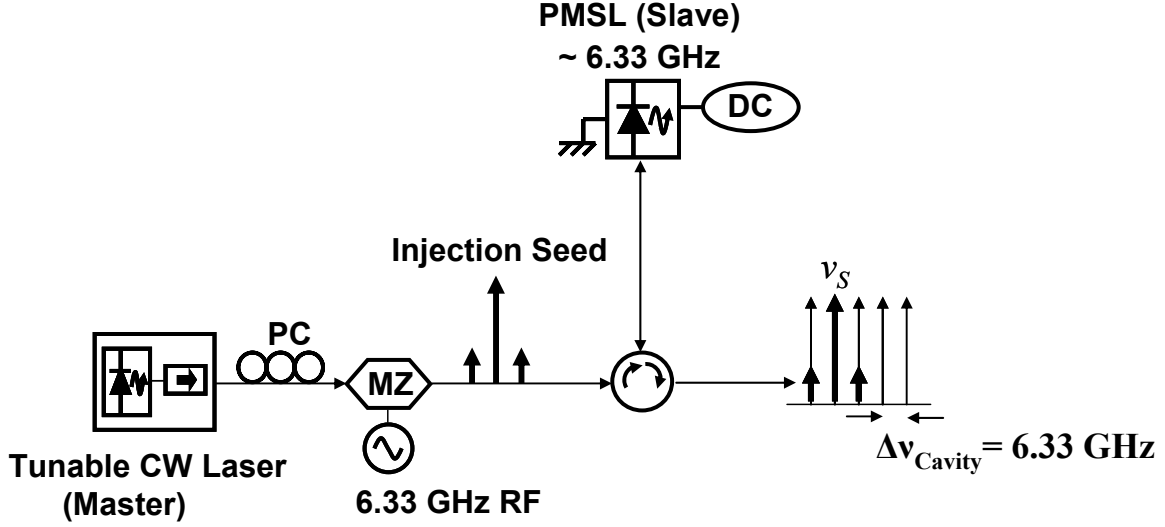


Figure 26: Schematic of experimental setup for the modulation sideband injection locking of a MSL with a tunable CW laser.

The tunable CW laser is simultaneously used as a data beam and as an injection seed to a passively modelocked laser that will serve as the comb source for LOs as shown in Figure 26. In the lower arm of the interferometer setup, two sinusoidal signals at 500 MHz and 700 MHz are applied to the first MZ to simulate two-tone amplitude modulated (AM) data signals. In the upper arm, the second MZ is modulated at 6.33GHz to impose sidebands that match the axial mode spacing of the modelocked laser LO. This seed beam is injected into a passively modelocked semiconductor laser based on a two-section semiconductor optical amplifier (SOA).

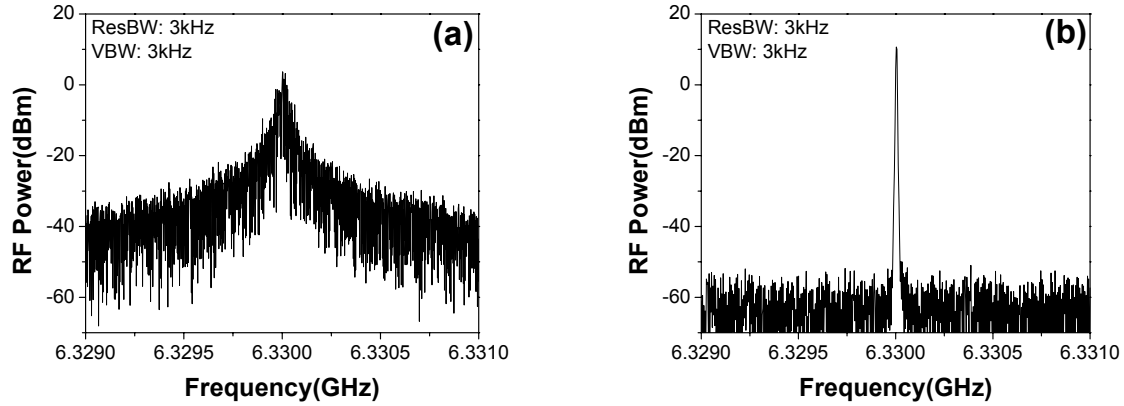


Figure 27: RF spectrum of the 6.33 GHz passively modelocked semiconductor laser LO (a) before injection locking and (b) after injection locking.

A hyperfine (HF) wavelength filter selects a single modelocked laser axial mode which is subsequently combined with the two-tone data signal. The combined signals prior to and subsequent to injection seeding are recorded in a RF spectrum analyzer. Finally, a microwave bandpass filter (BPF) is used to filter an information-bearing single channel.

Owing to inherent uncertainty in the phase of the laser source and effective cavity length variation, significant noise sidebands were observed with passive modelocking. The RF spectrum of the independent 6.33 GHz passively mode-locked semiconductor laser LO is shown in Figure 27(a). However, when the injection locking was implemented by using a CW injection seed with incoming average optical power of less than -20 dBm, the noise sidebands from the LO carrier were suppressed by 42 dB at 100 kHz offset in Figure 27(b).

### 3.2.2 Dual-Mode Injection Locking of Two Independent MSLs

A pair of neighboring axial modes out of the entire spectral band of an MSL system can be an ideal injection seed for another MSL system, simultaneously obtaining identical optical

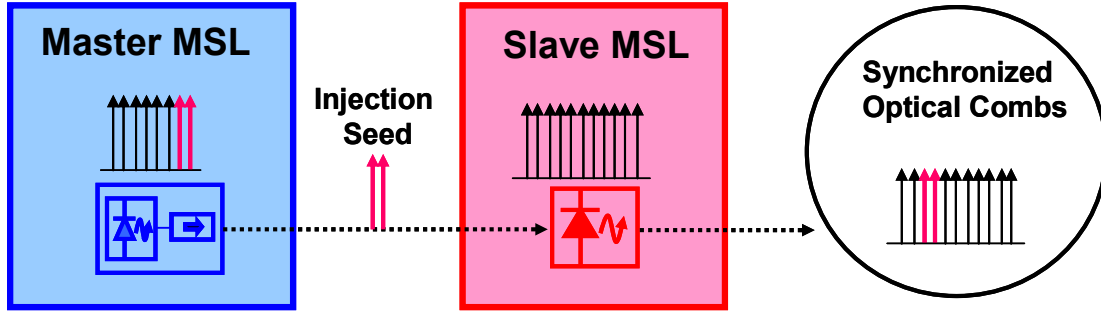
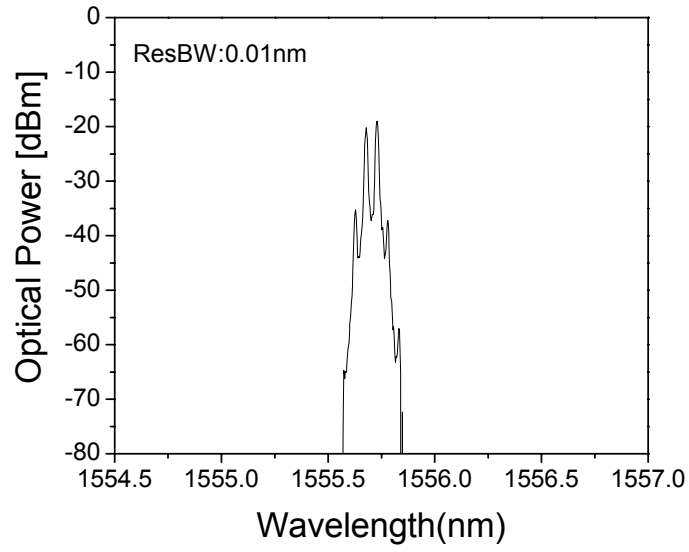
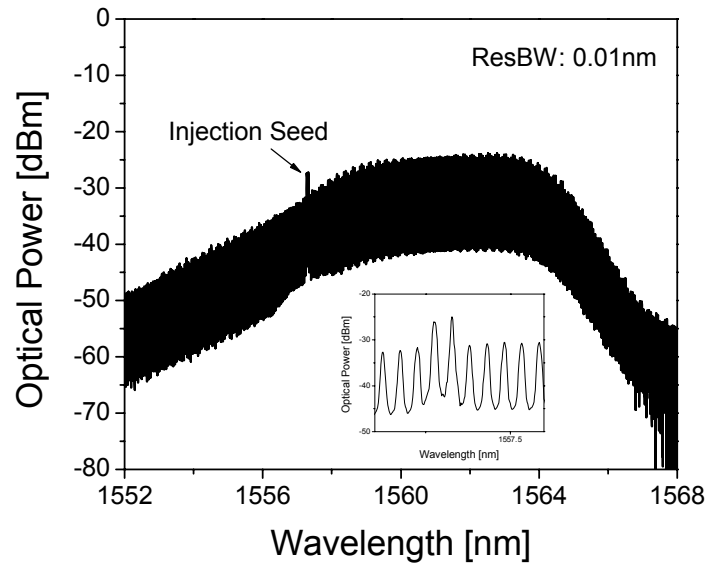


Figure 28: Conceptual diagram of the dual-mode injection locking of MSLs

frequency and phase synchronization, as well as, mode spacing between the two systems [40]. Because of the intrinsic characteristic of modelocking, the dual-mode injection seed has very strong phase coherency of the optical carriers as well as complete information of the laser system. This is necessary for achieving efficient remote harmonization between independent MSL systems, such as the laser cavity frequency, the optical carrier frequency and phase, and the noise characteristic of the carriers. The effect of this method is similar to an externally modulated CW injection technique [10,12]. However, our method ultimately requires much less optical power consumption and it is much simpler. Figure 28 and 29 show the conceptual diagram of the dual-mode injection locking of MSLs and the experimentally measured optical spectra of the dual-mode injection seed from a master MSL as well as an injection locked slave MSL as an example of the dual-mode injection locking.

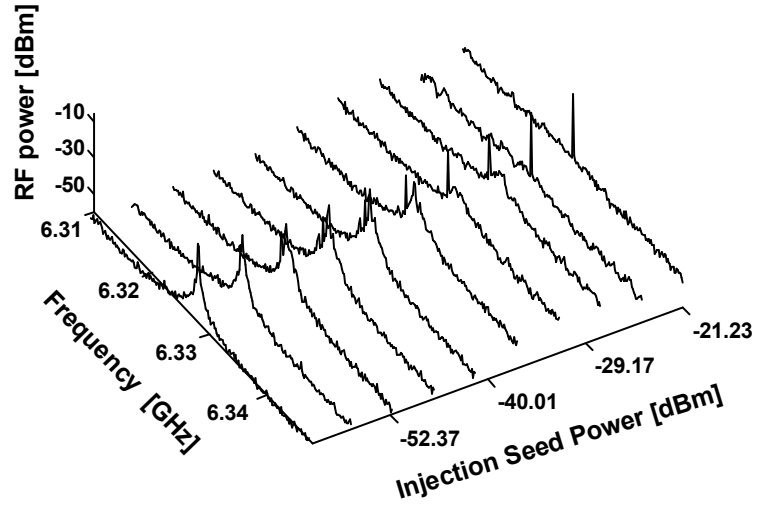


(a)

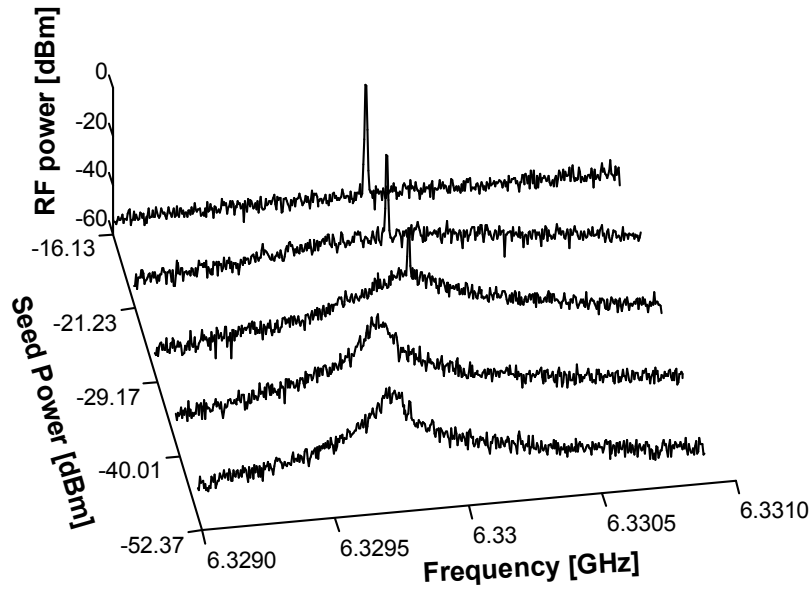


(b)

Figure 29: Experimentally measured optical spectra of the dual-mode injection seed from a master MSL (a) as well as an injection locked slave MSL(b).



(a)



(b)

Figure 30: Dynamic locking and pulling behavior of the injection seeded SL carrier. (a) dynamic evolution of the injection seeded SL carrier of injection locking (b) dynamic evolution of the cavity frequency detuned SL carrier of frequency pulling.

Figure 30(a) shows the measured dynamic locking behavior of the dual-mode injection seeded SL carrier at 6.33 GHz, increasing the seed power level from -60 to -20 dBm,. At the seed power level of -29.17 dBm, the noise sidebands of the SL carrier were suppressed by more than 35 dB at 100 kHz offset. In terms of seed power, a threshold behavior occurred with average optical seed power of less than -30 dBm and the stable locked state was shown after -29.17 dBm. The frequency pulling effect was observed from the injection locking of the initially cavity frequency detuned SL carrier. Depending on a given frequency offset range, the threshold level of the stable locking condition was slightly higher than the carrier frequency matched case. A locking bandwidth of 3 MHz, showing the carrier phase noise suppression of more than 30 dB at 100 kHz offset, was observed at the seed power -21.23 dBm. The dynamic evolution of the pulling effect is shown in Figure 30(b).

A novel optical injection locking method, dual-mode injection locking is ideal for obtaining synchronous optical frequency combs and optical pulses from MSLs. Further study on the utilization of the synchronized MSL systems will be discussed in the following chapter.



## CHAPTER 4: APPLICATIONS WITH SYNCHRONIZED MSLS

### 4.1 Coherent Analog Photonic Links

Coherent heterodyne detection has been widely studied in many coherent communication applications as well as various microwave photonic systems owing to the significantly improved signal-to-noise ratio and narrow channelization of broad-band signals as compared to common direct detection methods [41]-[44].

#### 4.1.1 Heterodyne Detection

In this experiment, the optical heterodyne detection for extremely densely channelized communication systems is demonstrated by an optical modulation sideband injection locking technique. A passively MSL injection locked to a tunable CW master laser forms a comb of broadband frequency probes, and a single axial mode is used as a local oscillator.

*Experiment and Results:* The tunable CW laser is simultaneously used as a data beam and as an injection seed to a passively modelocked laser that will serve as the comb source for LOs as shown in Figure 31. In the lower arm of the interferometer setup, two sinusoidal signals at 500 MHz and 700 MHz are applied to the first MZ to simulate two-tone amplitude modulated (AM) data signals shown in Figure 32. In the upper arm, the second MZ is modulated at 6.33GHz to impose sidebands that match the axial mode spacing of the modelocked laser LO. This seed beam is injected into a passively modelocked semiconductor laser based on a two-section semiconductor optical amplifier (SOA). A hyperfine (HF) wavelength filter selects a

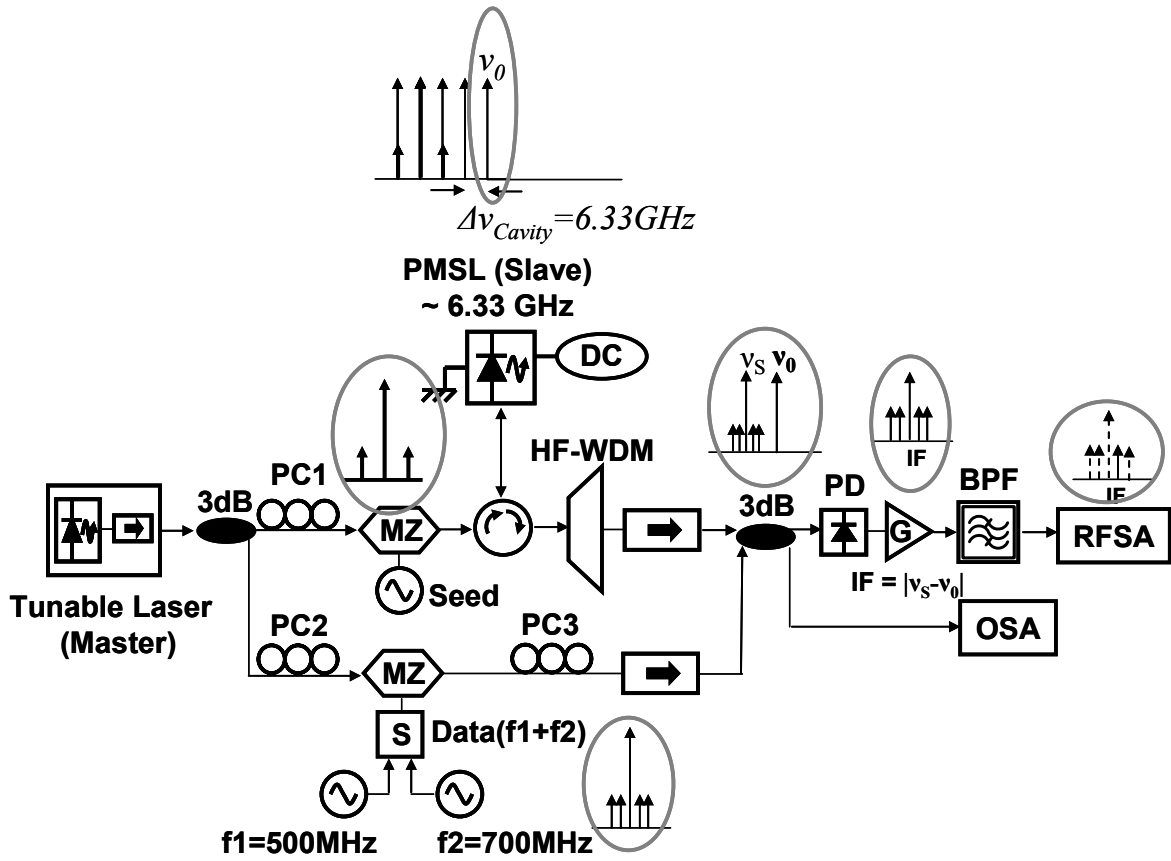
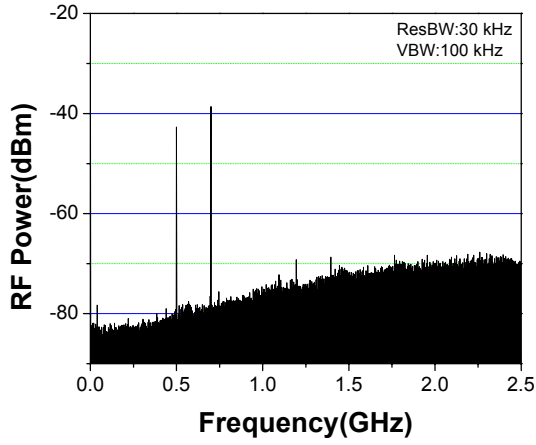
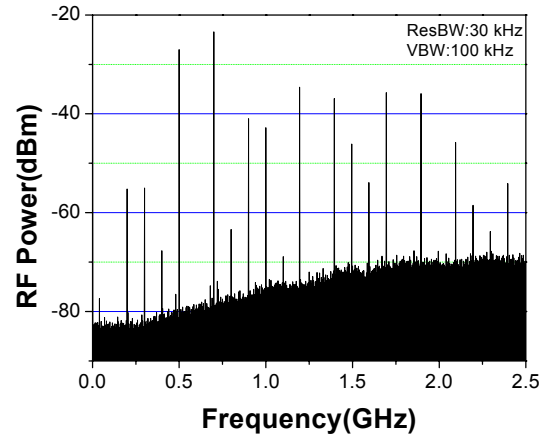


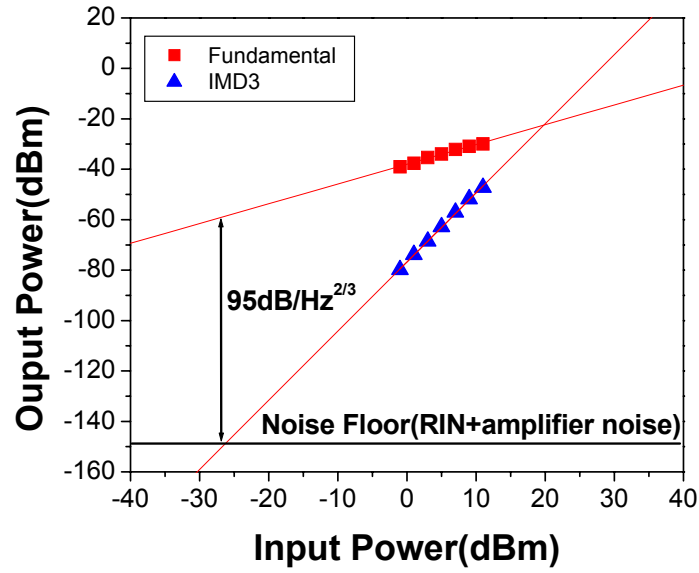
Figure 31: Schematic of the experimental setup for optical heterodyne detection based on modulation sideband injection locking. PML LD – passively modelocked laser diode; HF-WDM– hyperfine WDM filter; MZ – Mach-Zehnder intensity modulator; PD – photodiode; RFSA – radio frequency spectrum analyzer; OSA – optical spectrum analyzer; others defined in text.  $f_1 = 500\text{MHz}$ ;  $f_2 = 700\text{MHz}$



(a)



(b)



(c)

Figure 32: Modulated optical two-tone analog signals ( $f_1 = 500$  MHz;  $f_2 = 700$  MHz) (a) at optimum RF input power (b) at high RF input power (c) IMD measurement of the analog two-tone signals.

single axial mode which is subsequently combined with the two-tone data signal. The combined signals prior to and subsequent to injection seeding are recorded in a RF spectrum analyzer. Finally, a microwave bandpass filter (BPF) is used to filter an information-bearing single channel.

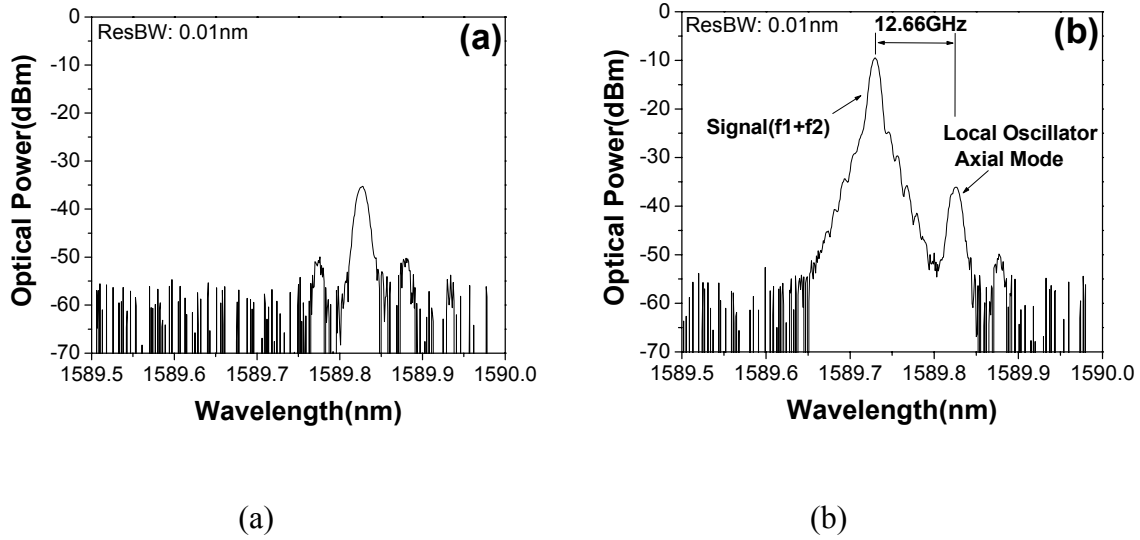


Figure 33: A filtered single axial mode of the 6.33 GHz passively modelocked semiconductor laser LO (a) and the optical spectrum of the analog signals ( $f_1 = 500$  MHz,  $f_2 = 700$  MHz) heterodyned with the selected single axial mode of the LO (b).

A modelocked laser axial mode detuned from the optical carrier frequency of the simulated RF data by two axial mode intervals combines with the simulated data to form a heterodyne beat signal at the IF of 12.66 GHz. Figure 33 (a) displays the optical spectrum of the filtered single axial mode of the 6.33 GHz passively modelocked semiconductor laser LO. The optical spectrum of heterodyne mixing the data signals and the selected single axial mode from

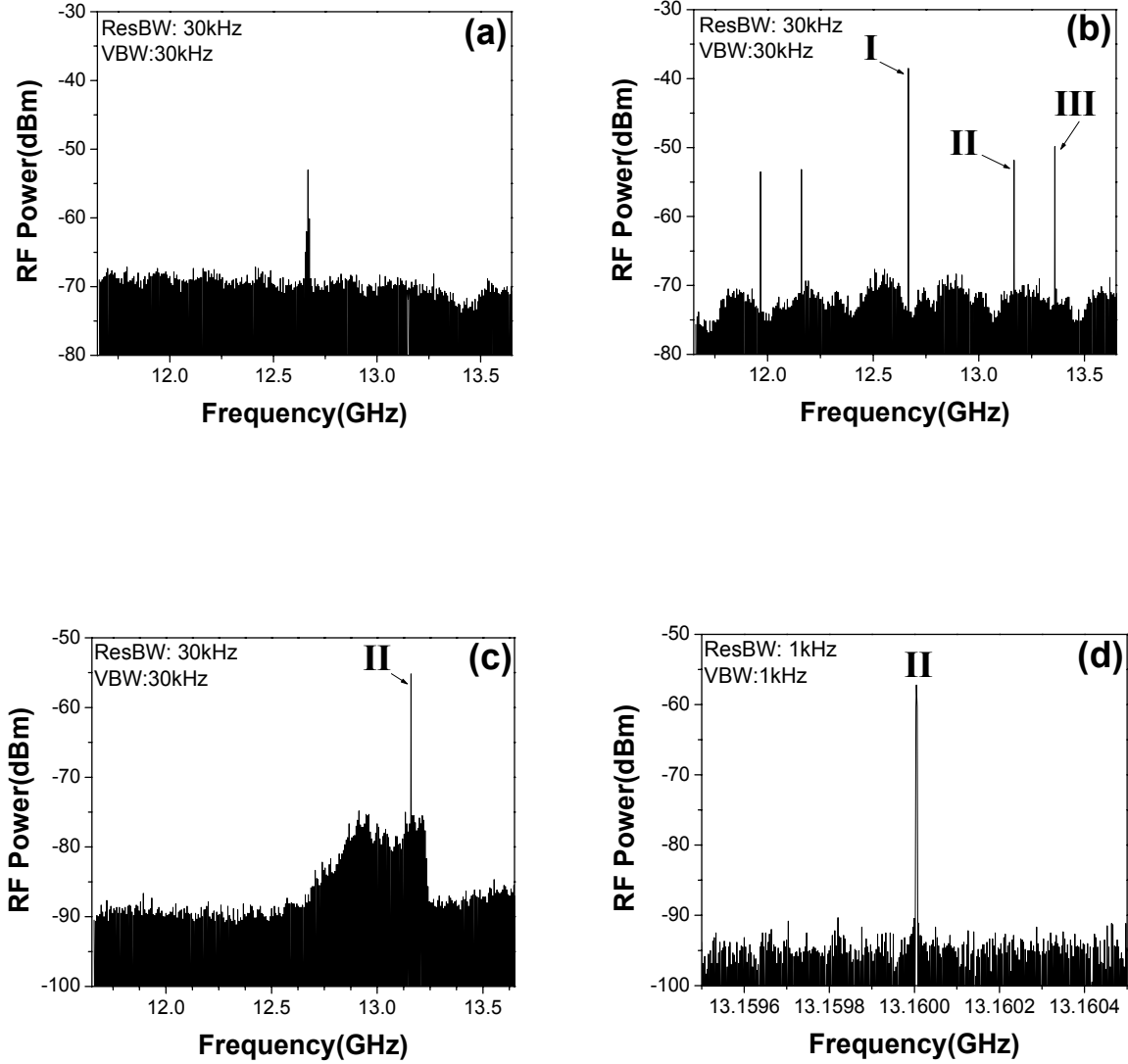


Figure 34: Heterodyne beat signal (a) before injection locking, (b) after injection locking (I: IF 12.66 GHz tone, II: 13.16 GHz tone [ IF+500 MHz ], III: 13.36 GHz tone [ IF+700 MHz ] ), (c) the microwave bandpass filtered 13.16 GHz tone at the resolution bandwidth of 30 kHz, and (d) a higher resolution scan of the 13.16 GHz tone (RBW = 1kHz).

the LO is shown in Figure 33 (b). The heterodyne signal prior to injection seeding lacks any trace of the data signals in Figure 34 (a). In contrast, the data signals were recovered when injection locking was implemented in Figure 34 (b). A microwave bandpass filter was used to demultiplex a single channel [Figure 34 (c)], [Figure 34 (d), high resolution scan]. One of two analog RF signals detuned by only 200 MHz showed a signal-to-noise ratio of over 65 dB/Hz through demultiplexing with a commercially available microwave bandpass filter. The single sideband noise of the heterodyne beat tone at 13.160 GHz was measured to be -123 dBc/Hz at 100 kHz offset from the carrier under injection locked state.

*Conclusion:* These experimental results verify that a single axial mode from a passively modelocked semiconductor laser injection locked to a MO serves admirably as a LO frequency probe despite the broad axial mode linewidth. This immunity is facilitated by the fixed relative phase difference between the carrier frequency in the MO and the frequency comb in the LO. The experimental results revealed a phase noise suppression of 42 dB from the injection locked LO carrier at 100 kHz offset, and a signal-to-noise ratio of over 65 dB/Hz in the channel selected from the two analog RF signals separated by only 200 MHz. These results show that monolithically integrated optical heterodyne detectors based on optical injection locking techniques are appealing for deployment of coherent lightwave technology.

#### **4.1.2 Broadband Coherent Probe System**

The experimental setup for the dual-mode injection locking of two independent MSLs is shown in Figure 35. Through the experimental setup, dynamic locking behavior depending on

injection seed power was observed, and the quality of the synchronization was verified by the following heterodyne detection experiment using a two-tone analog signal. As shown in Fig. 9 two MSLs play the role of a source of data channels from a master laser (ML), and coherent local oscillator (LO) probes from a slave laser (SL). The ML is the frequency stabilized hybridly mode-locked grating-coupled MSL with a fundamental cavity rate of 6.33 GHz, subject to the

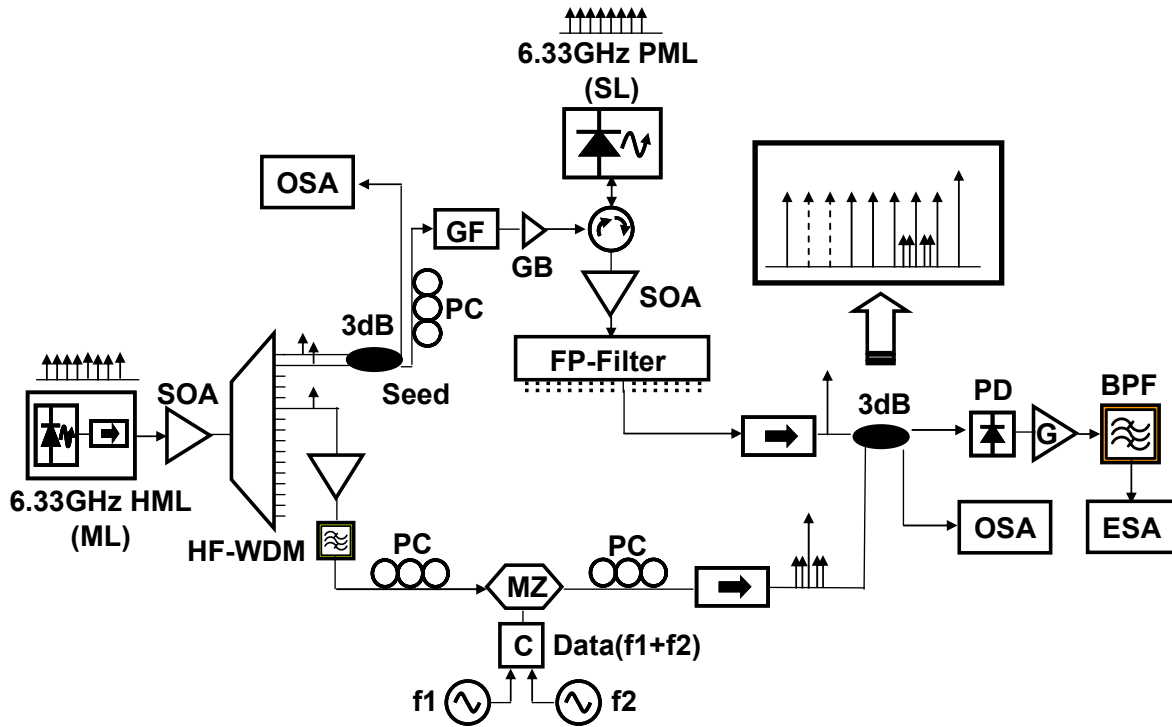


Figure 35: The experimental setup for the dual-mode injection locking of independent MSLs and heterodyne detection of a two-tone analog signal; GF: grating filter(See Appendix D); GB: optical gain block; PC: polarization controller; HF-WDM: hyperfine WDM filter; MZ: Mach-Zehnder intensity modulator; PD: photodiode; BPF: electrical bandpass filter; ESA – electrical spectrum analyzer; OSA – optical spectrum analyzer; others defined in text.

same rate of sinusoidal signal from a signal generator (Agilent E8254A) to form stable spectral combs for data channels. On the other hand, the SL is the passively mode-locked mirror coupled

MSL roughly with the same rate of the ML, and is susceptible to accept optical injection seed combs from the ML. The hyperfine (HF) wavelength filter with a grid space of 6.33 GHz is used to demultiplex 16 channels out of several tens of phase coherent spectral combs from the ML within a 3-dB bandwidth. Two of the channels are selected and combined in a 3 dB coupler, and

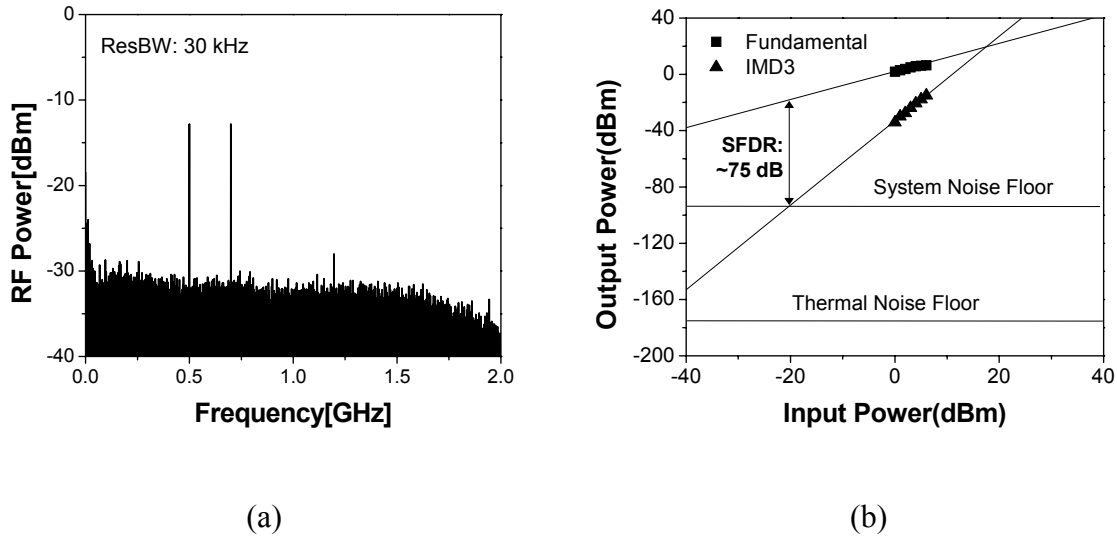
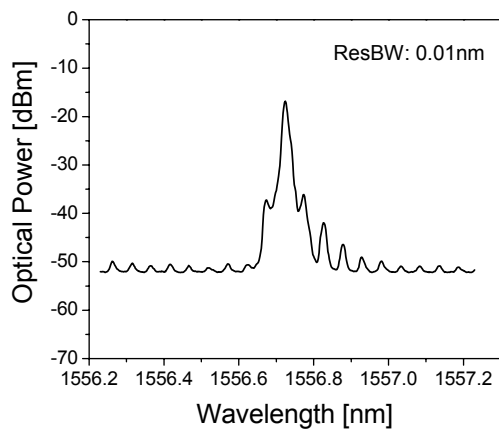


Figure 36: Two-tone analog signal. (a) sinusoidally modulated optical analog signals at 500 MHz and 700 MHz. (b) spurious free dynamic range (SFDR) measurement of the two-tone analog signal.

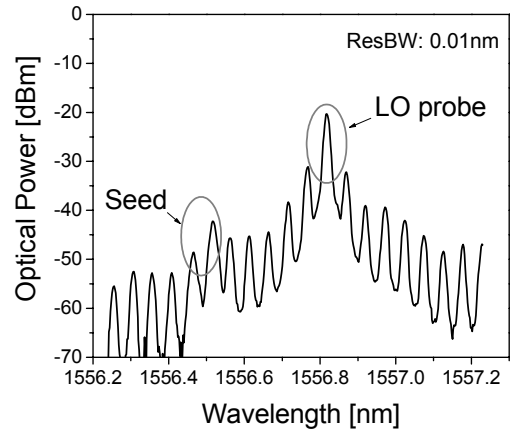
ultimately injected through a fiber optic circulator ( $> 60$  dB isolation) into the LO via the grating filter.

In order to verify the quality of oscillator synchronization, the previous injection locking experiment was extended into a heterodyne detection experiment of a two-tone analog signal. Another channel located at the four times of mode intervals apart from the closest seed channel is selected as an analog data channel, and imposed with two combined sinusoidally modulated signals at 500 MHz ( $f_1$ ) and 700 MHz ( $f_2$ ) by a Mach-Zehnder intensity modulator (MZI)

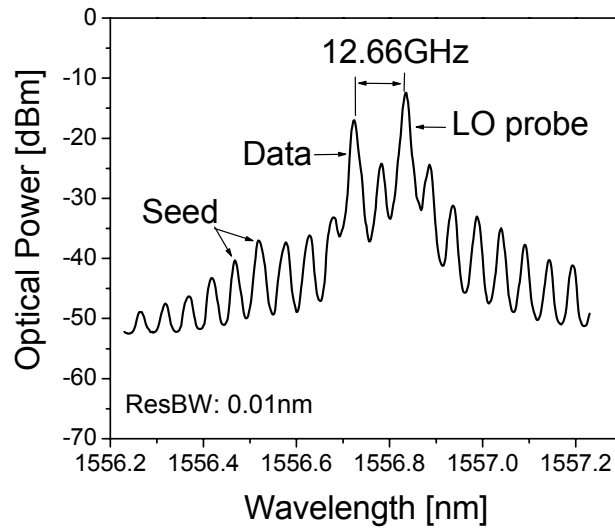




(a)

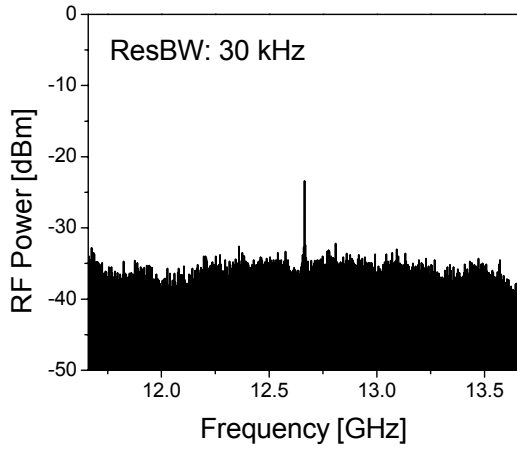


(b)

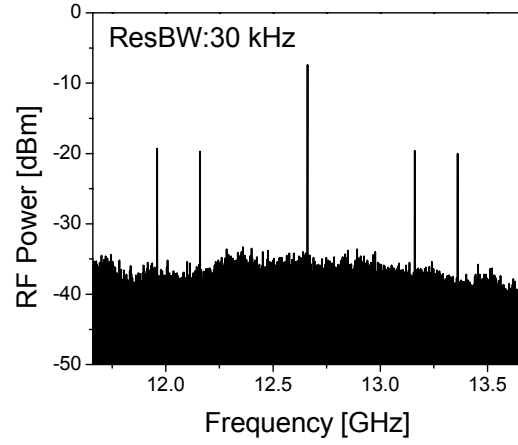


(c)

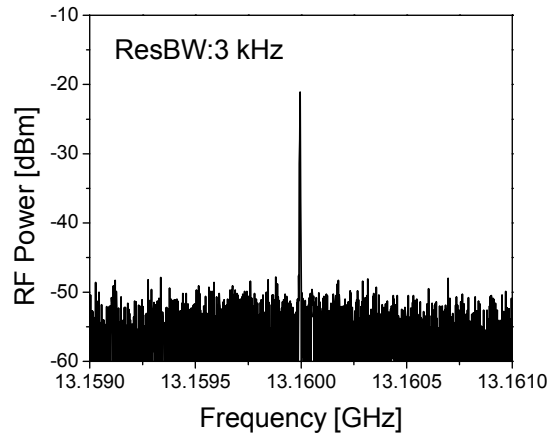
Figure 37: Optical heterodyning (a) optical spectrum of the data channel from the ML (b) optical spectrum of the selected probe channel from the injection locked SL. (c) optical heterodyning of the data channel and the LO probe channel



(a)



(b)



(c)

Figure 38: Experimental results of the coherent heterodyne detection of the two-tone analog signal. (d) heterodyne beat signal around the IF of 12.66 GHz before injection locking (e) heterodyne beat signal around the IF of 12.66 GHz after injection locking (f) the filtered heterodyne beat signal at 13.160 GHz (IF carrier 12.66 GHz +500 MHz) under a strongly injection locked state.

subject to two separate signal generators (HP 8648D and HP 8648B). The aggregate signal and spurious free dynamic range (SFDR) measurement are shown in Figure 36 (a) and (b). In the upper arm, a high finesse Fabry-Perot filter selects the single spectral comb of the injection locked SL, separated by two mode intervals from the data channel of the ML. Subsequently, the SL probe comb is combined with the analog data channel from the ML in another 3 dB fiber coupler. Figure 37 (a)-(c) shows the optical spectrum of heterodyne mixing between the two-tone, sinusoidally modulated analog data channel from the ML and selected SL probe comb from the Fabry-Perot filter. The combined signals prior to and subsequent to injection seeding are recorded using a 50 GHz photodiode and RF spectrum analyzer (HP 8565E), as shown in Figure 38 (a)-(c). The up-converted data signals were fully recovered only when the synchronization between the ML and SL was implemented by the injection locking. Finally, one of the upper sideband heterodyne beat signals centered at 13.160 GHz, which contains the 500 MHz analog RF signal information was successfully filtered out exhibiting a superb signal-to-noise ratio of 60 dB/Hz using a commercial microwave bandpass filter.

*Conclusion:* Optical heterodyne detection using synchronized MSLs based on optical injection locking technique was demonstrated. A passively modelocked local oscillator laser injection locked to a hybridly modelocked master oscillator laser formed broad-band discrete frequency probes, and a selected probe was heterodyned with a two-tone modulated data channel. Finally, dense frequency channel demultiplexing was performed by using a commercial bandpass filter. The experimental results revealed exceptional crosstalk rejection and a signal-to-noise ratio of over 60 dB/Hz of a single channel filtered from two-tone analog signals separated by only 200 MHz.

## 4.2 Coherent Ultra-Dense WDM System

Two different digital data detection experiments are performed by dual-mode hybrid injection locking technique as shown in Figure 39. One is the single channel data modulation experiment of CW injection locking without data. The other is the multi-channel data modulation experiment of CW injection locking without data. The other is the multi-channel data modulation

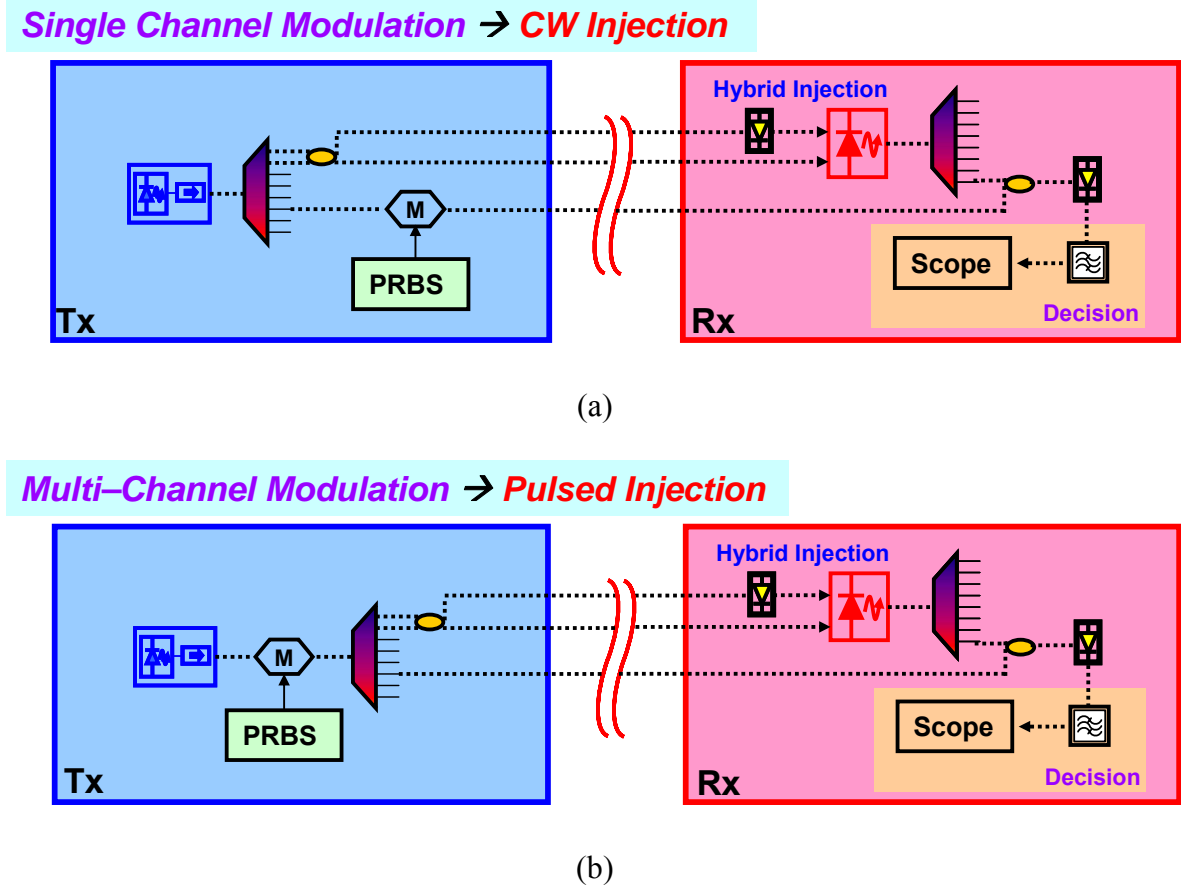


Figure 39: Schematic of coherent heterodyne digital data detection based on dual-mode hybrid injection locking. (a) single channel data modulation (injection locking without data). (b) multi-channel data modulation (injection locking with data).

experiment of pulsed injection locking with data. In these experiments, the dual-mode hybrid injection locking method is attempted to achieve more robust synchronization between a maser

MSL and slave MSL by injecting not only CW dual-mode from the master laser but also a beat signal of the dual-mode injection seed into the slave laser. Recovered clock signals from the passively modelocked slave laser are compared in both cases of injection locking with and without data. Finally, the performance of heterodyne detection is shown by the BER measurement.

### 4.2.1 Single Channel Modulation (CW Injection Locking)

The experimental setup is shown in Figure 40. The configuration of laser systems is same as the previous study.

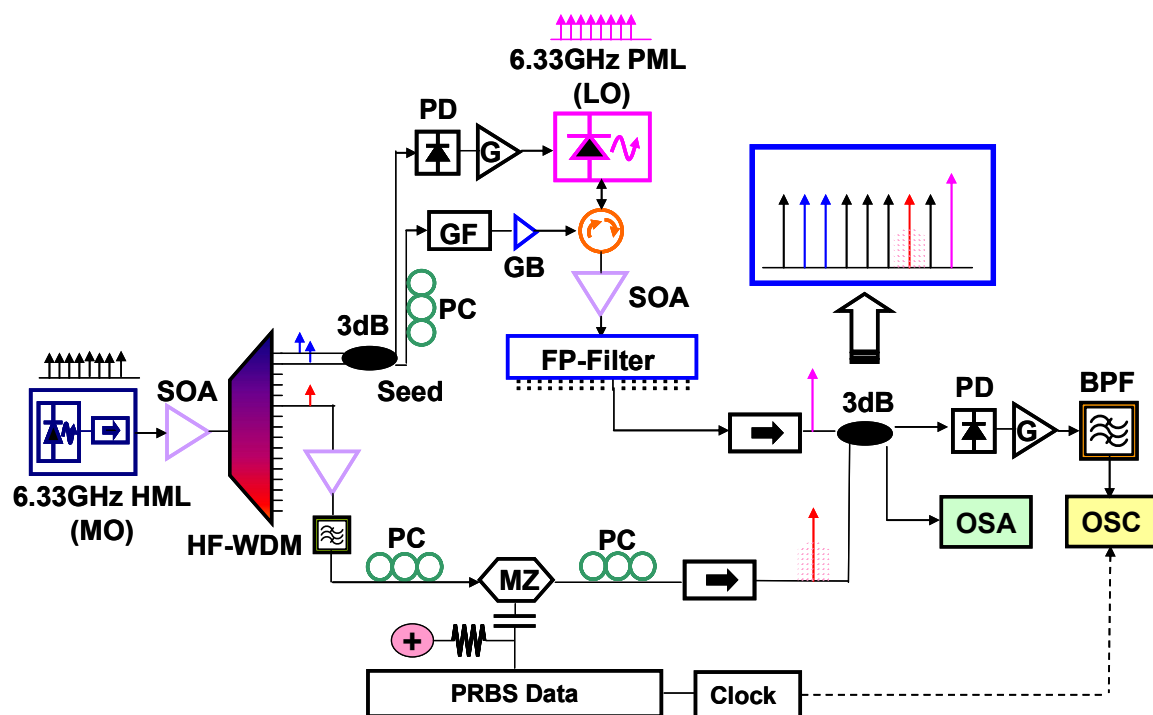
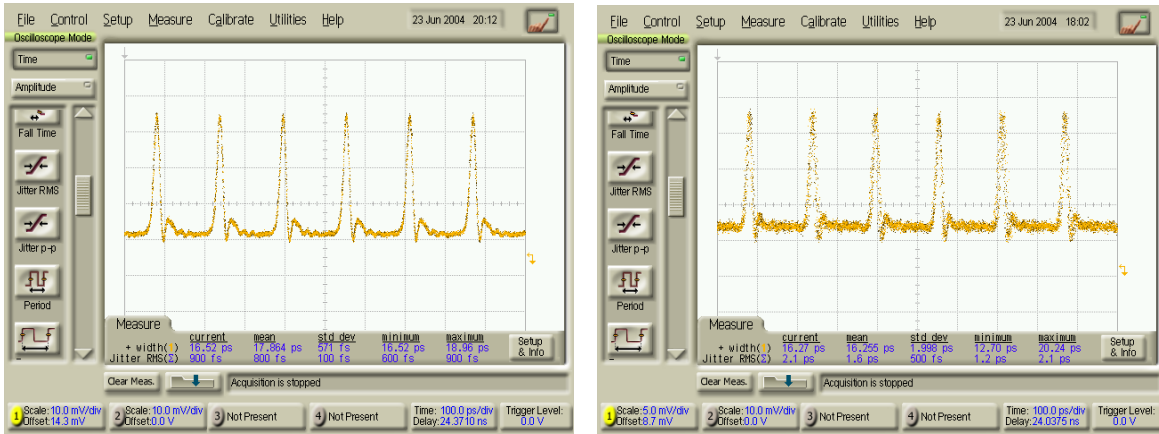


Figure 40: Schematic of the experimental setup for coherent heterodyne digital data detection in the case of single channel data modulation

In this experiment, the master MSL is considered as a multiwavelength WDM source for accommodating many different users. In other words, each separated channel from the single master MSL is considered as an independent WDM source. As shown in Figure 40, a data channel is selected from the channels in the HF WDM, which is separated by four times the mode interval from the seed channel, and imposed with RZ coded  $2^{23}-1$  long 500 Mb/s pseudo random bit sequence (PRBS).

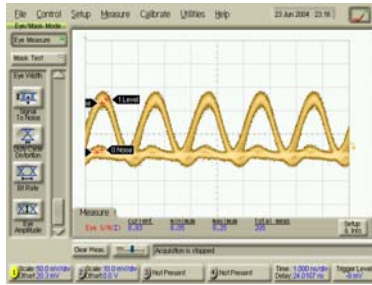


(a)

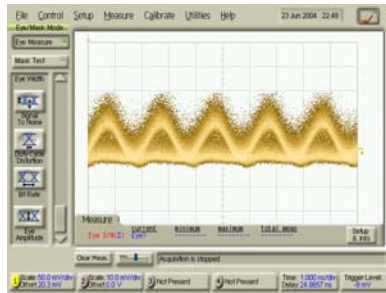
(b)

Figure 41: Clock Recovery. (a) Pulse train of the 6.33GHz hybridly modelocked master laser (Pulse Width: 17 ps, RMS Jitter: 600-900 fs )(b) Recovered pulse train from the dual-mode hybrid injection locked passively modelocked slave laser (Pulse Width: 16.2 ps, RMS Jitter: 1.2-2.1 ps).

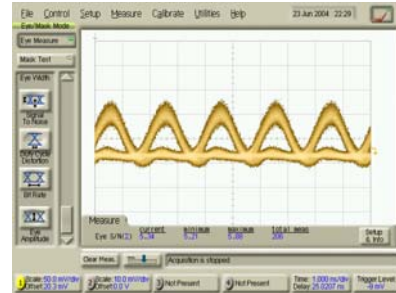
Figure 41 shows pulse train of the 6.33GHz hybridly modelocked master laser (ML) and recovered pulse train from the injection locked passively modelocked slave laser (SL). The average pulse width of the recovered clock was 17 psec and the measured RMS jitter of the



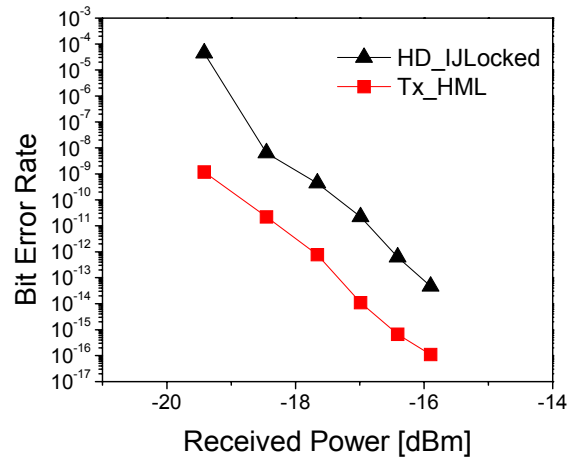
(a) Tx (500Mbps)



(b) Unlocked



(c) Locked



(d) BER

Figure 42: Coherent Heterodyne Digital Data Detection. (a) Eye diagram of the heterodyne detection of 500Mb/s PRBS data signals before injection locking (b) under injection locked state. (c) Bit error rate (calculated from measured SNR): square symbol (back to back direct detection of the PRBS data channel), triangle symbol (heterodyne detection of PRBS data under injection locked state)

recovered pulse was 2.1 psec which is approximately 2 times as large as that of the ML. In the upper arm, a high finesse Fabry-Perot filter selects the single axial mode of the injection locked SL as a local oscillator (LO) probe comb, separated by two mode intervals from the data channel of the ML. Subsequently, the LO probe comb is heterodyned with the PRBS data channel from the ML in another 3 dB fiber coupler, which generates the 12.66 GHz intermediate frequency (IF) heterodyne detected signal. Figure 42 (a) and (b) shows the eye diagrams of the heterodyne detected PRBS data prior to and subsequent to injection locking. The 500 Mb/s PRBS data signals were fully recovered only when the synchronization between the ML and the SL was successfully implemented by the dual-mode injection locking. It should be noted that the 12.66 GHz heterodyned signal is not resolved in the eye diagram since this frequency range is beyond the detection electronics. As shown in Figure 42 (c), the received power level of the heterodyne detection was 1.5 dB higher than that of the back to back direct detection measurement of the PRBS data channel at the same level of BER. The reason for the higher power penalty in the case of heterodyne detection is related to the limited LO probe power due to a high insertion loss of the FP filter and possible polarization mismatch in the optical heterodyning process.

#### **4.2.2 Multi-Channel Modulation (Pulsed Injection Locking)**

Considering practical coherent communication systems applications based on the synchronized MSLs, injection seeds possessed a certain data modulation is more often realistic. This is the case of pseudo-pulsed injection locking. The experimental setup is shown in Figure 43. The whole configuration of this experiment is same as the previous case of single channel modulation (CW injection locking without data), except that the entire optical combs of



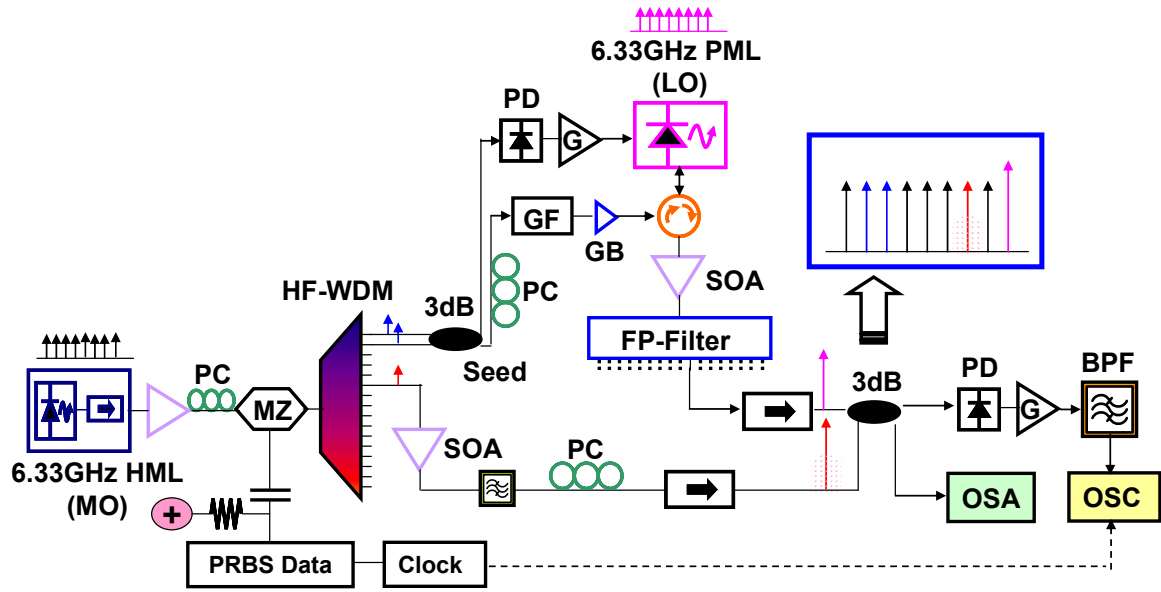
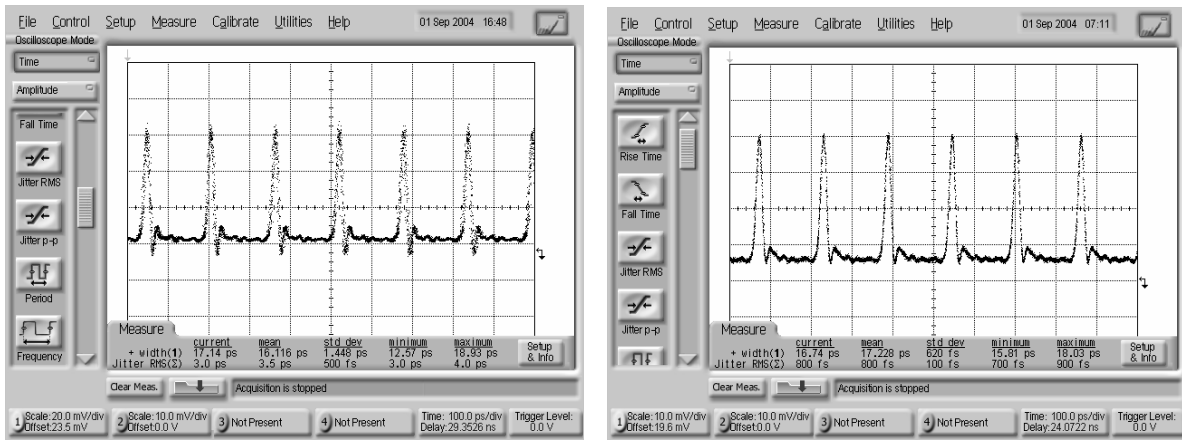


Figure 43: Schematic of the experimental setup for coherent heterodyne digital data detection in the case of multi-channel data modulation



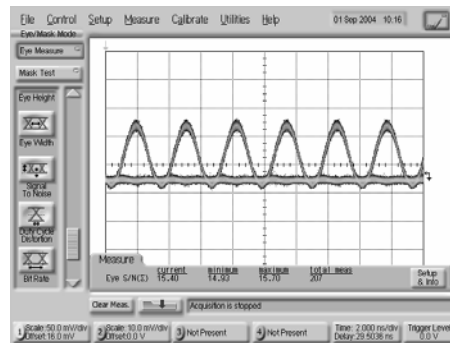
(a)

(b)

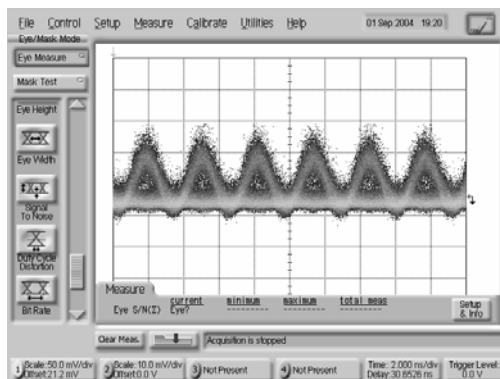
Figure 44: Data Clock Recovery. (a) Pulse train of the 6.33GHz hybridly modelocked master laser (Pulse Width: 17 ps, RMS Jitter: 700-900 fs) (b) Recovered pulse train from the dual-mode hybrid injection locked passively modelocked slave laser (Pulse Width: 16.1 ps, RMS Jitter: 3.0-4.0 ps).

the master MSL are modulated with RZ coded  $2^{23}-1$  long 316.5 Mb/s PRBS data before demultiplexing by HF WDM. Since the injection seeds also contain the data, performance of the injection locking is expected to be degraded by the relatively lower average seed power.

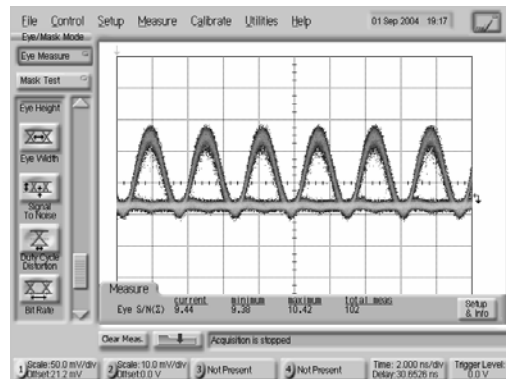
Figure 44 shows pulse train of the 6.33GHz hybridly modelocked master laser (ML) and recovered pulse train from the injection locked passively modelocked slave laser (SL).



(a) Tx (316Mbps)



(b) Unlocked



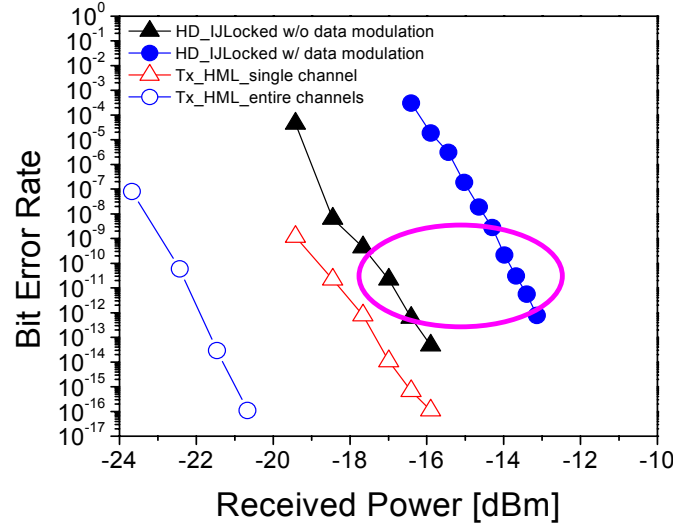
(c) Locked

Figure 45: Coherent Heterodyne Digital Data Detection. (a) Eye diagram of the heterodyne detection of 316.5 Mb/s PRBS data signals before injection locking (b) under injection locked state.

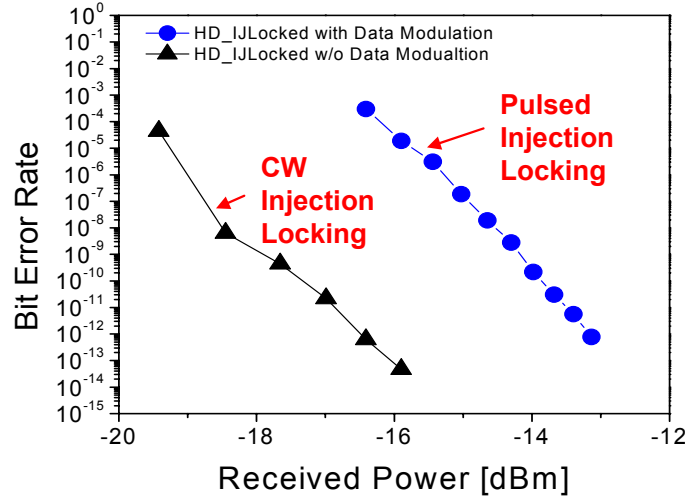
The average pulse width of the recovered clock was 16.1 psec and the measured RMS jitter of the recovered pulse was 3-4 psec which is approximately 2 times larger than previous single channel modulation (CW injection locking without data) case. Figure 45 (a)-(c) show the eye diagrams of the back-to-back directly detected PRBS data as well as the heterodyne detected PRBS data prior to and subsequent to injection locking. The 316 Mb/s PRBS data signals were fully recovered only when the synchronization between the ML and the SL was successfully implemented by the dual-mode injection locking. Error-free detection ( $\text{BER} \sim 10^{-9}$ ) was made by using a LO power less than  $\sim -16$  dBm under the robust hybrid injection locking technique.

#### 4.2.3 Comparison of BER

The calculated BER from the measured signal Q value in the case of multi-channel modulation (pulsed injection locking with data) is compared with that of the single channel modulation (CW injection locking without data) in Figure 46. Due to the relatively lower injection power, the case of multi-channel modulation showed twice increment of RMS jitter of the recovered clock in comparison with the case of single channel modulation. At the same level of BER, the received power level was measured to be 3 dB higher than the case of single channel modulation. However, the measured power is only from a single data channel out of several available data channels filtered from the HF WDM. All the powers of available data channels can be possibly gathered to improve BER. In the following chapter, details of arrayed coherent heterodyne receiver system are discussed.



(a)



(b)

Figure 46: Comparison of BER: (a) open circle symbol (back to back direct detection of entire data channels), closed circle (heterodyne detection of a single data channel under injection locked state). Triangle (single channel modulation case) (b) BER of a Heterodyne-Detected Single Data Channel: Triangle  $\rightarrow$  Single Channel Modulation Case (CW injection locking without data), Circle  $\rightarrow$  Multi-Channel Modulation Case (Pulsed injection locking with data).

### **4.3 Secure Coherent Communications**

On the basis of the previous studies on the characteristics of the MSLs and their effective synchronization techniques, in the following we will describe the experimental demonstration of efficient coherent homodyne detections for a spectrally phase-encoded optical code-division multiple access (SPE-OCDMA) system using synchronized MSLs, as a practical application of the synchronized MSL systems in secure coherent communications [50].

#### **4.3.1 Spectrally Phase-Encoded Optical CDMA (SPE-OCDMA)**

Recently, the SPE-OCDMA system based on synchronized MSLs has been recognized as a promising candidate for future secure coherent communications[45]-[47]. The simplicity of synchronous operation in MSLs is a very attractive characteristic to consider MSLs as sources of phase-locked transmitters and LOs. The fixed phase relationship of the optical frequency combs of the MSLs facilitates spectral phase encoding capability [48], [49]. The short time durations (broad bandwidth) of the optical pulses from the MSL has the potential to provide high processing gain [50], defined as the bandwidth ratio between the data rate and the spectral bandwidth of the optical pulses, for the SPE-OCDMA system.

Figure 47 shows the schematic of the architecture of the SPE-OCDMA system based on synchronized MSLs. In this system, a number of MSLs serve as synchronized transmitters and receivers by means of the dual-mode injection locking technique. It should be noted that a single comb source could be used and distributed to individual users to establish a multiplicity of phase coherent comb transmitters. Several matched phase encoders and decoders are used to implement the optical code-division multiplexing (OCDM) for the optical CDMA system.

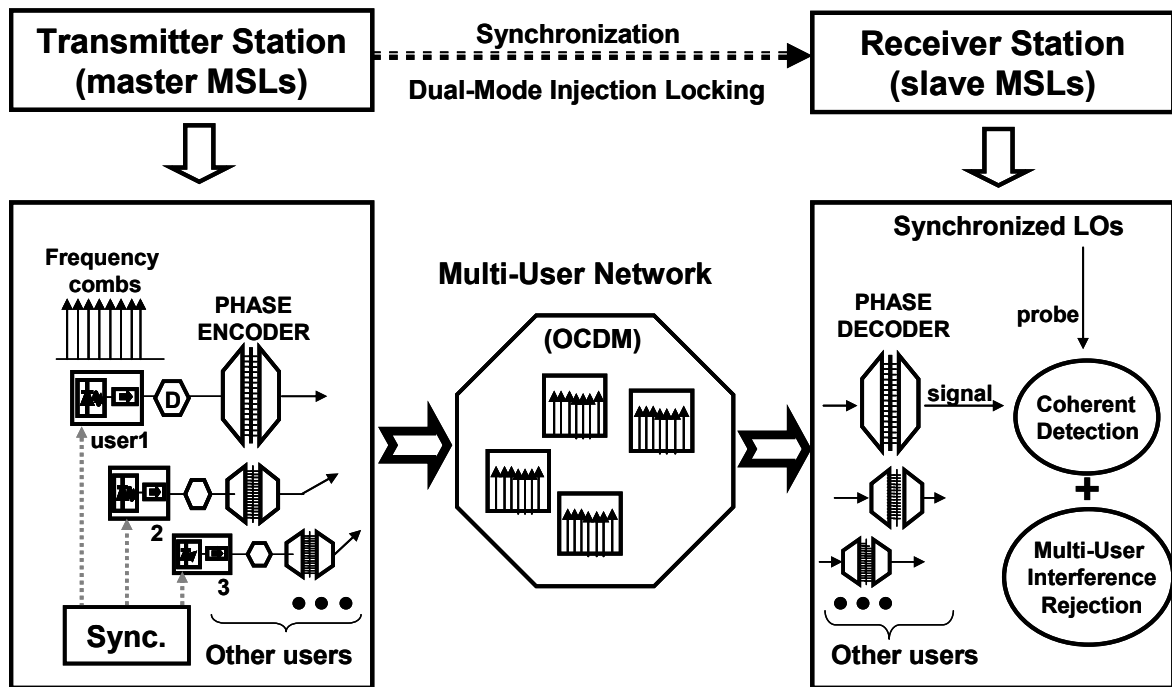


Figure 47: Architecture of the overall spectrally phase-encoded optical CDMA (SPE-OCDMA) system based on synchronized MSLs. D: data modulation; OCDM: optical code-division multiplexing.

Each user employs distinct phase code sets for the spectral phase scrambling of the optical frequency combs from the transmitter MSLs, to encode and spread the information-bearing signal through the multi-user network. At the receiver station, only the intended receiver knows the code and can decode the desired signal and reject the other signals owing to the orthogonality of codes among the multiple users.

In most coherent optical CDMA applications, the system performance is limited by an increase in the bit rate and the number of active users due to the sharing of channel resources with other users. In consequence, to improve the SPE-OCDMA system performance, it is important to develop efficient data receiver systems which can provide higher detection sensitivity as well as strong multi-user interference (MUI) rejection.

In addition, large intensity noise can be another considerable impairment for the SPE-OCDMA system based on the MSLs. However, utilizing a balanced optical receiver in which the photocurrents from two output branches are subtracted, the relative intensity noise (RIN) from the optical sources can be significantly reduced [52].

#### **4.3.2 Coherent Pulse Detection and Multi-Channel Coherent Detection**

Figure 48 illustrates two concepts of efficient coherent homodyne detection schemes, which will be referred to as coherent pulse detection (CPD) and multi-channel coherent detection (MCCD) based on a differential balanced detection for the SPE-OCDMA using synchronized MSL systems. In the CPD system, after the decoding process, the recombined signal channels for an intended user are homodyned with the LO pulses from the synchronized SL. On the other hand, in the MCCD system, for a single user the decoded signal channels conveying identical

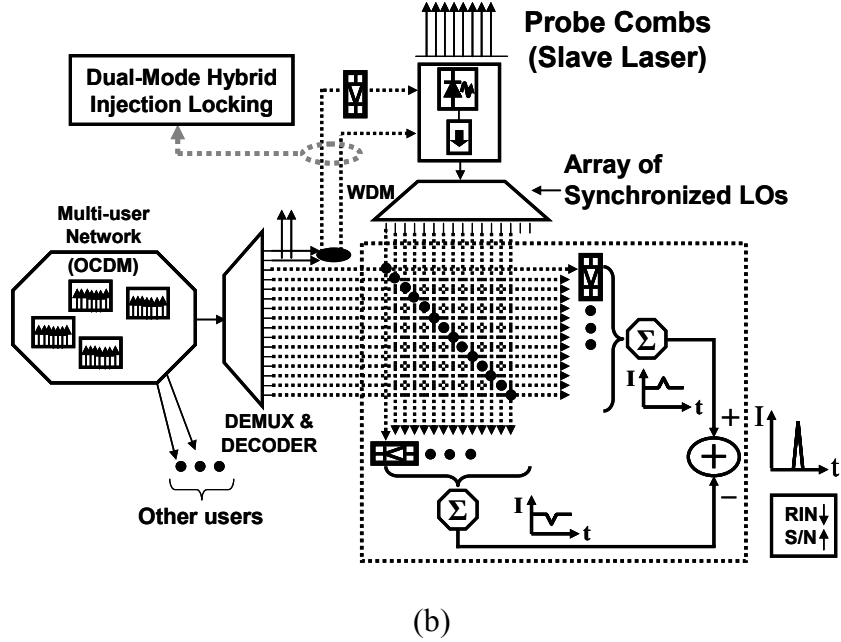
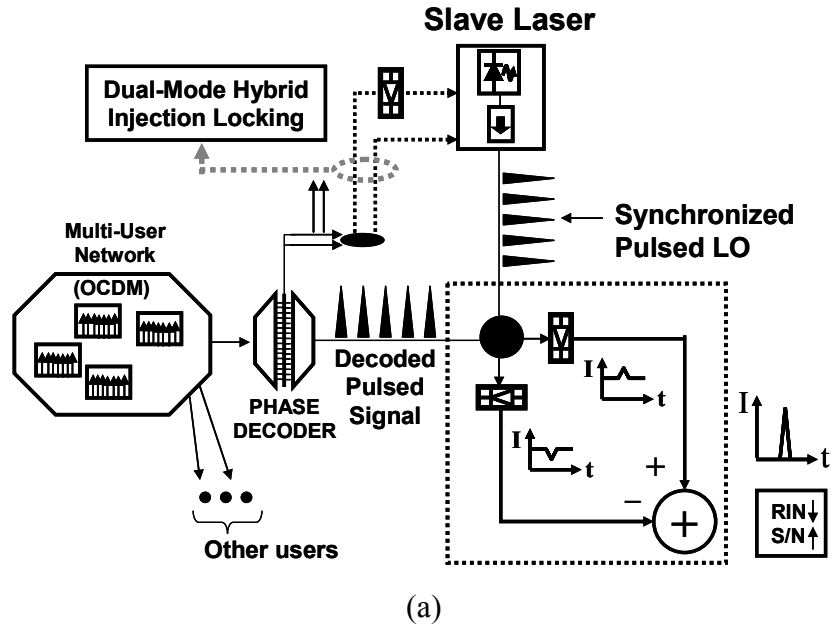


Figure 48: Schematic of the architecture of efficient coherent homodyne receivers for the SPE-OCDMA based on synchronized MSLs. (a) CPD (b) MCCD.



data information are individually homodyned with an array of LOs generated from the synchronized SL and the recovered data is combined together electrically. Compared with direct detection system, due to the synchronous detection mechanism and the improved detection sensitivities, both CPD and MCCD systems can provide strong signal selectivity in the presence of severe MUI without recourse to optical time gating or nonlinear thresholding devices.

In the following sections, we demonstrate CPD and MCCD by using a single free-space balanced homodyne receiver with two large-area photodetectors. First, we show the generation of 20-GHz optical frequency combs and pulses by using a 10-GHz external cavity grating-coupled MSL system combined with a 20-GHz micro-ring resonator spectral de-interleaver. It should be mentioned that the use of the 20-GHz channel spacing is to insure complete channel separation considering the resolution of gratings in the MCCD experiment. Second, we discuss the experimental results of CPD and MCCD, as compared with direct detection.

**1) 10-GHz grating-coupled mode-locked semiconductor laser system:** In this experiment, the cavity length of the previous grating-coupled MSL was adjusted to generate 10-GHz optical frequency combs, subsequently sent into the 20-GHz micro-ring resonator spectral de-interleaver. Figure 49 (a) shows the conceptual diagram of the generation of the 20-GHz frequency channels. Figure 49 (b) and (c) show the optical spectrum of the 10-GHz MSL and the filtered 20-GHz frequency channels of the MSL after the 20- GHz de-interleaver, respectively. Figure 50 (a) and (b) show sampling oscilloscope traces of the 10-GHz MSL pulses and the interleaved 20-GHz pulses, respectively. The sampling scope traces were measured by using a 50-GHz photodetector. Figure 50 (c) and (d) show the intensity autocorrelation measurement of the 10-GHz MSL pulse and the interleaved 20-GHz pulse corresponding to the optical spectrum in Figure 49 (b) and (c), respectively. The pulse duration directly from the 10-GHz MSL was measured to be 16.3 ps

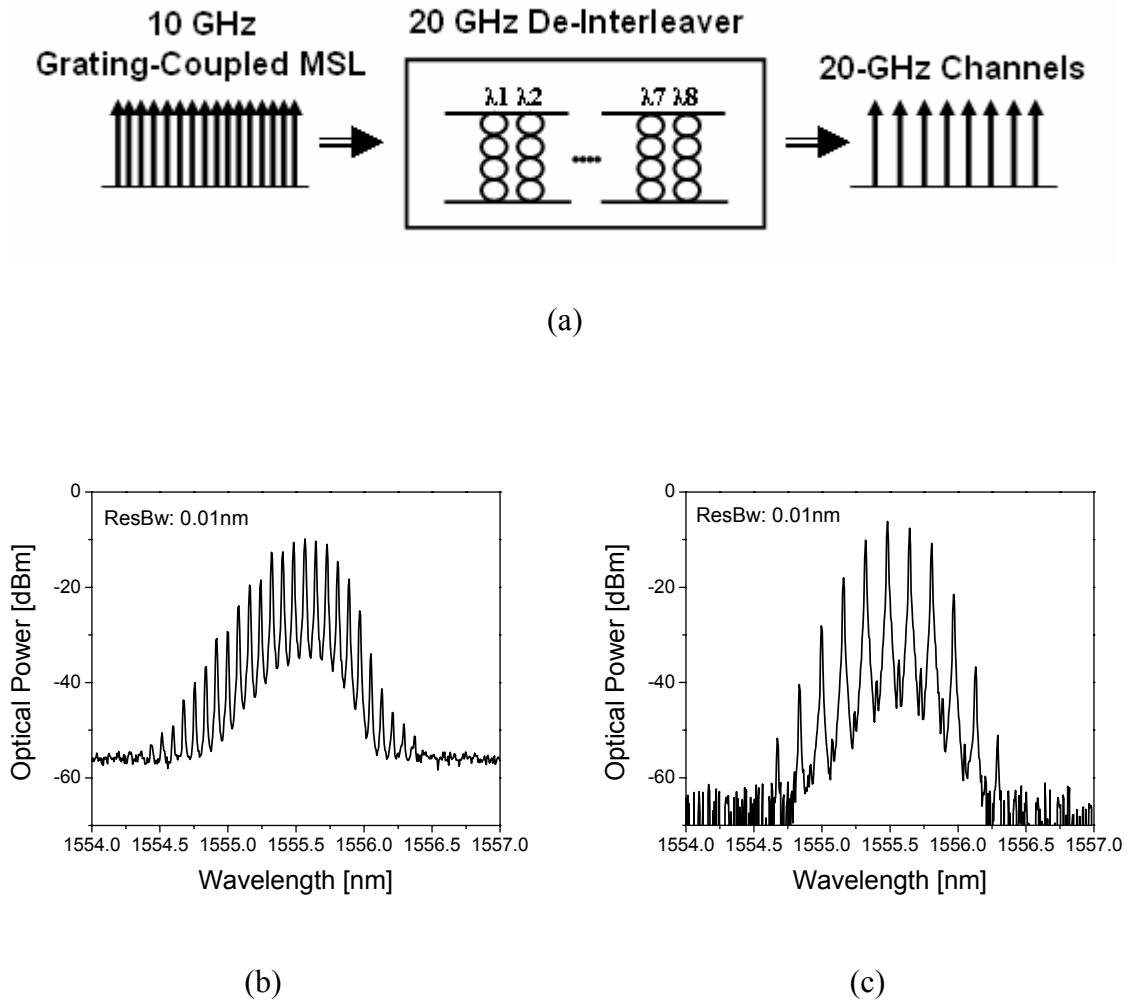
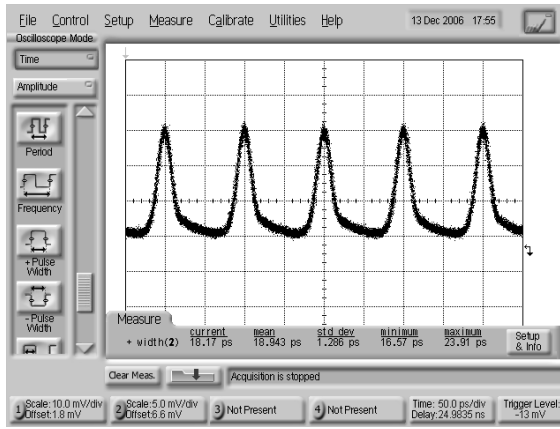
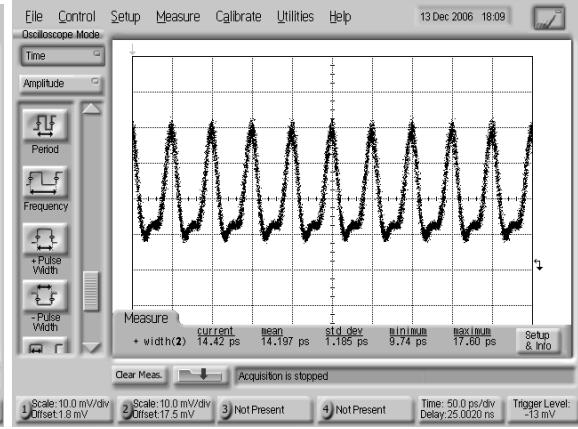


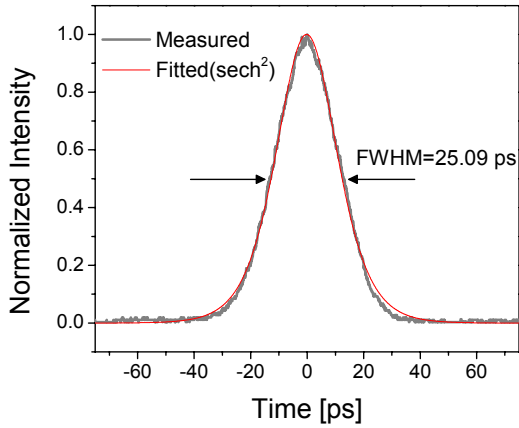
Figure 49: 10-GHz external cavity grating-coupled MSL combined with a 20-GHz microring resonator interleaver. (a) conceptual diagram of 20-GHz frequency channel generation (b) optical spectrum of the 10-GHz hybridly MSL (c) optical spectrum of the filtered 20-GHz channels out of the 10-GHz MSL spectrum through the 20-GHz interleaver.



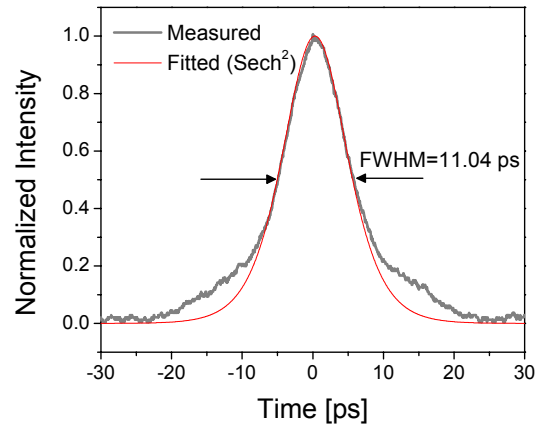
(a)



(b)



(c)



(d)

Figure 50: Pulse measurements of the 10-GHz external cavity grating-coupled MSL system combined with the 20-GHz de-interleaver (a) sampling oscilloscope trace of the 10-GHz MSL pulse train before the 20-GHz de-interleaver (b) 20-GHz pulse train after the 20-GHz de-interleaver (c) intensity autocorrelation measurement of the 10-GHz MSL pulse before the 20-GHz de-interleaver (d) intensity autocorrelation measurement of the 10-GHz MSL pulse before the 20-GHz de-interleaver.

(assuming a hyperbolic secant pulse shape). The time-bandwidth product was 0.9, which indicated that the measured pulse width is 2.9 times larger than the transform-limited pulse width. The pulse duration after the 20-GHz de-interleaver was measured to be 7.2 ps (assuming a hyperbolic secant pulse shape). It should be noted that the pulse shortening is caused by a dispersion compensation effect by the micro-ring resonator de-interleaver.

**2) Experimental setup of a free- space coherent homodyne receiver system for CPD and MCCD:** In order to demonstrate CPD as well as MCCD, a Mach-Zehnder interferometric homodyne detection system was built as shown in Figure 51. In this experiment, the previous hybridly MSL was simultaneously used as a data transmitter as well as a local oscillator (LO)

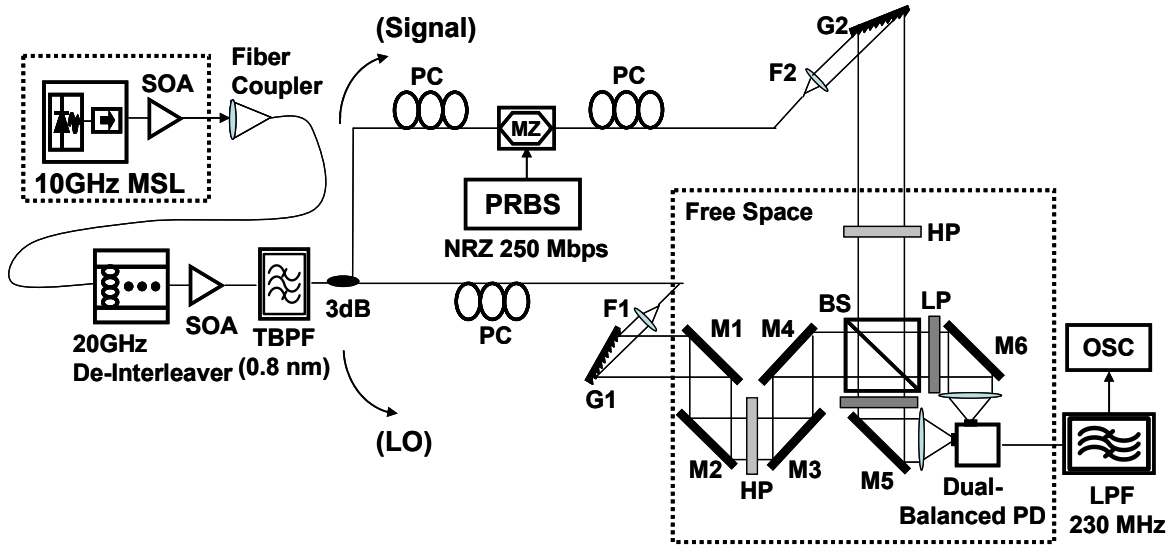
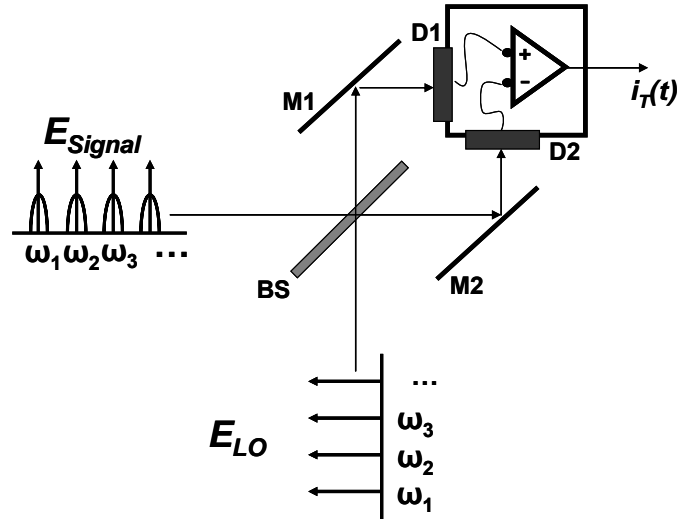


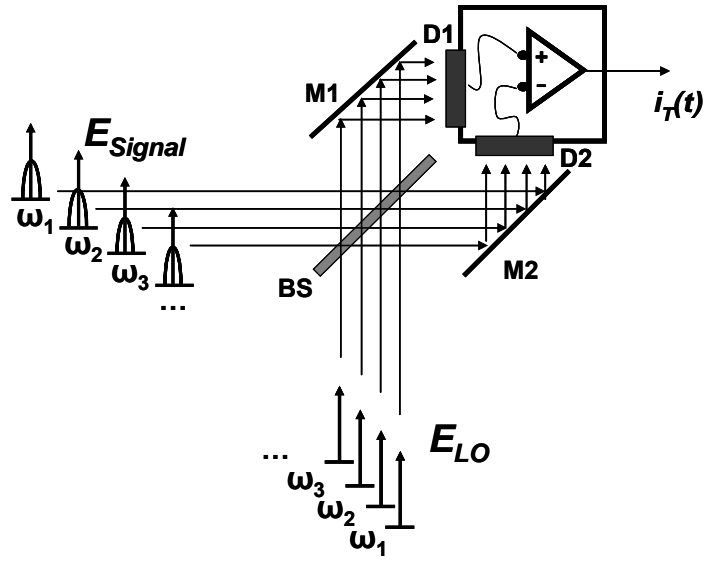
Figure 51: Experimental setup for the CPD and MCCD demonstration using a 10-GHz MSL (M1~M6: mirror; G: grating; SOA: semiconductor optical amplifier; TBPF: tunable bandpass filter; MZ: Mach-Zehnder intensity modulator; F1 and F2: fiber to free space launcher; BS: beam splitter; PC: polarization controller; HP: half wave plate; LP: linear polarizer; PD: photodetector; LPF: low pass filter; OSC: oscilloscope)

satisfying the required synchronization condition. For the practical SPE-OCDMA systems using synchronized MSLs, it should be noted that two separate, individual MSLs can be used where one MSL is frequency and phase-locked to the other by injection locking as shown in section III-A[7]. After the 20-GHz de-interleaver, the filtered frequency channels of the laser output were divided into two arms of the Mach-Zehnder interferometric homodyne detection system. The signal beam imposed with NRZ modulated  $2^{10}-1$  long 250 Mb/s PRBS data is recombined with the LO beam through a free-space beam splitter (BS). Subsequently, the combined beam goes to the differential balanced detection setup based on a free-space dual-balanced receiver with an electrical bandwidth of 800 MHz. The diameter of the photodetectors in the balanced receiver is 0.1 mm. The responsivity is  $\sim 1$  A/W. The saturation power of the photodetectors is 1 mW. Finally, data signals were recovered by using an electrical lowpass filter (LPF) with a bandwidth of 230 MHz in order to consider only the baseband signal. It should be noted that differential balanced detection provides suppression of the relative intensity noise (RIN) of optical sources, as well as a 3-dB sensitivity improvement as compared with direct detection.

Figure 52 shows the schematic of the homodyne detection processes in CPD and MCCD. For the CPD experiment, the gratings (G1 and G2) with a groove density of 1050 lines/mm in the setup were initially set up for the 0th order configuration so that the entire data channels can be homodyned with the synchronized pulsed LO at a single spot on the photodetector area in the manner of a pulse-to-pulse temporal overlap. A free space movable delay stage (M2, M3) was used to control the temporal overlapping of the signal pulses with the LO pulses for the CPD experiment. On the other hand, by rotating the gratings for the 1st order configuration the MCCD was performed. In the MCCD, spatially and spectrally resolved signal channels and the LO probes are individually homodyned at distinctively separate spots on the photodetector area, in



(a) CPD

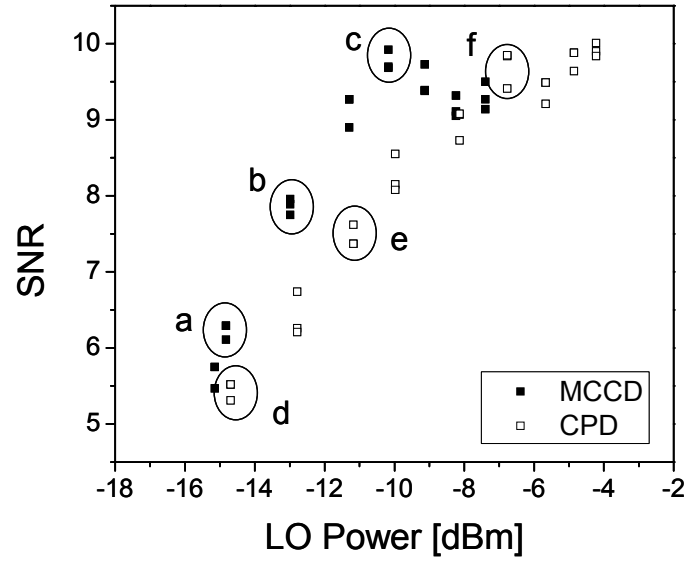


(b) MCCD

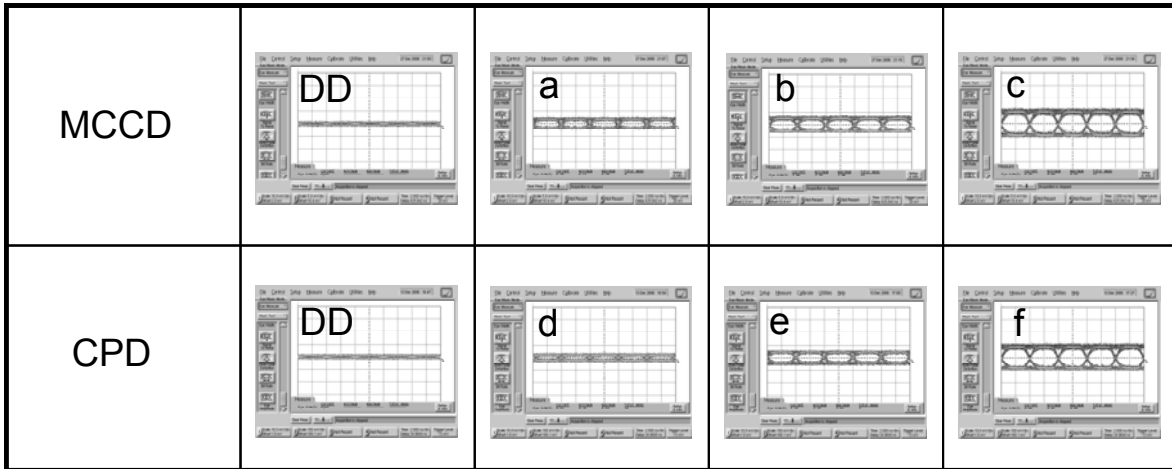
Figure 52: Schematic of the homodyne processes in CPD and MCCD (BS: beam splitter, M1 and M2: mirror, D1 and D2: photodetector).

the manner of channel-to-channel spatial overlap. Each beam diameter was  $\sim 4 \mu\text{m}$ , and spatial channel separation was  $\sim 10 \mu\text{m}$ . Likewise, for the MCCD each of the path lengths from the two gratings to the beam splitter (BS) was matched in order to maximize individual spatial overlapping of signal channels and LO probes at the photodetectors in the balanced receiver. As in any coherent detection process, control of the relative phase difference between the signal beam and the LO beam is crucial to realize an idealized coherent homodyne detection scheme in both CPD and MCCD.

**3) Comparison of the experimental results of CPD and MCCD:** By increasing the LO power, the SNR was measured in both CPD and MCCD configurations with respect to a fixed signal power of -21.8 dBm. Figure 53 shows the SNR measurement and the corresponding eye diagrams of the CPD and MCCD. As shown in Figure 53 (b), the eye diagram of direct detection (DD) is composed of multiple superimposed traces of the signal beam measured by blocking the LO beam after the fiber-to-free space launcher and one of the windows of the balanced receiver. The directly detected SNR was measured to be 2.6. In comparison with the direct detection, a noticeable SNR improvement was observed in both CPD and MCCD. In MCCD, by mixing an LO power of  $\sim -10.2$  dBm with the original signal, an SNR of 9.9 was obtained from the coherently received data signals, whereas, in the CPD an LO power of more than  $\sim -6.8$  dBm was required to obtain an SNR of 9.8 from the coherently received data signals. As shown in Figure 53 (a), the approximately 2~3 dB improvement in sensitivity obtained in MCCD compared with CPD is mainly because MCCD has an advantage in a path-length error over CPD, i.e., more stringent path-length matching in the interferometer is required for CPD. For example, a pulse duration of 7 ps can tolerate only a small path-length error such as 0.2 mm in order to acquire the 90 % temporal overlapping between the signal and the LO pulses. Whereas in MCCD



(a)



(b)

Figure 53: Experimental results of CPD and MCCD (a) SNR measurements of CPD and MCCD (Solid symbol: MCCD, open symbol: CPD) (b) eye diagrams of the direct detection of the initial signal and coherent homodyne detections (scale: 10mV/Div.)



utilizing spatially and spectrally resolved optical frequency combs, the channel-to-channel spatial overlapping is much less sensitive to the path-length error. In addition, the effect of spatial shifts of the spectral channels due to the laser frequency drift is almost negligible within the coherence length of the laser source. It should be mentioned that from the estimated bit-error-rate (BER) values based on the measured SNR, error-free (BER less than  $10^{-9}$ ) coherent detection has been obtained with a LO power level of -13 dBm and -15 dBm in the CPD and the MCCD, respectively.

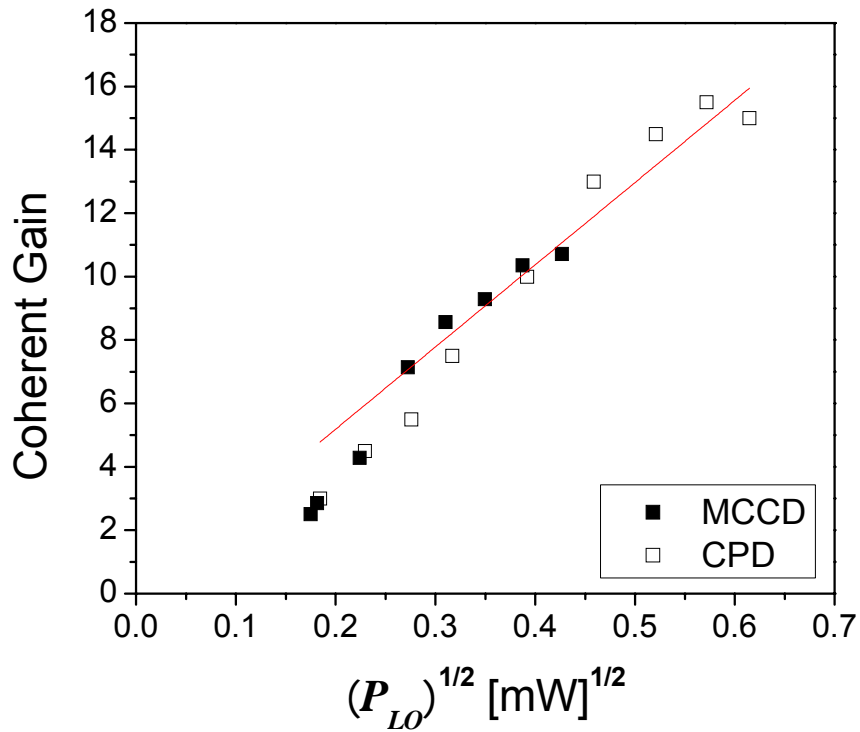


Figure 54: Coherent gain versus LO power

Figure 54 shows the LO power dependence of coherent gain in the CPD and MCCD. The coherent gain is the quantity which can show the efficiency of the coherent beating process depending on LO power, defined as the maximum eye opening ratio of coherent detection with respect to direct detection. When the measured baseband signal voltage output of the coherent detection ( $V_{CD}$ ) and the direct detection ( $V_{DD}$ ) are given as,

$$\begin{aligned} V_{CD} &= 2 \cdot R \cdot R_L \cdot \sqrt{P_{sig} \cdot P_{LO}} \sin(\Delta\phi) \\ V_{DD} &= R \cdot R_L \cdot P_{sig} \end{aligned} \quad (4.1)$$

where,  $R$  is the detector responsivity,  $R_L$  is the load resistance,  $P_{sig}$  is the optical power of the signal,  $P_{LO}$  is the optical power of the LO, and  $\Delta\phi$  is the phase difference between the signal and the LO, then coherent gain can be given by

$$G_C \equiv \frac{V_{CD}}{V_{DD}} \quad (4.2)$$

With a fixed signal power, the coherent gain in both CPD and MCCD has the same square-root dependence on LO power.

$$G_C \propto \sqrt{P_{LO}} \quad (4.3)$$

Our experimental results of CPD and MCCD agree well with the square-root LO power dependence of the coherent gain. A high coherent gain of over 10 dB, as well as, an SNR

improvement of over 5 dB compared with direct detection were obtained in both CPD and MCCD.

### 4.3.3 High-Speed MSM Balanced Receiver

In the previous section, we have experimentally demonstrated CPD and MCCD at a data rate of 250 Mbps. Higher data rates can be implemented by using commercially available fiber-pigtailed high-speed ( $>10$  GHz) balanced receivers. However, as shown in Figure 52, the synchronous coherent detection techniques based on a single free-space balanced receiver with large area high-speed photodetectors are not only attractive for the SPE-OCDMA but also for other applications such as two dimensional photonic signal processing. To illustrate this idea, we have developed a free-space balanced receiver utilizing high-speed metal-semiconductor-metal (MSM) photodetectors with large sensor areas. At present, we have been able to demonstrate only CPD. For MCCD, information regarding the size, spacing, and orientation of the interdigitated metal fingers of the MSM detector is necessary for the alignment of the spatially resolved frequency combs. This information was not available for the commercial MSM detectors used in this experiment.

For the 2.5-Gbps CPD demonstration, the configuration of a free-space balanced receiver using high-speed MSM photodetectors is shown in Figure 55. The data was NRZ modulated  $2^{10}$ -long PRBS. The configuration of a free-space balanced receiver system using the high-speed MSM photodetector is shown in Fig. 23. The rise time of the MSM photodetector used in this experiment was 40 ps. The 3-dB frequency response was measured to be approximately 5 GHz. The effective sensor area is  $0.2 \times 0.2 \text{ mm}^2$ . The responsivity is 0.4 A/W. The physical structure

of the MSM photodetector is similar to the integrated photoconductor with alternated metal fingers so that either a positive or a negative bias can be applied to the MSM photodetectors. As shown in Figure 55, the MSM photodetector was directly connected to a bias tee in order to be biased with a proper DC voltage while passing AC signals. The 3-bandwidth of the bias tee used in this experiment is  $\sim 15$  GHz, and the 3-dB low frequency cut-off is 12 kHz. For CPD demonstration, optical pulses with a time duration of  $\sim 16$  ps directly from the 10-GHz hybridly modelocked grating-coupled MSL was simultaneously used as a transmitter as well as a LO in an ideal synchronization condition. Considering lower dark current noise performance of a forward-biased MSM detector, a voltage of +7 V was applied and slightly tuned to make power balancing

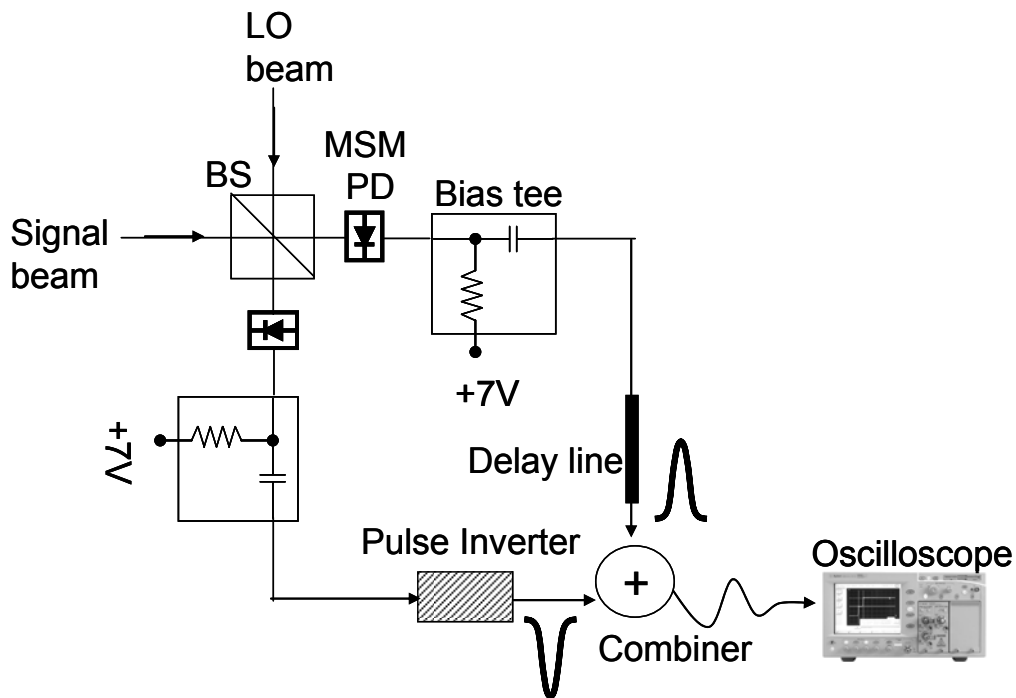
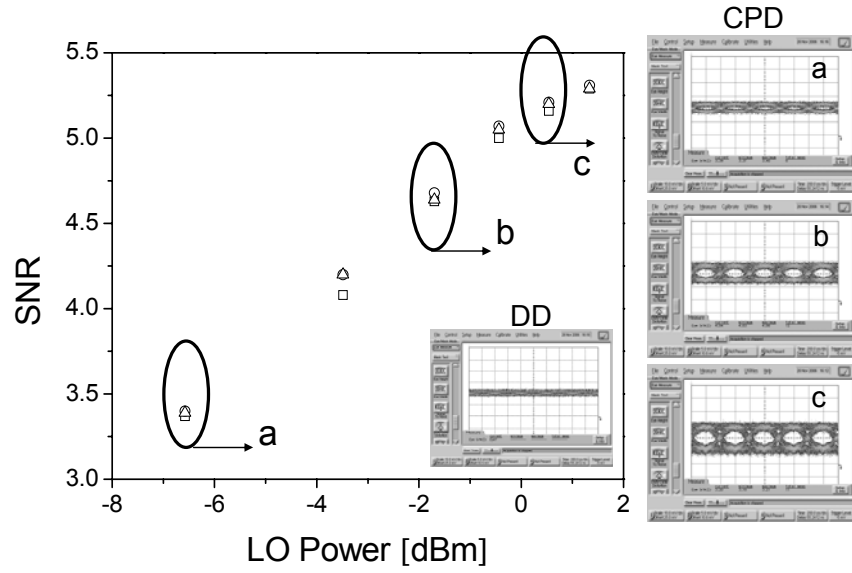
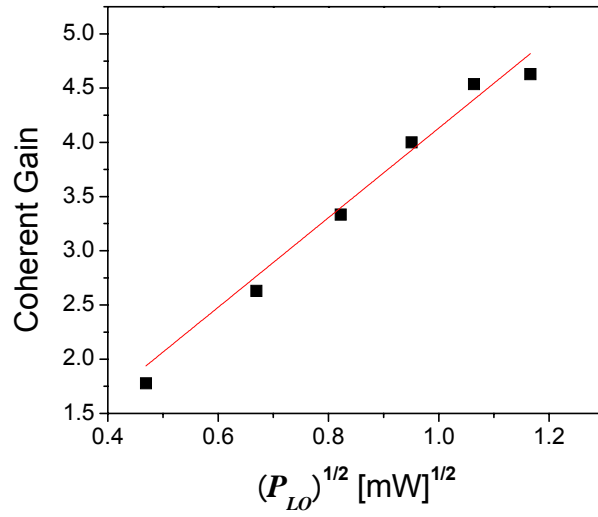


Figure 55: Schematic of a balanced receiver system based on high-speed MSM photodetectors



(a)



(b)

Figure 56: Experimental results of CPD at the data rate of 2.5 Gbps (NRZ coded  $2^{10}-1$  long PRBS) (a) SNR measurements in the CPD (Different symbols stand for different measurements) and the corresponding eye diagrams (b) Coherent gain vs. LO power.

and subsequently the pulses from two different arms in the balanced receiver were combined between the two MSM detectors in the balanced receiver. As shown in Figure 55, an inverting transformer was used to change the polarity of the pulses in one of the balanced receiver arms, through an electrical combiner to complete a differential balanced receiver.

A measurement of SNR versus LO power and the corresponding eye diagrams as well as coherent gain are shown in Figure 56. The signal power was initially fixed at -11 dBm and SNR was measured to be less than 1.5. In comparison with the direct detection, a noticeable improvement was observed in CPD, as shown in Figure 56 (a). By mixing an LO power of  $\sim 1$  mW with the signal, an SNR of  $\sim 5.2$  was obtained. In this balanced receiver system, it is important to have an electrical combiner which has higher port isolation in order to prevent signal degradation due to an interference effect. The round-shaped eyes as shown in Figure 56 (a) is due to the limited bandwidth of the electrical combiner (Bandwidth: 10-1500 MHz) which has a high port isolation of  $\sim 30$  dB. Figure 56 (b) shows coherent gain of the CPD experiment as a function of LO power. A coherent gain of more than 6 dB has been obtained at the LO power of  $\sim 0$  dBm. This is lower than the result shown in the previous section because of the relatively low responsivity of the MSM detectors. The measured coherent gain result agrees well with the theoretical square-root dependence on LO power.

## CHAPTER 5: CONCLUSION

### 5.1 Summary

High-speed external cavity grating-coupled and mirror-coupled modelocked semiconductor laser (MSL) systems using a saturable absorber incorporated two-section curved semiconductor optical amplifier were developed. The generation of short optical pulses with a multiplicity of phase coherent optical frequency combs by hybrid mode-locking was demonstrated. Laser spectral bandwidth of  $\sim 0.6$  nm (grating-coupled MSL) and  $\sim 3$  nm (mirror-coupled) were obtained at the center wavelength around 1555 nm. Optical pulses with a pulse width of 10~20 ps as well as a multiplicity of phase coherent optical frequency combs were obtained. Average output power directly from the MSL systems was few mW, however, through external power amplification with an addition semiconductor optical amplifier (SOA) an average power more than 50 mW was easily obtained.

The Pound-Drever-Hall (PDH) frequency stabilization technique was applied to stabilize the laser frequency. The laser frequency was successfully locked up a frequency range of less than 350 MHz. After the laser frequency stabilization, a linewidth of 3 MHz, and a relative intensity noise (RIN) below -150 dB/Hz with a 3-dB improvement of modal RIN from a filtered single axial mode were obtained from the hybridly modelocked grating-coupled MSL.

Laser oscillator synchronization of two independent MSLs (master laser: hybridly modelocked grating-coupled MSL, slave laser: passively modelocked mirror-coupled MSL) and a tunable laser to a MSL is demonstrated by using a novel method of injection locking technique, called dual-mode injection locking and modulation sideband injection technique, respectively. Dynamic locking behavior and locking bandwidth was theoretically and experimentally studied.

Stable injection locking was performed with an injection seed power of few microwatt. In the modulation sideband injection, with incoming average optical power of less than -20 dBm (before slave laser output coupler), the noise sidebands from the SL carrier were suppressed by 42 dB at 100 kHz offset. In the dual-mode injection locking, at the seed power level of -29.17 dBm (before slave laser output coupler), the noise sidebands of the SL carrier were suppressed by more than 35 dB at 100 kHz offset. A locking bandwidth of 3 MHz, showing the carrier phase noise suppression of more than 30 dB at 100 kHz offset, was obtained at the seed power -21.23 dBm.

Coherent heterodyne detections based on a synchronized mode-locked semiconductor laser system were demonstrated for many applications in several high-speed photonic systems such as coherent analog photonic links, a broad-band coherent probe system, ultra-dense WDM systems. In the analog heterodyne detection experiments, a signal-to-noise ratio of more than 60 dB/Hz was demonstrated in bandpass filtered RF two-tone modulated optical signals. In digital heterodyne detection experiments, error free operation using digital signal modulation with a RZ coded  $2^{23}-1$  long 316 and 500 Mb/s pseudo random bit sequence (PRBS) was demonstrated.

Finally, two efficient coherent homodyne balanced detection techniques for a SPE-OCDMA system were demonstrated. The detection techniques are called coherent pulse detection (CPD) and multi-channel coherent detection (MCCD) based on a single free-space balanced receiver. A high coherent gain of over 10 dB as well as an SNR improvement of over 5 dB compared with direct detection have been demonstrated in both CPD and MCCD. Furthermore, using two high-speed metal-semiconductor-metal (MSM) photodetectors, a high-speed free-space balanced receiver system was developed. CPD at a higher data rate of 2.5 Gb/s (NRZ modulated  $2^{10}-1$  long PRBS) was demonstrated. As a result, the experimental results



indicated that the MCCD and CPD configurations based on a single balanced receiver can both provide high ( $>10\text{dB}$ ) coherent gain. Further, the MCCD receiver offers 2~3dB of SNR improvement relative to CPD at the cost of a more complex receiver configuration. Simulations suggest both approaches have the potential of strong multi-user interference rejection enabling the accommodation of multiple users in an SPE-OCDMA system for future secure coherent communication applications.

Beyond communication applications, we believe that the synchronized coherent optical frequency combs and short pulses from MSLs are very promising optical sources for a variety of coherent high-speed photonic systems.

## **5.2 Future Studies**

In this dissertation, several coherent heterodyne signal detections experiments have already reflected some of the applicable features for microwave photonic link systems as well as signal processing. Recently, ubiquitous antenna systems based on radio-on-fiber (RoF) technology have been proposed for next generation mobile radio communication networks [56]-[60]. In this system, microcellular radio base stations (RBS) deployed over the service area are connected to a central control station (CCS) by optical fibers. Radio signals are transmitted over an optical fiber link among RBSs and CCS with their original RF signal format kept. By utilizing synchronized MSL systems, some of the practical applications in RoF photonic link system, for instance, millimeter wave generation, data up-and-down link systems, and etc. would be good topic to be investigated. Some other interesting topics are coherent detections related to the previously developed multi-channel coherent detection technique using a large area

photodetector. Since the MCCD using a single large area photodetector showed the many advantageous features for the application in high-capacity coherent photonic systems and two dimensional high-speed optical signal processing [61,62] as well as pattern recognition based on phase correlation technique [63].

## **APPENDIX A: HIGH-SPEED MODELOCKED SEMICONDUCTOR LASER SIMULATION CODE IN MATLAB**

- `clc; clear all; close all; format long`
- `% Initial vector definitions`
- `%%%`
- `m = 1024; m2 = m/2; %Vector length`
- `i = 1:m; %Frequency and time vector`
- `fmax=1024; fmin=0; fspan=fmax-fmin;`
- `finc=fspan/m % resolution 1 GHz, full frequency span, 1024 GHz;`
- `tinc=(1/finc)*(1/m) %time increment 0.9765625 ps(~1ps)`
- `% Mode spacing and width`
- `%%%`
- `detun=5*finc;% 5 GHz (laser repetition rate)`
- `dw = detun*0.01;%multiwavelength filter(cavity mode filter)linewidth 50 MHz;`
- `dw1= dw*1;%Injection seed linewidth`
- `% Spectral filter %%`
- `dw2 = detun*20;% Filter width 8,25`
- `b1=7; %supergaussian factor`
- `env = 1.0*exp(-(i-m2)/dw2).^(2*b1));%spectral filter`
- `% Multiwavelength filter(cavity mode filter)`
- `%%%`
- `mn=41;%Mode number`
- `A=1/pi;`
- `WF1=A.*0.5*dw./((i-m2).^2+(0.5*dw).^2); %filter function (Lorentzian)`
- `for p = 1:(mn-1)/2`
- `WF1=WF1+A.*0.5*dw./((i-m2-p*detun).^2+(0.5*dw).^2)+...`
- `A.*0.5*dw./((i-m2+p*detun).^2+(0.5*dw).^2);`
- `end`
- `WF=WF1/max(WF1);`
- `% ASE noise (Initial Input)`
- `%%%`
- `ASE=rand(1,m);`
- `Ew = env.*ASE;`
- `Iw = Ew.*conj(Ew);`
- `Et1 = fftshift(fft(Ew)); % Input Field in time domain (FFT)`
- `It1 = Et1.*conj(Et1);`
- `figure(1)`
- `subplot(221),plot(i,Iw,i,env),axis([m2-200 m2+200 0 1])`
- `subplot(222),plot(i,log10(Iw),i,log10(env.^2)),axis([m2-200 m2+200 -15 5])`
- `% Time filter %%`
- `det=204.8;%period(=200/tinc)~200 ps; considering tinc=0.9765625 ps(~1ps)`
- `dt=15; % width ~ 25ps; 25,20`
- `b=1;%Supergaussian factor`
- `T2 = exp(-(i-m2)/dt).^(2*b))+...`
- `exp(-(i-m2-det)/dt).^(2*b))+exp(-(i-m2+det)/dt).^(2*b))+...`

- $\exp(-((i-m2-2*\det)/dt).^(2*b))+\exp(-((i-m2+2*\det)/dt).^(2*b));$
- figure(2)
- subplot(221),plot(i,T2),axis tight
- subplot(222),plot(i,WF,i,env),axis([m2-200 m2+200 0 1])
- subplot(222),plot(i,WF.\*env),axis([m2-200 m2+200 0 1])
- subplot(224),plot(i,WF),axis([m2-25 m2+25 0 1])
- %Parameters
- %Amplifier %%
- s1=0.00026; %Gain Saturation Parameter
- g=2.8;% Small Signal Gain Coefficient
- % Phenomenological Self phase modulation constant
- n\_spm =0.0032;%SPM coefficient
- 
- %SA %%
- s2=0.0012;%SA Saturation Parameter
- L=-1.9;%Absorption Coefficient
- 
- %GVD %%
- k1=1.2e-3;%GVD parameter
- k2=1.2e-3;
- 
- %Linear loss %%
- L1 = 0.2; %
- 
- %Linear phase %delay%%%
- Lpd =-0.09e-3; %
- 
- n = 50; %Loop iterations 100
- %Array allocation
- EwM=zeros(n,m); %initialize evolution matrices
- EtM=zeros(n,m);
- 
- %%
- %%
- for J = 1:n
- 
- %SG&SPM %%
- wg(1)=0;
- SG(1)=sqrt(exp(s1\*wg(1))/(exp(-g)-1+exp(s1\*wg(1))));
- for k = 1:m-1 %Integration of the pulse intensity for saturable gain and SPM
- wg(k+1) = wg(k) + It1(k);
- SG(k+1) = sqrt(exp(s1\*wg(k))/(exp(-g)-1+exp(s1\*wg(k))));
- end
- SPM = exp(j\*n\_spm\*wg); %Self phase modulation vector
- Et2 = Et1.\*SG.\*SPM; %apply saturable gain, spm
- Ew2 = ifft(fftshift(Et2)); %preshift for transform back to frequency domain
-

- %GVD1&LD1&WF  
%%%
- $GVD1 = \exp(j*k1*(i-(m+1)/2).^2);$
- $LD1 = \exp(j*Lpd*(i-(m+1)/2));$  %Linear phase delay
- $Ew3 = Ew2.*GVD1.*env.*WF.*LD1;$  %apply GVD,spectral filter, Wavelength filter,LPD
- $Et3 = \text{fftshift}(\text{fft}(Ew3));$  %shift again into temporal domain
- $It3 = Et3.*\text{conj}(Et3);$
- 
- %SA&L1&T2 %%
- $ws(1)=0;$
- $SA(1) = \sqrt{\exp(s2*ws(1))/(\exp(-L)-1+\exp(s2*ws(1)))};$
- for k = 1:m-1 %Integration of the pulse intensity for saturable absorber
- $ws(k+1) = ws(k) + It3(k);$
- $SA(k+1) = \sqrt{\exp(s2*ws(k))/(\exp(-L)-1+\exp(s2*ws(k)))};$
- end
- 
- $Et4 = Et3.*SA.*(1-L1).*T2;$  %Apply saturable absorption and linear loss
- $Ew4 = \text{ifft}(\text{fftshift}(Et4));$
- 
- %GVD2&LD2&WF  
%%%
- $GVD2 = \exp(j*k2*(i-(m+1)/2).^2);$
- $LD2 = \exp(j*Lpd*(i-(m+1)/2));$
- $Ew5 = Ew4.*GVD2.*env.*WF.*LD2;$  %+IJS;
- $Et5 = \text{fftshift}(\text{fft}(Ew5));$  %shift again into temporal domain
- $Iw5 = Ew5.*\text{conj}(Ew5);$
- $It5 = Et5.*\text{conj}(Et5);$
- 
- %Initialization %%
- $Et1=Et5;$
- $It1=Et1.*\text{conj}(Et1);$
- 
- $EwM(J,:)=Ew5;$  %record vectors into evolution matrices
- $EtM(J,:)=Et5;$
- 
- end %J-loof ends
- %%
- %%
- $Iwf = Ew5.*\text{conj}(Ew5);$
- $Itf = Et5.*\text{conj}(Et5);$  %pulse intensity for material response
- 
- for k=1:m
- $z(k)=\text{angle}(Et5(k).*(-1).^k);$
- end
- 
- %Plot %%
- $x=\text{linspace}(0,n,m);$
- $y=\text{linspace}(1,m,m);$
- $[X Y]=\text{meshgrid}(x,y);$
- 
- $IwM=EwM.*\text{conj}(EwM);$

- `ItM=EtM.*conj(EtM);`
- `Z1=IwM/max(Iwf);`
- `Z2=ItM/max(Itf);`
- `figure(3)`
- `subplot(221),mesh(Z1),axis tight`
- `subplot(222),contour(Z1,50),axis tight,axis([m2-100 m2+100 0 n 0 100]),view([0 0 1])`
- `subplot(223),plot(i,Iwf/max(Iwf)),axis([m2-100 m2+100 0 1])`
- `subplot(224),plot(i,log10(Iwf/max(Iwf))),axis([m2-100 m2+100 -15 1])`
- `figure(4)`
- `subplot(221),contour(Z2,50),axis tight,axis([m2-100 m2+100 0 n 0 100]),view([0 0 1])`
- `subplot(222),plot(i,ItM(n,:)/max(ItM(n,:)),i,T2),axis tight`
- `subplot(223),plot(i,Itf/max(Itf)),axis([m2-100 m2+100 0 1])`
- `subplot(224),plot(i,z),axis([m2-102 m2+102 -5 5])`
- `%Program End`

## **APPENDIX B: LASER FREQUENCY STABILIZATION BY POLARIZATION SPECTROSCOPY**



Frequency drifting of an optical comb source with respect to a WDM filter frequency window causes an additional relative intensity noise (RIN) which can be possibly transferred successively into the data at the receiver station. To avoid this problem, it is very necessary to

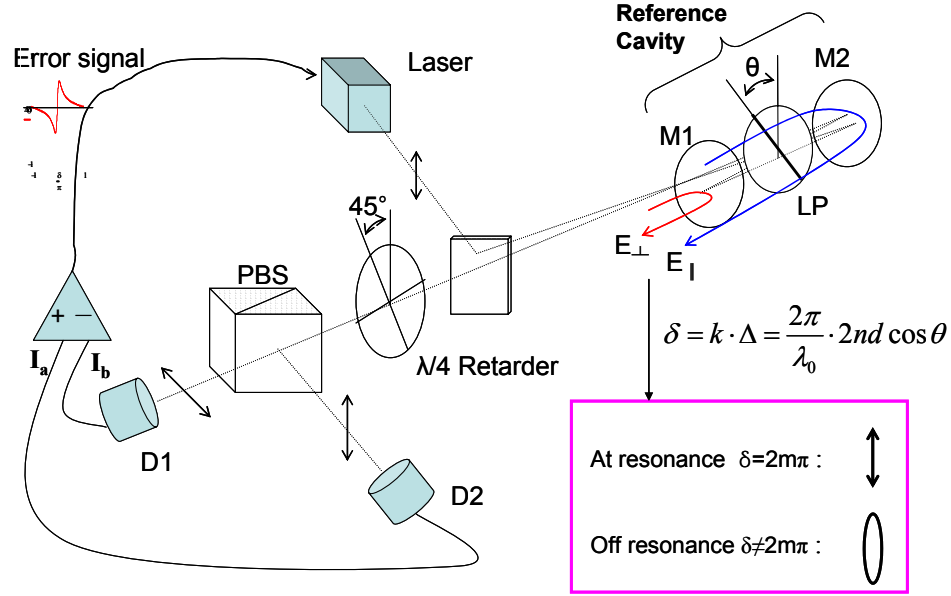
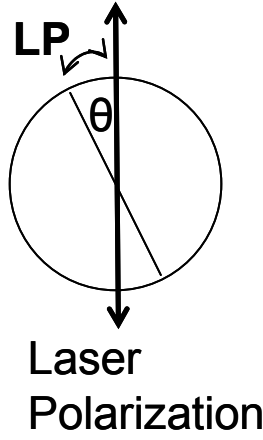
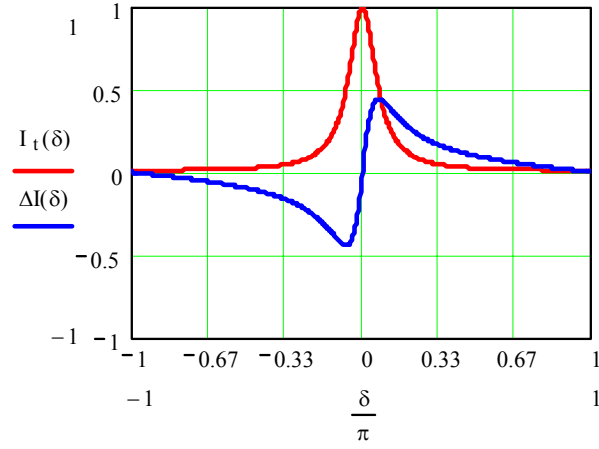


Figure 57: Schematic of laser frequency stabilization by polarization spectroscopy

stabilize optical frequencies of the comb source as much as needed for practical applications. Among several useful methods of laser frequency stabilization, a polarization analysis technique has recently shown promising potential of the successful adaptation to several practical laser systems [64]-[66]. In this method shown in Figure 55, the linear polarized output of the laser is sent to a reference cavity. The linear polarizer inside the cavity is rotated so that its transmission axis forms an angle  $\theta$  with the polarization axis of the incident beam. The incoming light can be



(a)



(b)

Figure 58: Theoretical response of a reference cavity (a) the angle  $\theta$  (b) the error signal

decomposed into two orthogonal linearly polarized components with the electric field vector parallel and perpendicular to the transmission axis of the intracavity polarizer. The parallel component sees a cavity of low loss and experiences a frequency-dependent phase shift in reflection of mirror m2. On the other hand, the perpendicular component simply reflected by mirror m1, serves as a reference. Any relative phase change between the two reflected components will make the resulting beam elliptically polarized. The  $\lambda/4$  retarder and a linear polarization beam splitter analyze the signal

$$\Delta I = I_a - I_b = I^{(i)} 2 \cos \theta \sin \theta \frac{T_1 R \sin(\delta)}{(1 - R)^2 + 4R \sin^2(\frac{1}{2} \delta)}$$

Where, the  $I^{(i)}$  is input beam intensity, the  $\delta$  is the phase of the beam as defined in Figure 55. The error signal  $\Delta I$  depends on the magnitude and handedness of the ellipticity, but not on the azimuth angle. For  $\theta = 45^\circ$ , theoretically calculated error signal is shown in Figure 56 (b). The obtained error signal can be used to control the driving current for the laser system via a servo electronic system. To improve overall performance of coherent heterodyne systems introduced here, the polarization analysis technique of laser stabilization scheme could be used for future research.

## **APPENDIX C: LONG-WAVELENGTH TWO-SECTION MONOLITHIC MSL FABRICATION**

### C.1 Laser Diode Fabrication Steps

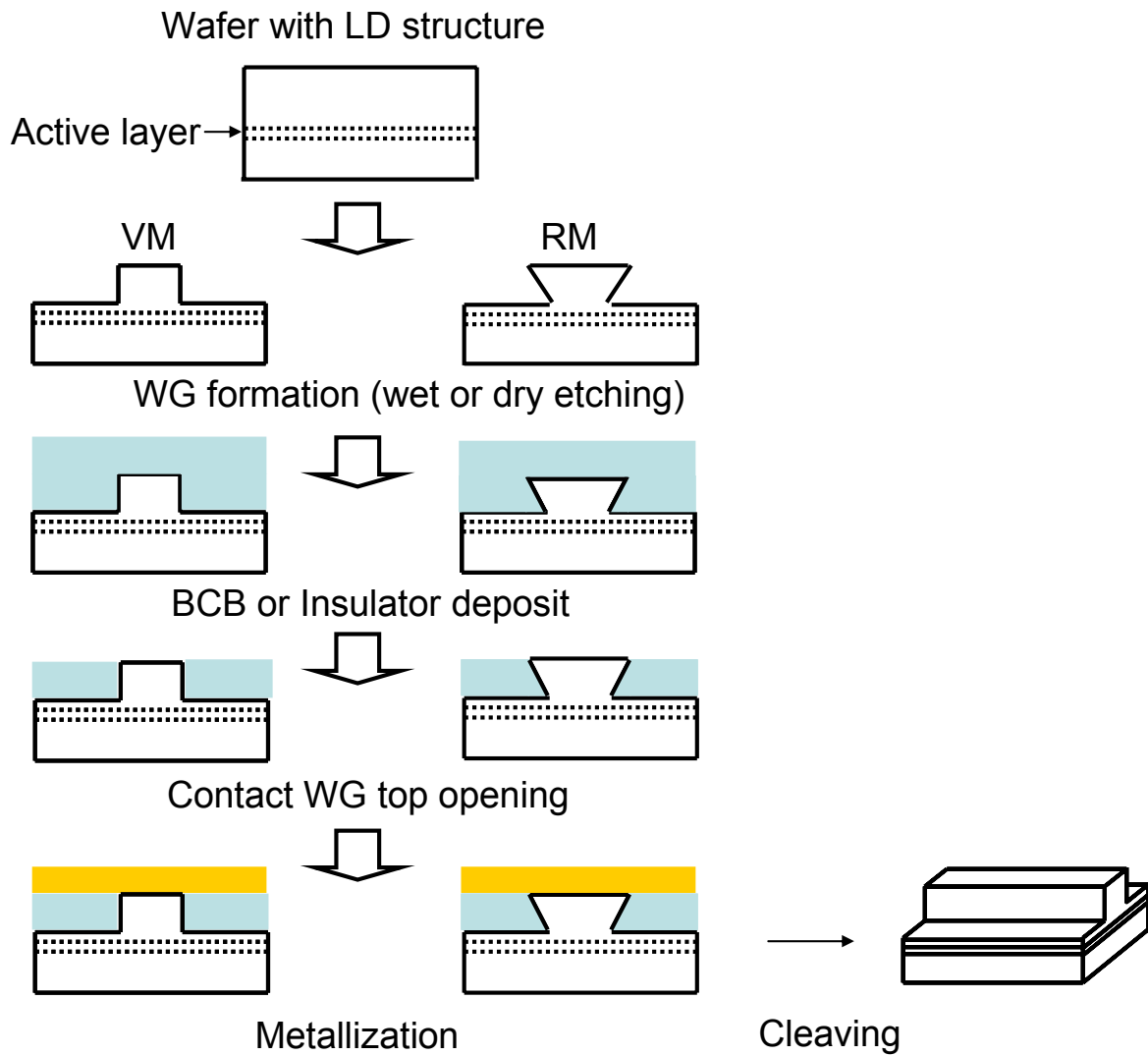


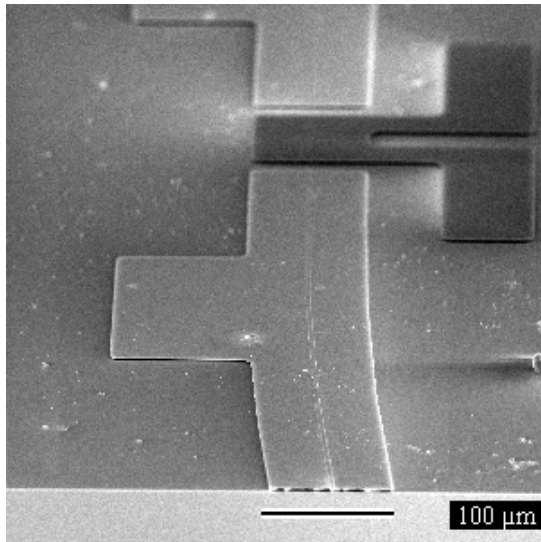
Figure 59: Schematic diagram of the Ridge Waveguide Laser Diode (RWLD) fabrication steps

(VM: vertical mesa, RM: reverse mesa)

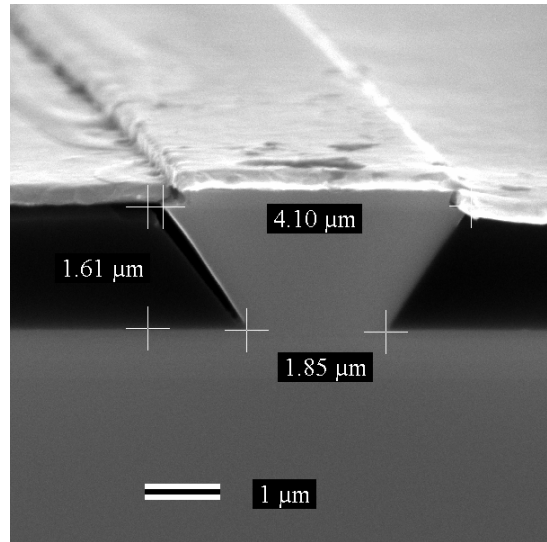
## **C.2 Device Characteristics**

One of the biggest advantages of a MSL system is the ability to be integrated with other subsystem components on a single platform. A monolithically integrated optical heterodyne receiver based on optical injection-locking techniques is appealing for deployment of coherent lightwave technology. For the purpose of developing a high quality monolithic MSL chip, device fabrication is being continued.

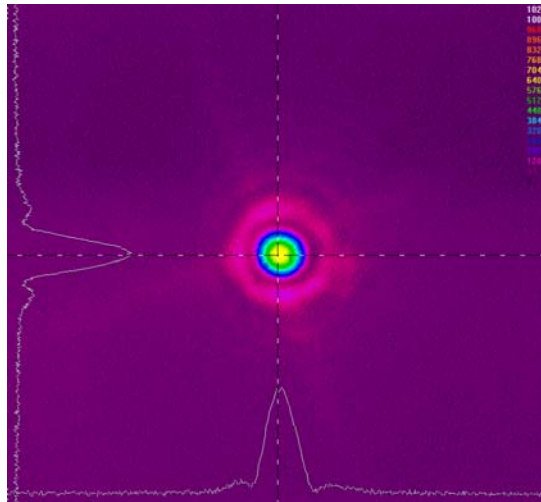
Figure 57 shows the fabrication steps of the ridge waveguide laser diodes. So far, a reverse mesa ridge waveguide laser diode (RM-RWLD) has been developed. As shown in Figure 58, 59, and 60 general performance of the device has shown a high quality single mode beam profile, reasonable output power, stable current-voltage characteristic, low threshold, and high frequency RF performance of the electroabsorption modulator in saturable absorber section of the device, was very good. However, there are few things to be improved to obtain the quality of modelocking performance such as undesirable modulation effect due to residual facet reflectivity on the gain section and effective discontinuity at the boundary between the sections as shown in Figure 61. When using an external cavity configuration it is desirable to have high reflectivity at the output facet of the semi-conductor laser while maintaining very low reflectivity at its inner facet to couple to the external cavity. With imperfect antireflection coatings at this facet, multiple pulses are generated at the semiconductor laser roundtrip frequency. These additional pulses are undesirable for most applications, and also deplete the power of the primary pulse. An inner facet reflectivity of  $10^{-4}$  is often quoted as a minimum value for satisfactory mode locking operation, but facet reflectivities of the order of  $10^{-6}$  are needed to more completely suppress the formation of subpulses [67].



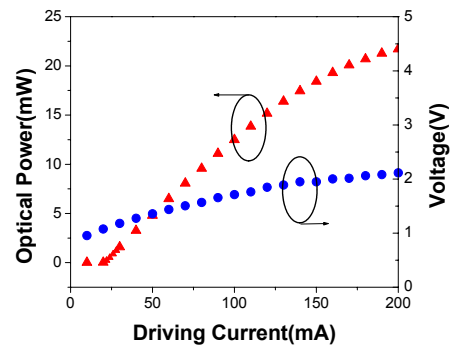
(a) Overall view



(b) Facet View

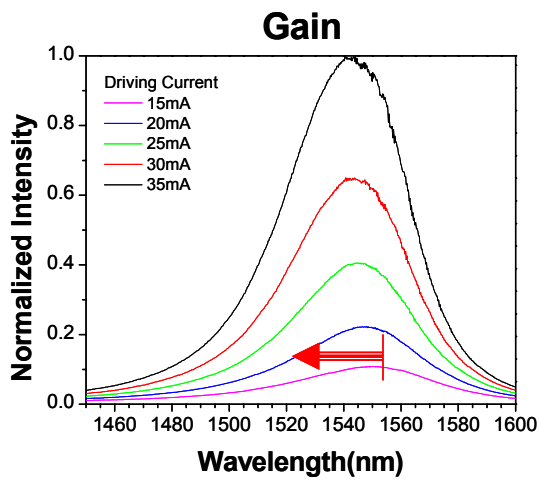


(c) Beam Profile from ball lens coupling

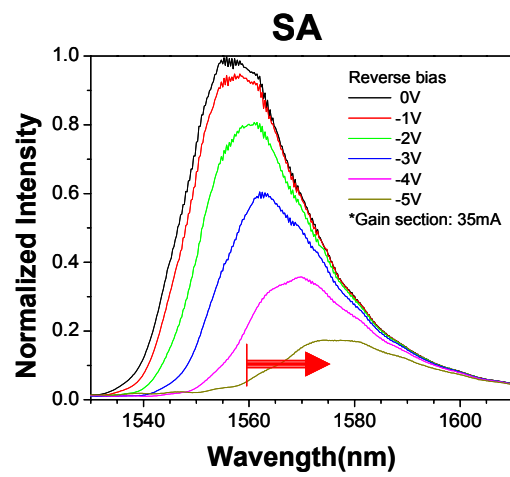


(d) L-I & I-V Characteristic

Figure 60: Reverse Mesa Ridge Waveguide Laser Diode (RM-RWLD)



(a) gain growing



(b) absorption band edge shift

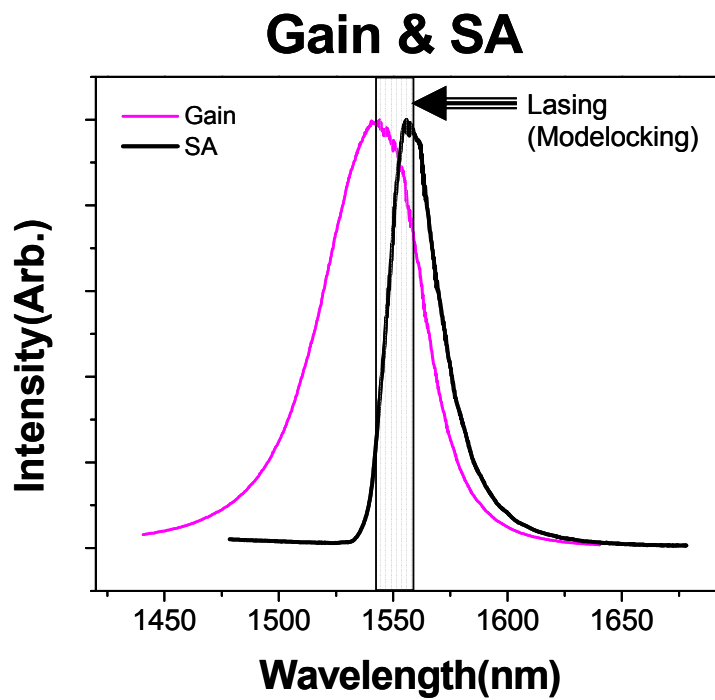
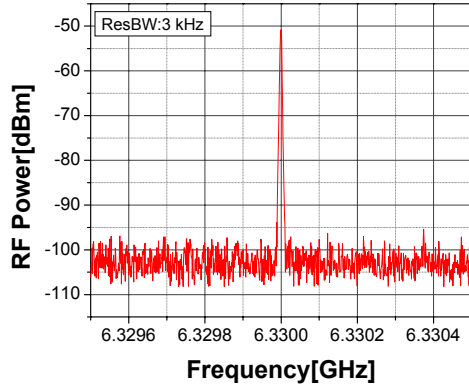
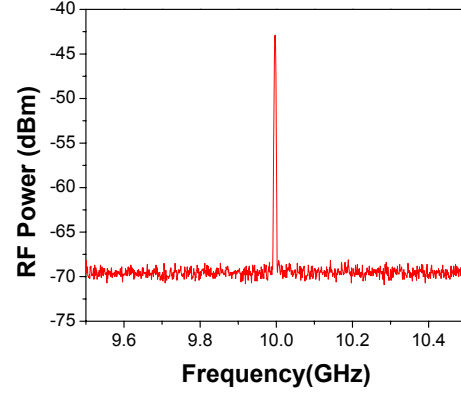


Figure 61: Gain growth and Absorption band edge shift



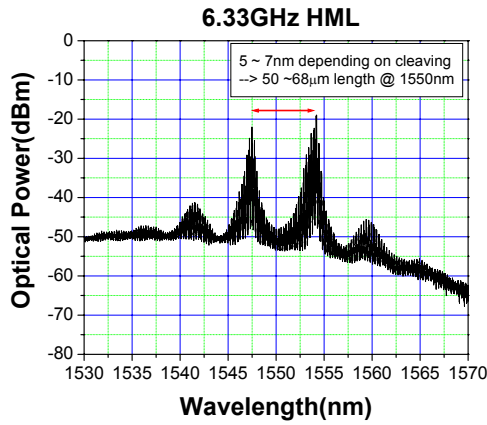


(a)

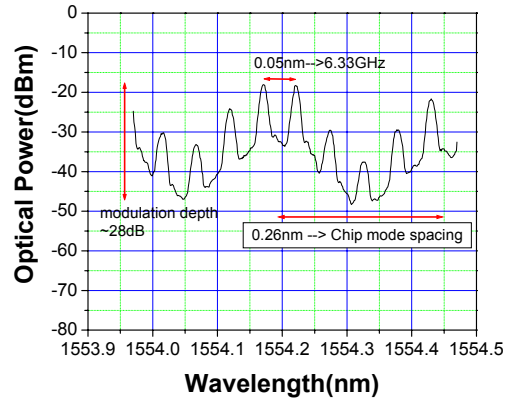


(b)

Figure 62: RF performance of the RM-RWLD (a) External Cavity Hybridly Modelocked at 6.33GHz (b) 10 GHz modulated carrier by the electroabsorption modulator



(a)



(b)

Figure 63: Optical spectra of 6.33GHz hybridly modelocked external cavity RM-RWLD (a) undesirable modulation due to discontinuity effect (b) Undesirable modulation due to poor AR coating

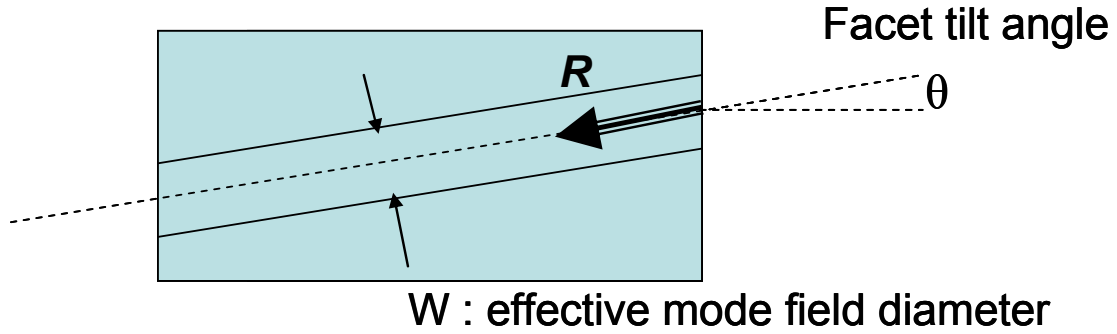


Figure 64: Angled waveguide

Semiconductor optical amplifiers with angled facets, as shown in Figure 62 have a reduced reflectivity due to the reduction in overlap between the reflected light and the guided mode, and have been mode locked in the past [68]. The effective facet reflectivity of the angled waveguide structures is given by [69]

$$R = R_f e^{-(\pi \cdot n \cdot W \cdot \theta / \lambda)^2}$$

where  $R_f$  is the reflectivity of the uncoated device facet,  $n$  is the refractive index of the waveguide core,  $W$  is the mode field diameter,  $\theta$  is the wave guide tilt angle with respect to the facet normal. Figure 63 shows the effective facet reflectivity of the angled waveguide structure. 4 micron mode field diameter gives us facet reflectivity of well below  $10^{-5}$ .

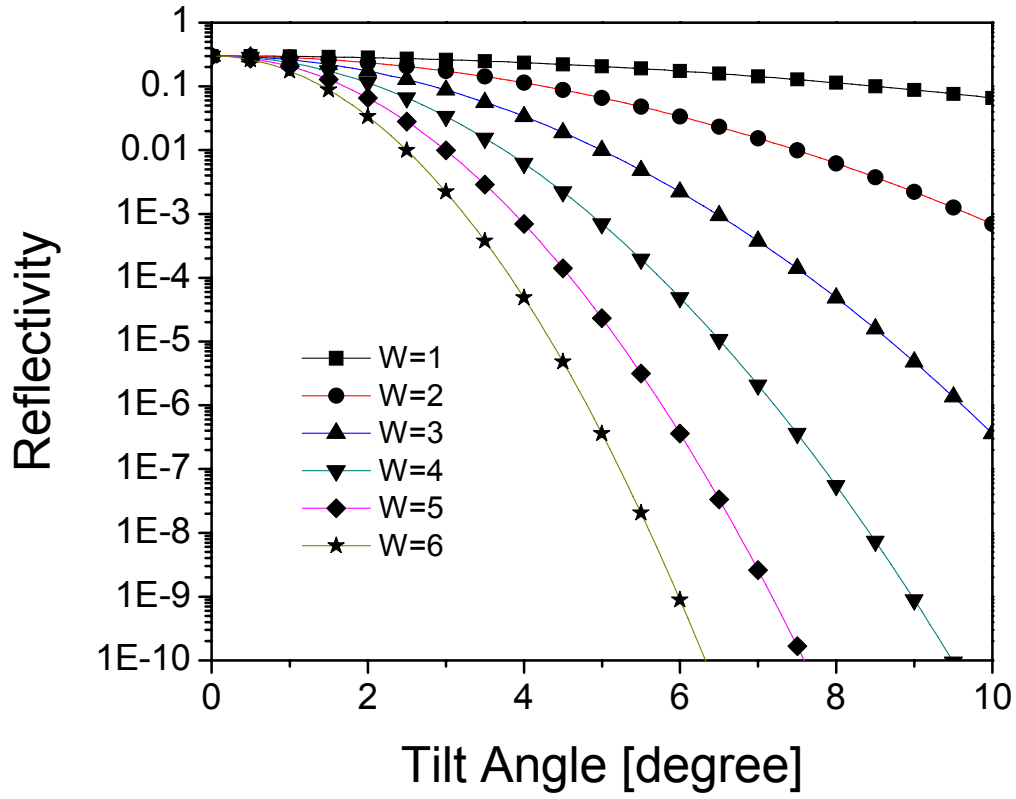


Figure 65: Effective facet reflectivity of angled waveguide

Nevertheless, strong single mode field confinement in such a narrow-neck RM-RWLD overwhelmed the angled facet effect. To solve this problem, the mask pattern of the RM-RWLD has been modified in order to eliminate the detrimental modulation effect from the facet on the gain side and the discontinuity at the boundary between the sections as shown in Figure 64. Further fabrication work with this design will improve overall performance much better.

### C.3 Improved Design

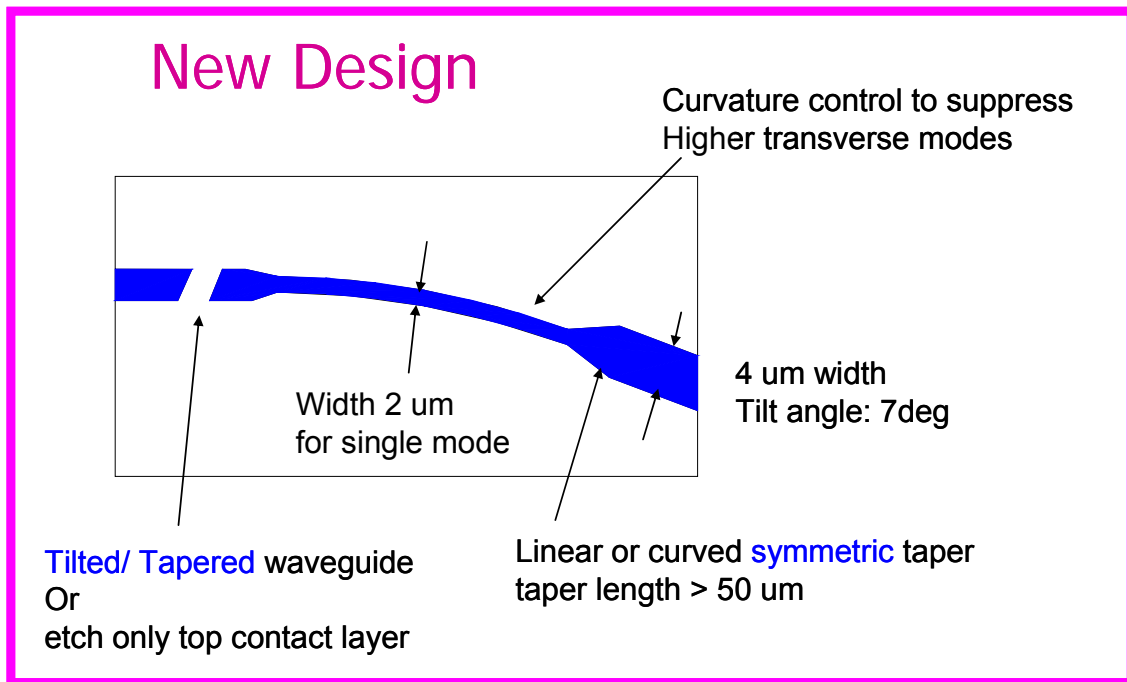


Figure 66: Mask design for the improved RM-RWLD

## C.4 Metallic Pad Design for the High-speed MSL

### Metallic Pad Design Layout 1

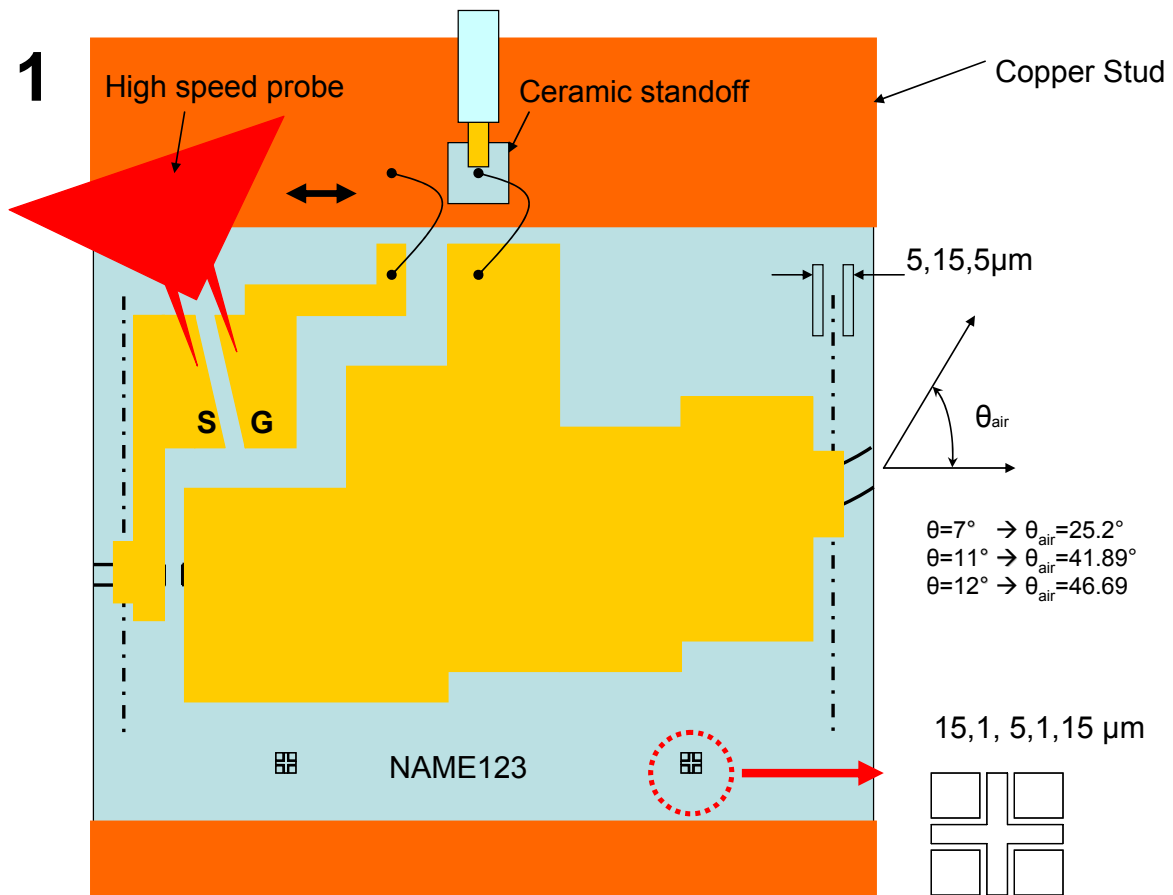


Figure 67: Metallic pad design 1 (S: signal, G: ground)

## Metallic Pad Design Layout 2

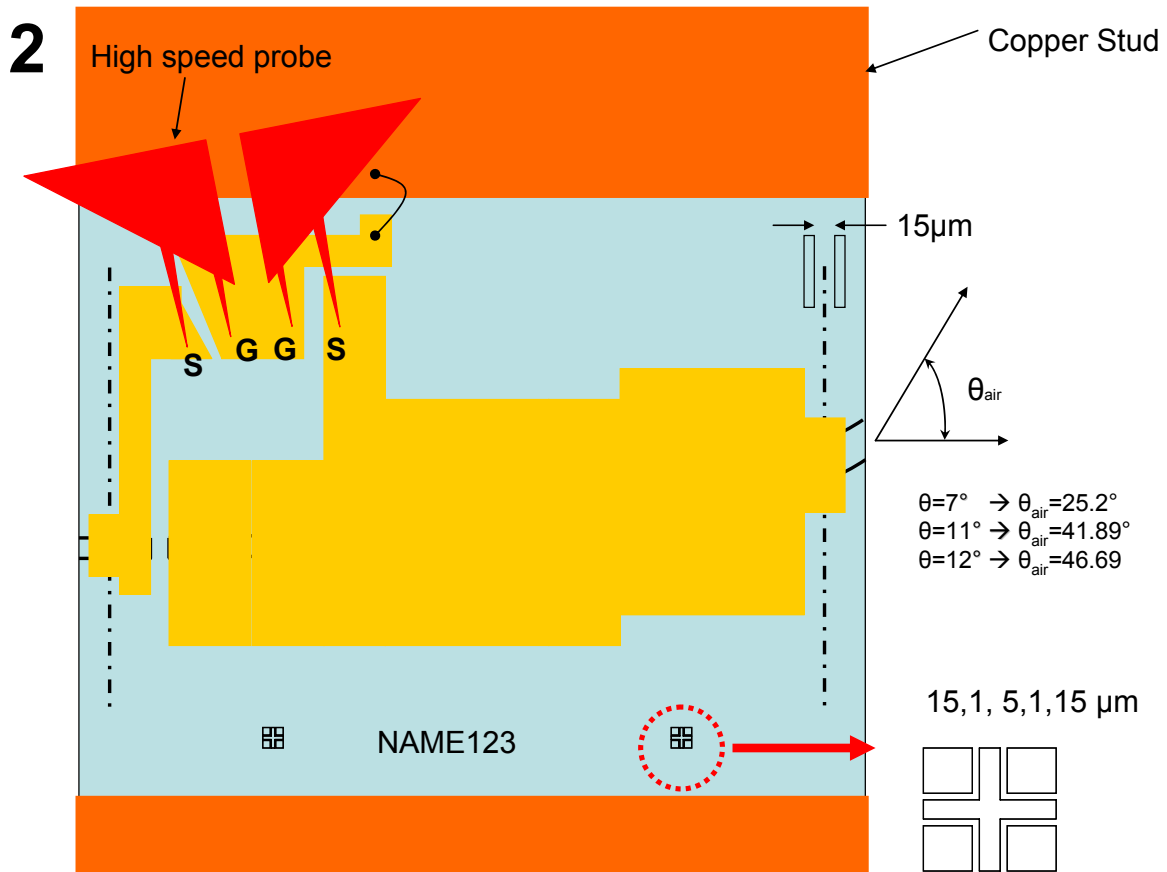


Figure 68: Metallic pad design 2

## **APPENDIX D: SEMICONDUCTOR OPTICAL AMPLIFIER DEVICE CHARACTERISTICS AND MISCELLANEOUS SYSTEM ELEMENTS**

### D.1 Two-Section SOA Characteristics

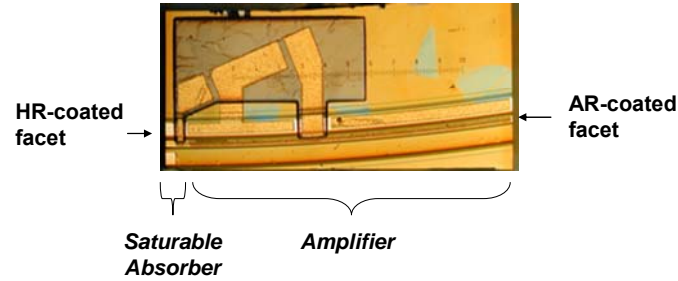
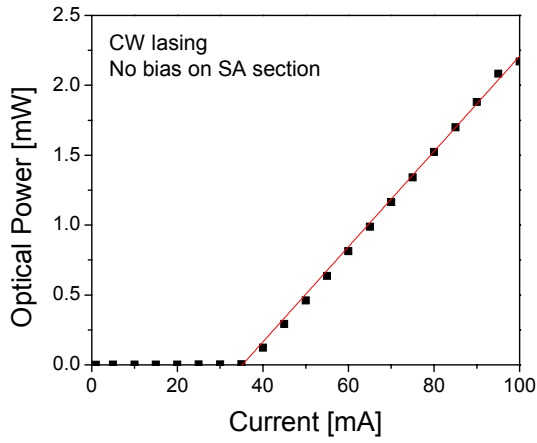


Figure 69: Picture of the 1550 nm two-section SOA

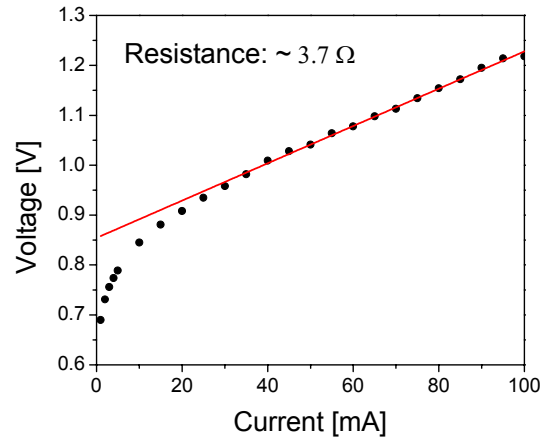
The two-section SOA device picture is shown in Figure 67. The device length is 1.5 mm with a 50  $\mu\text{m}$  electro-absorption modulator which can work as a saturable absorber (SA). The separation between the gain and SA section is  $\sim 10 \mu\text{m}$ . The metal pad of the device was designed as a high-speed top-driven configuration. The electrical resistance across the two sections is kOhm. The active region of the device is made of InGaAsP multiple quantum well (MQW). However, the device wafer structure is not publicly known. Through a simple DC probe test, the ASE power from the AR-coated facet was measured to be  $\sim 1 \text{ mW}$  at a forward bias current of 100 mA. The peak wavelength of the ASE spectrum was centered at  $\sim 1555 \text{ nm}$ . The gain bandwidth of the device fully covers entire optical C band (1525 -1565 nm).

Figure 68 shows LI (light output vs. current)-VI (bias voltage vs. current) characteristics of the two-section SOA. The LI-curve is measure of CW lasing based on the grating-coupled PF laser configuration using a groove density of 600 lines/mm. In this LI measurement, the SA-section of the device is not biased. The measured VI curve shows the linear slope of 3.7 Ohm. Figure 69 (a) and (b) show tunable wavelength range of the grating-coupled laser.



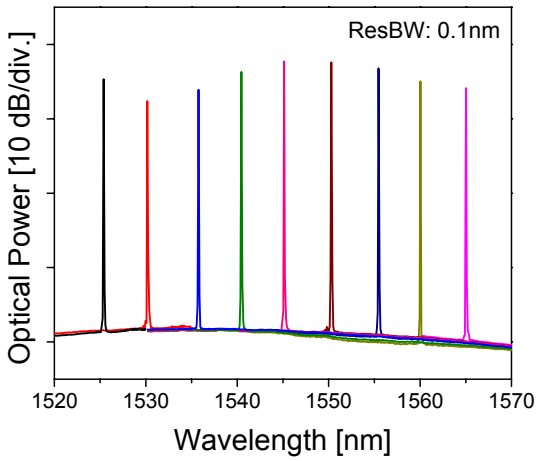


(a) LI curve

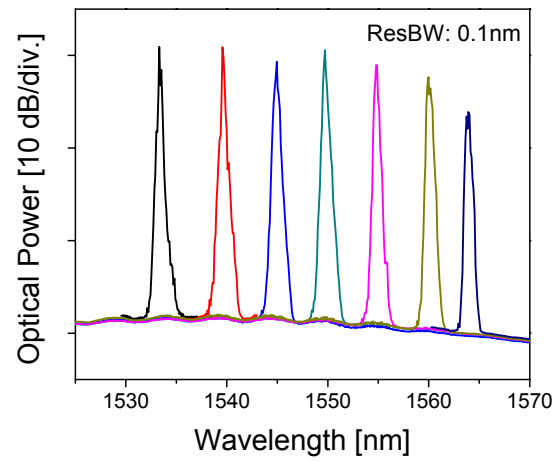


(b) VI curve

Figure 70: LI (light output vs. current)-VI (bias voltage vs. current) characteristics of the two-section SOA

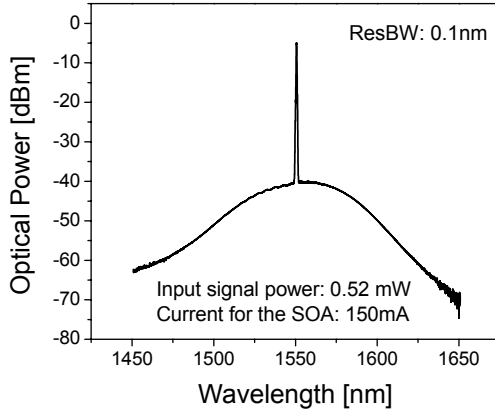


(a) CW lasing

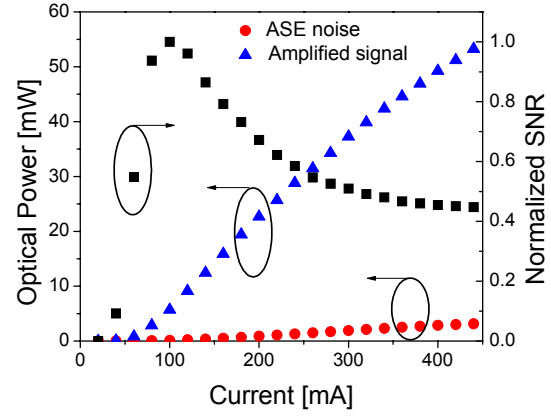


(b) Hybrid Modelocking (10 GHz)

Figure 71: Wavelength tuning range of the grating-coupled laser in CW lasing (a) and hybrid modelocking (b)



(a) Optical spectrum



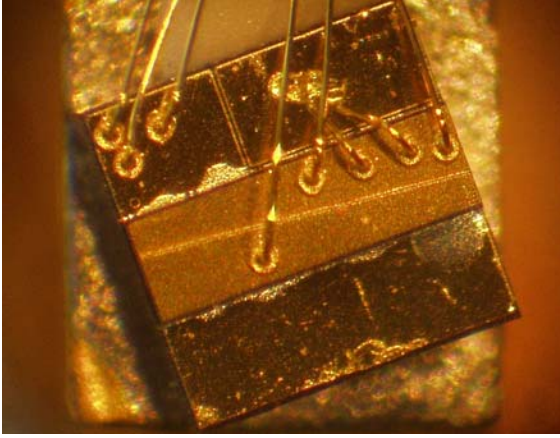
(b) Output power and SNR

Figure 72: Optical spectrum, output power, and SNR of the amplified 6.33 GHz hybridly modelocked grating-coupled laser.

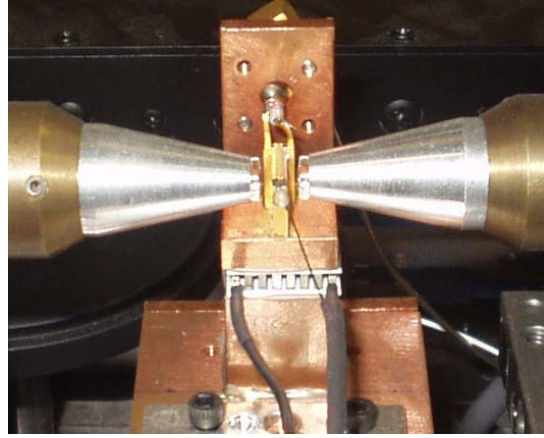
The CW lasing and modelocked spectrum nearly covers the entire optical C band. Figure 70 (a) and (b) show the optical spectrum of the amplified grating-coupled laser. In this case, the laser was hybridly modelocked at 6.33 GHz with a dc current of 69 mA on the gain section as well as a combined a rf power of  $\sim 20$  dBm at 6.33 GHz and a dc bias of - 3.2V on the SA section. The additional external amplifier was a 2 mm Covega SOA. The details of the Covega SOA is described in the following section. The input laser signal power to the Covega SOA was 0.52 mW. After amplification, maximum average output power of more than 50 mW was obtained.

## D.2 Covega SOA Characteristics

The device wafer structure is not publicly known. The device length is 2 mm. General characteristics of the device are described in the following.



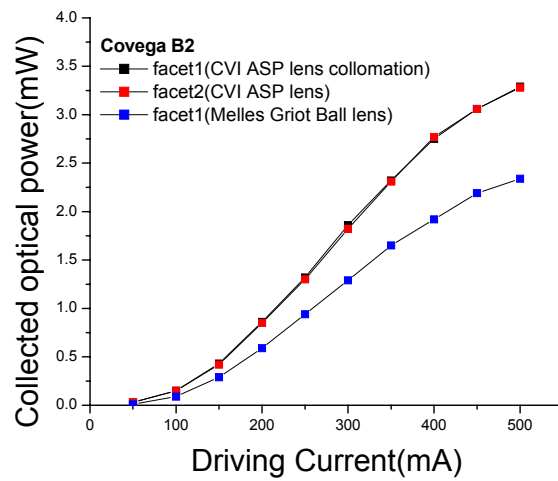
(a) angled-facet booster Covega SOA



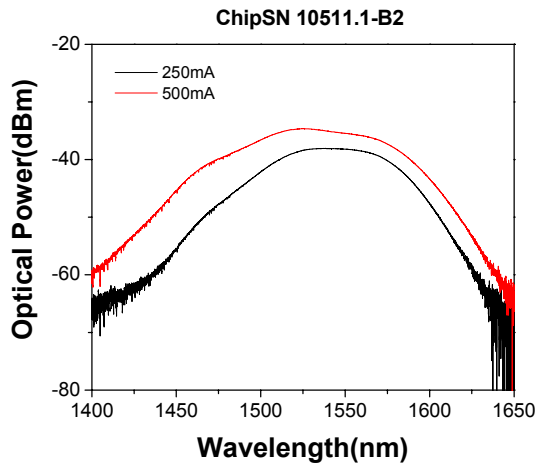
(b) light collimation mount

Figure 73: Picture of the 1550 nm commercial Covega SOA and home-made device mount

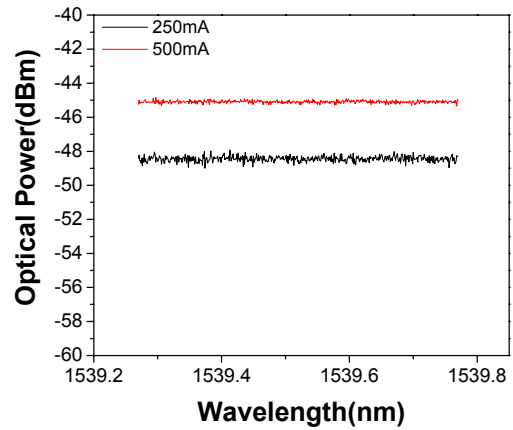
- $I(P_{max})@25C$ : 490 mA
- $V(P_{max})@25C$ : 1.21 V  $\rightarrow$  1.5 Ohm
- ASE- $P_{max}@25C$ : 2.54 mW
- Small signal gain G: 18 dB
- Saturation Power(3dB): 18 dBm



(a) L-I Curve



(b) ASE Gain



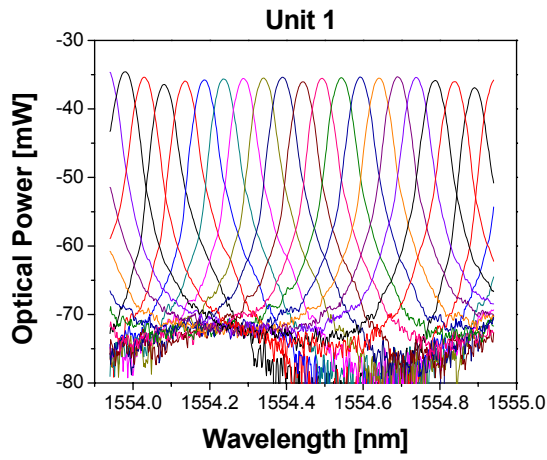
(c) Ripple on the Gain (Good AR coating)

Figure 74: Covega SOA characteristics

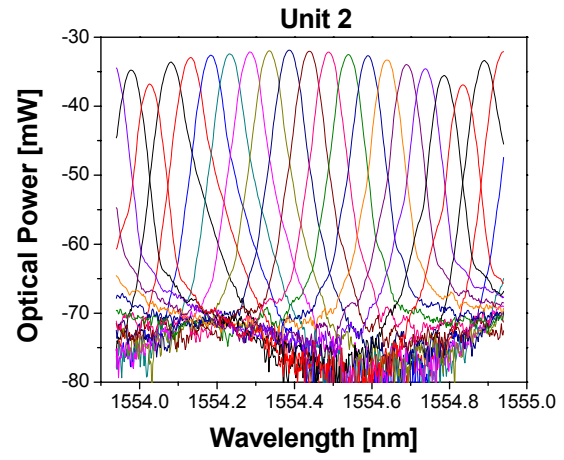
### D.3 Essex Hyperfine WDM

#### Specification

- Channel: 16
- Optical window: C band (centered 1555 nm)
- Spacing: 6.33 GHz
- Free spectral range: 100 GHz
- Insertion loss: 5 dB (center) ~ 8 dB (edge)
- Cross talk: ~ 15 dB
- PMD: < 1 ps



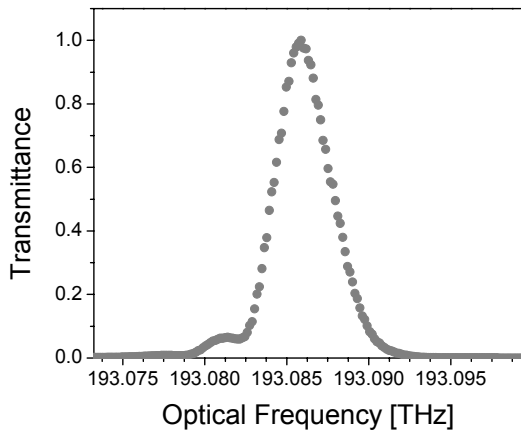
(a)



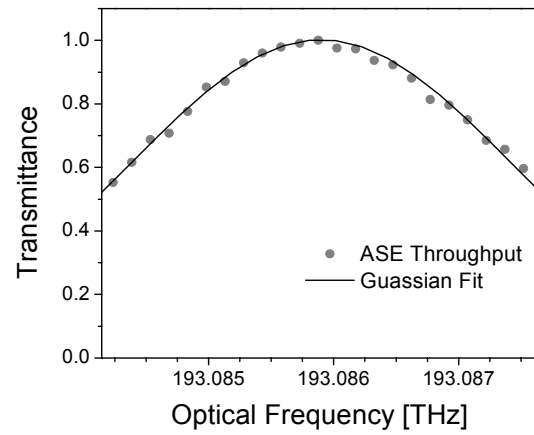
(b)

Figure 75: Essex hyperfine filter transfer function (a) unit1 (b) unit2.

### Filter Shape Function



(a)



(b)

Figure 76: Essex hyperfine filter shape function measurement (a) ASE throughput of a single channel window (b) Zoom-in filter shape.

## D.4 Grating Filter

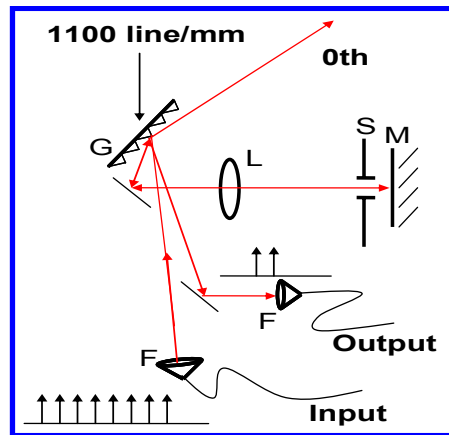


Figure 77: Schematic of the grating filter (G: grating, L: lens, S: slit, M: mirror, F: fiber launcher)

### Filter Passband Width

**grating groove density G**      $G := \frac{1100}{10^6} \frac{\text{grooves}}{\text{nm}}$

**grating period p (mm/grooves)**      $p := \frac{1}{G} \frac{\text{nm}}{\text{grooves}}$       $\lambda := 1555 \text{ nm}$       $c := 3 \cdot 10^8 \cdot 10^9 \frac{\text{nm}}{\text{sec}}$

**diffraction order**      $m := 1$

$\alpha := \frac{\pi}{3.6} \quad \alpha \cdot \frac{180}{\pi} = 50$

$\beta := \text{asin}\left(\frac{m\lambda}{p} - \sin(\alpha)\right) \quad \beta = 1.236 \quad \beta \cdot \frac{180}{\pi} = 70.814$

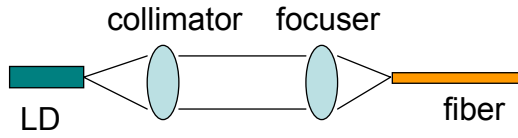
**effective focal length**      $f := 200 \text{ mm}$

**exit slit width**      $w := 0.45 \text{ mm}$

**Passband width**      $\Delta\lambda := \frac{p \cdot \cos(\beta)}{f \cdot m} \cdot w \text{ nm} \quad \Delta\lambda = 0.672 \text{ nm}$

$\Delta\nu := \frac{c}{\lambda^2} \Delta\lambda \quad \Delta\nu = 8.34 \times 10^{10} \text{ Hz} \quad \text{less than 100GHz}$

## D.5 Fiber Coupling System



\*LD: angle stripe (6deg tilt)

\*Fiber: FC-APC

\*Collimator, focuser : CVI Aspheric Lens, MG Ball Lens, Newport Fiber Launcher

	NA	EFL[mm]	BFD[mm]	Aperture[mm]	Outer Dia.[mm]
CVI Asp. Lens	0.67	2.84	1.76	4	5.4
Melles Griot ball lens	0.19		0.29	4	5

	Coupled Power (mW)	Collected Power (mW)	%
ball to ball	5.53	13.83	40
ball to fiber launcher	2.34	11.7	20
Asp. To fiber launcher	6.28	16	39.25
<b>Asp. To ball</b>	<b>12</b>	<b>16</b>	<b>&gt;75</b>
Asp. To Asp.	5.5	15	37

\*Asp: Aspheric lens

\*Ball: ball lens

## LIST OF REFERENCES

- [1] P. Y. Takushima and K. Kikuchi, "10-GHz, over 20-channel multiwavelength pulse source by slicing super-continuum spectrum generated in normal-dispersion fiber," *IEEE Photon. Technol. Lett.*, vol. 11, pp. 322–324, Mar. 1999.
- [2] C. Silva and A. Seeds, "Terahertz span > 60-Channel exact frequency dense WDM source using comb generation and SG-DBR injection-locked laser filtering," *IEEE Photon. Technol. Lett.*, vol. 13, pp. 370–372, Apr. 2001.
- [3] M. Mielke, G. Alphonse, P. Delfyett, "168 channels x 6 GHz from a multiwavelength mode-locked semiconductor laser," *IEEE Photon. Technol. Lett.*, On page(s): 501-503, Volume: 15, Issue: 4, Apr 2003
- [4] P. Delfyett, S. Gee, M.-T. Choi, H. Izadpanah, W. Lee, S. Ozharar, F. Quinlan, and T. Yilmaz, "Optical frequency combs from semiconductor lasers and applications in ultrawideband signal processing and communications," *J. Lightwave Technol.*, vol. 24, pp. 2701 - 2719, 2006.
- [5] X. Shijun , A.M. Weiner, C. Lin, Experimental and theoretical study of hyperfine WDM demultiplexer performance using the virtually imaged phased-array (VIPA)," *J. Lightw. Technol.*, vol. 23, pp. 1456 - 1467, 2005.
- [6] A. Agarwal, P. Toliver, R. enendez, S. Etemad, J. Jackel, J. Young, T. Banwell, B. Little, S. Chu, W. Chen, W. Chen, J. Hryniewicz, F. Johnson, D. Gill, O. King, R. Davidson, K. Donovan, and P. Delfyett, "Fully programmable ring-resonator-based integrated photonic circuit for phase coherent applications," *J. of Lightw. Technol.*, vol. 24, pp 77-86, 2006.
- [7] W. Lee and P.J. Delfyett, Jr, "Dual-mode injection locking of two independent modelocked semiconductor lasers," *IEE, Electron. Lett.*, vol. 40, no. 19, pp. 1182-1183, 2004.
- [8] B. K. Mathason, and P. J. Delfyett, "Pulsed injection locking dynamics of passively mode-locked external-cavity semiconductor laser systems for all-optical clock recovery", *J. Lightw. Technol.*, vol. 18, no. 8, pp. 1111-1120., 2000.
- [9] F. Mogensen, H. Olesen, and G. Jacobsen, "Locking conditions and stability roperties for a semiconductor laser with external light injection," *IEEE J.Quantum Electron*, vol. QE-21, pp. 784-793, 1985.
- [10] K. Kikuchi, C.-E. Zah, and T.-P. Lee, "Amplitude-modulation sideband injection locking characteristics of semiconductor lasers and their application," *J. Lightw. Technol.*, vol. 6, no. 12, pp. 1821-1988, Aug. 1988.



- [11] Z. Ahmed, H. F. Liu, D. Novak, Y. Ogawa, M. D. Pelusi, and D. Y. Kim, "Locking characteristics of a passively mode-locked monolithic DBR laser stabilized by optical injection," *IEEE Photon. Technol. Lett.*, vol. 8, no. 1, pp. 37-39, Jan. 1996.
- [12] T. Jung, J. L. Shen, D. T. K. Tong, S. Murthy, M. C. Wu, T. Tanbun-Ek, W. Wang, R. Lodenkamper, R. Davis, L. J. Lembo, and J. C. Brock, "CW injection locking of a mode-locked semiconductor laser as a local oscillator comb for channelizing broad-band RF signals," *IEEE Trans. Microwave Theory Tech.*, vol. 47, pp. 1225-1233, July 1999.
- [13] W. Lee, M. Mielke, S. Etemad, and P. Delfyett, "Subgigahertz channel filtering by optical heterodyne detection using a single axial mode from an injection locked passively modelocked semiconductor laser," *IEEE Photon. Technol. Lett.*, vol. 16, no. 8, pp. 1945-1947, Aug. 2004.
- [14] M. Ogusu, K. Inagaki, and Y. Mizuguchi, "60 GHz millimeter-wave source using two-mode injection-locking of a Fabry-Perot slave laser," *IEEE Microwave and Wireless Components Lett.*, vol. 11, no. 3, pp. 101-103, Mar. 2001.
- [15] H. Yokoyama, "Highly reliable mode-locked semiconductor lasers," *IEICE Trans. Electron.*, vol. E85-C, no. 1, pp. 27-36, 2002.
- [16] H. Kurita, I. Ogura, H. Yokoyama, "Ultrafast all-optical signal processing with mode-locked semiconductor lasers," *IEICE Trans. Electron.*, vol. E81-C, no. 2, pp. 129-139, 1998.
- [17] B. Mathason, H. Shi, I. Nitta, G. Alphonse, J. Abeles, J. Connolly, P. J. Delfyett, "Multiwavelength all-optical TDM switching using a semiconductor optical amplifier in a loop mirror," *IEEE Photonics Technol. Lett.* vol. 11, no. 3, pp. 331-333, 1999.
- [18] K. Sato, I. Kotaka, Y. Kondo, and M. Yamamoto, "High-repetition frequency pulse generation at over 40 GHz using mode-locked lasers integrated with electroabsorption modulators," *IEICE Trans. Electron.*, vol. E81-C, no. 2, pp. 146-150, 1998.
- [19] Y. K. Chen and M. C. Wu, "Monolithic colliding-pulse mode-locked quantum-well lasers," *IEEE J. Quantum Electron.*, vol. 28, pp. 2176-2185, 1992.
- [20] H. Shi, J. Finlay, G. Alphonse, J., and P. J. Delfyett, "Multiwavelength 10-GHz picosecond pulse generation from a single-stripe semiconductor diode laser," *IEEE Photonics Technol. Lett.* vol. 9, no. 11, pp. 1439-1441, 1997.
- [21] H. Shi, G. Alphonse, J. Connolly, and, P. J. Delfyett, "20x5 Gbit/s optical WDM transmitter using single-stripe multiwavelength modelocked semiconductor laser," *Electronics Lett.*, vol. 34, no. 2, pp. 179-181, 1998.
- [22] Mielke M, Delfyett PJ, Alphonse GA, "Suppression of mode partition noise in a multiwavelength semiconductor laser through hybrid mode locking," *Opt. Lett.*, vol. 27, no. 12, pp. 1064-1066, 2002.

- [23] Y. Ozeki, Y. Takushima, and K. Kikuchi, "Reduction of mode partition noise in mode-locked semiconductor lasers by using nonlinear optical loop mirror," European Conference on Optical Communication 2004, We 4. P. 097.
- [24] C. Lin and C. Juang, "Superluminescent diodes with bent waveguide," IEEE Photon. Technol. Lett., vol. 8, no. 2, pp. 206-208, Feb. 1996.
- [25] A. E. Siegman, Lasers, University Science Books; (January 1, 1986).
- [26] J.-C. Diels and W. Rudolph, Ultrashort Laser Pulse Phenomena, Academic Press;(1996).
- [27] I. N. Duling, III and M. L. Dennis, Compact Sources of Ultrashort Pulses. Cambridge, U.K.: Cambridge Univ. Press, 1995.
- [28] D. J. Jones, L.M. Zhang, J.E. Carroll, D. D Marcenac, "Dynamics of monolithic passively mode-locked semiconductor lasers," IEEE J. Quantum Electron., Vol. 31, pp1051 – 1058, 1995.
- [29] E. D. Black: 'An introduction to Pound–Drever–Hall laser frequency stabilization', Am. J. Phys., vol. 69, no. 1, pp.79-87, 2001.
- [30] T. Okoshi, K. Kikuchi, and A. Nakayama, "Novel method for high resolution measurement of laser output spectrum," Electron. Lett., vol.16, no. 16, pp.630-631, 1980.
- [31] S. Ryu, Coherent Lightwave Communication Systems, Artech house, 1995.
- [32] D. Derickson, Fiber Optic Test and Measurement, Prentice Hall PTR, 1998
- [33] Obarski, G.E., and Splett, J.D.: 'Transfer standard for the spectral density of relative intensity noise of optical fiber sources near 1550 nm', J. Opt. Soc. Am. B, 18 (6), 2001, pp.750-761.
- [34] Carrier noise test set manual HP11729C, Hewlett Packard, 1994.
- [35] P.J. Delfyett, S. Gee, M-T. Choi, H. Izadpanah, W. Lee, S. Ozharar, F. Quinlan, T. Yilmaz, "Optical Frequency Combs From Semiconductor Lasers and Applications in Ultrawideband Signal Processing and Communications," IEEE J. of Lightwave Technol., 24, pp 2701- 2719, 2006.
- [36] W. Lee, M-T. Choi, H. Izadpanah, P. J. Delfyett, and S. Etemad, "Coherent Homodyne Pulse Detection for a Spectral Phase-Encoded Optical CDMA System using Synchronized Modelocked Lasers," OAA/COTA 2006, OSA topical meetings, CFD6, June 30, 2006
- [37] P.T. Ho, 'Phase and Amplitude' Fluctuations in a Mode-Locked Laser', IEEE J. Quant. Electron., QE-21, 1806-1813, Nov. 1985.

- [38] Chen, Y.K., Wu, M.C., Tanbun-Ek, T., Logan, R.A., and Chin, M.A.: ‘Multicolor Single-Wavelength Sources generated by a Monolithic Colliding Pulse Mode-Locked Quantum well Laser’, *IEEE Photon. Technol. Lett.*, 3 (11), pp. 971-973, 1991.
- [39] A. Tomita, and A. Suzuki, “A new density matrix theory for semiconductor lasers, including non-Markovian intraband relaxation and its application to nonlinear gain,” *IEEE J. Quantum Electron.* 27, pp1630, 1991.
- [40] W. Lee, and P. J. Delfyett, “Dual mode injection locking of two independent modelocked semiconductor lasers,” *IEE Electronics Letters*, 40, No. 19, pp.1182- 1183, 2004.
- [41] M. R. Surette, D. R. Hjelme, and A. R. Mickelson, “An optically driven phased array antenna utilizing heterodyne techniques,” *J. Lightw. Technol.*, vol. 11, pp. 1500–1509, Sept. 1993.
- [42] K. Sun, E. K. Gustafson, M. M. Fejer, and R. L. Byer, “Polarization-based balanced heterodyne detection method in a Sagnac interferometer for precision phase measurement,” *Opt. Lett.*, vol. 22, no. 17, pp. 1359–1361, Sept. 1997.
- [43] T. Kuri and K. Kiayama, “Optical heterodyne detection for 60 GHz-band radio-on-fiber systems,” *J. Commun. Res. Lab.*, vol. 49, no. 1, pp. 45–56, 2002.
- [44] W. Wang, R. L. Davis, T. J. Jung, R. Lodenkamper, L. J. Lembo, J. C. Brock, and M. C. Wu, “Characterization of a coherent optical RF channelizer based on a diffraction grating,” *IEEE Trans. Microwave Theory Tech.*, vol. 49, pp. 1996-2001, Oct. 2001.
- [45] S. Galli, R. Menendez, P. Toliver, T. Banwell, J. Jackel, J. Young, and S. Etemad, “DWDM-compatible spectrally phase encoded optical CDMA,” in *Proc. IEEE Global Telecommunications (GLOBECOM)*, Dallas, TX, Nov. 2004, pp. 1888–1894.
- [46] V. J. Hernandez, Y. Du, W. Cong, R. P. Scott, K. Li, J. P. Heritage, Z. Ding, B. H. Kolner, and S. J. Yoo, “Spectral phase-encoded time-spreading (SPECTS) optical code-division multiple access for terabit optical access networks,” *J. Lightw. Technol.*, vol. 22, no. 11, pp. 2671-2679, Nov. 2004.
- [47] Z. Jiang, D. S. Seo, S. D. Yang, D. E. Leaird, A. M. Weiner, R. V. Roussev, C. Langrock, and M. M. Fejer, “Four user, 2.5 Gb/s, spectrally coded O-CDMA system demonstration using low power nonlinear processing,” in *2004 Optical Fiber Conf. (OFC 2004)*, Los Angeles, CA, 2004, Paper PDP29.
- [48] R. Menendez, P. Toliver, S. Galli, A. Agarwal, T. Banwell, J. Jackel, J. Young, S. Etemad, “Network applications of cascaded passive code translation for WDM-compatible spectrally phase-encoded optical CDMA,” *J. Lightw. Technol.*, vol. 23, no. 10, pp. 3219-3231, Oct. 2005.

- [49] S. Etemad, T. Banwell, S. Galli, J. Jackel, R. Menendez, P. Toliver, J. Young, P. Delfyett, C. Price, and T. Turpin, "Optical-CDMA incorporating phase coding of coherent frequency bins: concept, simulation, experiment," in 2004 Optical Fiber Conf. (OFC 2004), Los Angeles, CA, 2004, Paper FG5.
- [50] J.A. Salehi, A.M. Weiner, J.P. Heritage, "Coherent Ultrashort Light Pulse Code-Division Multiple Access Communication Systems", J. of Lightw. Technol., Vol. 8, page 478, March 1990.
- [51] Z. Jiang, D. Seo, S. Yang, D. E. Leaird, R. V. Roussev, C. Langrock, M. M. Fejer, and A. M. Weiner, "Four-user 10-Gb/s spectrally phasecoded O-CDMA system operating at  $\sim 30$  fJ/bit," IEEE Photon. Technol. Lett., vol. 17, no. 3, pp. 705–707, Mar. 2005.
- [52] G. L. Abbas, V. W. S. Chan, and T. K. Yee, "A dual-detector optical heterodyne receiver for local oscillator noise suppression," J. of Lightw. Technol., vol. 3, pp. 1110 – 1122, Oct 1985.
- [53] W. Lee, M-T Choi, H. Izadpanah, P. Delfyett, "Relative Intensity Noise Characteristics of a Frequency Stabilized Grating-Coupled Mode-locked Semiconductor Laser' has been accepted for publication in Electronics Letters 2006.
- [54] K. Nosu, "Advanced coherent lightwave technologies," IEEE Commun. Mag., vol. 26, pp. 15-21, Feb. 1988.
- [55] R. Linke and A. H. Gnauck, "High-capacity coherent lightwave systems," J. Lightwave Technol., vol. 6, pp. 1750-1769, Nov. 1988.
- [56] M. Iqbal, J.-I. Song, and K. Kim, "Performance of millimeter wave transmission systems with digital subcarrier modulations for radio over fiber links," in Proc. Microwave Photonics (MWP), Oxford, U.K., pp. 43–47, 2000.
- [57] H. Al-Raweshidy, Radio Over Fiber Technologies for Mobile Communications Networks. Boston, MA: Artech House, 2002.
- [58] R. Prasad, Universal Wireless Personal Communications. Boston, MA: Artech House, 1998, p. 139.
- [59] F. Kojima, M. Fujise, "Multimedia lane and station structure for road-to-vehicle communication system using ROF techniques," Personal, Indoor and Mobile Radio Communications, 2000. on , Vol.2 , pp.18-21, 2000.
- [60] T. Kuri K. Kitayama., "Optical heterodyne detection technique for densely multiplexed millimeter-wave-band radio-on-fiber systems," J. Lightwave Technol., vol. 21 , no. 12 , pp. 3167 – 3179, 2003.

- [61] Mullen, L., Vierina, A., Herczfeld, P., and Contarino, V.: 'Application of RADAR Technology to Aerial LIDAR Systems for Enhancement of Shallow Underwater Target Detection', IEEE Trans. on Microwave Theory and Techniques, 1995, 43 (9), pp. 2370-77.
- [62] Jalali, B., Kelkar, P., and Saxena, V.: 'Photonic arbitrary waveform generator', LEOS 2001, 14th Annual Meeting of the IEEE LEOS, 2001, 1, pp.253-254.
- [63] Y. Li and J. Rosen, "Object recognition using three-dimensional optical quasi-correlation," J. Opt. Soc. Am. A, Vol. 19, No. 9, pp.1755, 2002.
- [64] T.W. Hänsch and B.J. Couillaud, "Laser frequency stabilization by polarization spectroscopy of a reflecting reference cavity," Opt. Commun. 35, 441-444 (1980).
- [65] K.S. Gardner, R.H. Abram, and E. Riis "A birefringent etalon as single-mode selector in a laser cavity," Opt. Express 12, 2365-2370, 2004.
- [66] Eric O. Potma, Conor Evans, and X. Sunney Xie, R. Jason Jones and Jun Ye, "Picosecond-pulse amplification with an external passive optical cavity," Opt. Lett., Vol. 28, No. 19, pp.1835, October 1, 2003.
- [67] M. Schell, A. G. Weber, E. Scholl, and D. Bimberg, "Ultrahigh-frequency self-pulsations under gain-switching modulation in 1.5- $\mu\text{m}$  dynamical single-mode monolithic compound-cavity semiconductor lasers: Experiment and theory," IEEE J. Quantum Electron. 27, pp.1661, 1991.
- [68] J. Chen, W. Sibbett, and J. I. Vukusic, Electron. Lett. 18, pp. 426, 1982.
- [69] C.E. Zah et al, IEEE PTL vol.2, No.1, 1990.
- [70] C. H. Henry, "Theory of the Linewidth of Semiconductor Lasers," IEEE J. Quantum Electron., Vol. QE-18, NO. 2, pp. 259 – 264, 1982.
- [71] G. P. Agrawal and N. K. Dutta, Semiconductor lasers, 2<sup>nd</sup> edition, Van Nostrand Reinhold (ITP), 1993.
- [72] Y. Takushima, H. Sotobayashi, M. E. Grein, E. P. Ippen, and H. A. Haus, "Linewidth of mode combs of passively and actively mode-locked semiconductor laser diodes," Proc. of SPIE Vol. 5595, pp. 213-227, 2004.